Design and Synthesis of Naphthobisthiadiazole-based Semiconducting Polymers for Non-Fullerene Organic Photovoltaics

（非フラーレン型有機太陽電池に向けた
ナフトビスチアジアゾール系ポリマーの開発）

March 2022

周 俐慧

LI-HUI CHOU

Department of Applied Chemistry, Graduate School of Engineering

Hiroshima University

ABSTRACT

π-Conjugated (semiconductive) polymers have attracted considerable attention because of their solution-processability and excellent electronic properties. These interesting features enable their application as semiconductive materials for organic electronic devices. A set of devices that strongly rely on the properties of semiconductive polymers is organic photovoltaics, in which said polymers are typically used as a p-type (donor) material in combination with fullerene derivatives or non-fullerene π-conjugated compounds as n-type (acceptor) materials. We have been focusing on a series of semiconductive polymers based on naphthobisthiadiazole (NTz); these polymers exhibited power conversion efficiencies (PCEs) of over 10% in combination with fullerene acceptors, which is among the highest values obtained for fullerene-based cells. Based on this, we envisioned that the use of NTz-based semiconductive polymers in photovoltaic cells combined with emerging non-fullerene acceptors can provide even higher PCEs than those previously obtained with fullerene acceptors.

In this dissertation, we report the design and synthesis of two series of NTz-based semiconductive polymers through different polymer designs, namely NTz-BDT polymers and NTz-TPTz random copolymers. First, the NTz-BDT polymers exhibited better

solubility because of their suppressed polymer crystallinity and weaker sidechain interdigitation, compared with that of PNTz4T, which may afford more well-mixed donor/acceptor blend films that are effective for increasing the photocurrent. In addition, the NTz-BDT polymers exhibited deeper highest occupied molecular orbital (HOMO) energy levels than PNTz4T, which was beneficial for improving the photovoltage. Second, the NTz-TPTz random copolymers exhibited significantly higher solubility than the NTz-BDT polymers even with the addition of only a small amount of the V-shaped TPTz unit (2.5%–10%) into the PNTz4T backbone. Interestingly, NTz-TPTz random copolymers were observed to exhibit a face-on backbone orientation that was favorable for photovoltaic cells, whereas PNTz4T is known for an edge-on orientation. Consequently, we obtained PCEs of approximately 13% and 11% for the NTz-BDT polymers and NTz-TPTz random copolymers, respectively, which were higher than those for PNTz4T. Herein, we discuss the structure–property–photovoltaic performance relationships of the polymers, in comparison with PNTz4T.

TABLE of CONTENTS

LIST of FIGURES

LIST of TABLES

CHAPTER 1 INTRODUCTION

1-1 General

Over 200 years after the industrial evolution, people began to use petrochemicals as their main source of energy. In particular, the more technology flourished, the more energy sources were required. Although petroleum is a powerful energy source and can be a constant support for human beings, it can harm the environment even for the coming generations. In addition, its sources are limited, similar to other natural fossil fuels. The most serious problem for petrochemicals is that burning and extracting petroleum could generate greenhouse gases that monumentally contribute to environmental pollution. Additionally, certain hazardous substances extracted during petroleum production may threaten human lives and the planet.

Furthermore, oil shocks affect the prices of petrochemical resources, petroleum, natural fossil fuel, coal, and even staple merchandise. Consequently, other energy resources are required, such as nuclear, wind, tidal, biomass, geothermal, solar, and hydropower energies. However, nuclear energy is nonrenewable, and there are issues concerning nuclear waste. Therefore, countries have put a lot of effort into achieving the sustainable use of renewable energy.

Among these renewable resources, solar energy appears to be one of the most ideal resources for the next generation because it is renewable, and no byproducts are obtained during the energy-generating process. In addition, the annual energy emitted from the sun and received by the earth is approximately 23000 TW/year, whereas the global annual consumption is only 16 TW/years[1] (Figure 1). This indicates that the annual energy

potential that the earth receives exposed to the sun would be sufficient for our lives. Hence, the effective use of solar energy is a global issue.

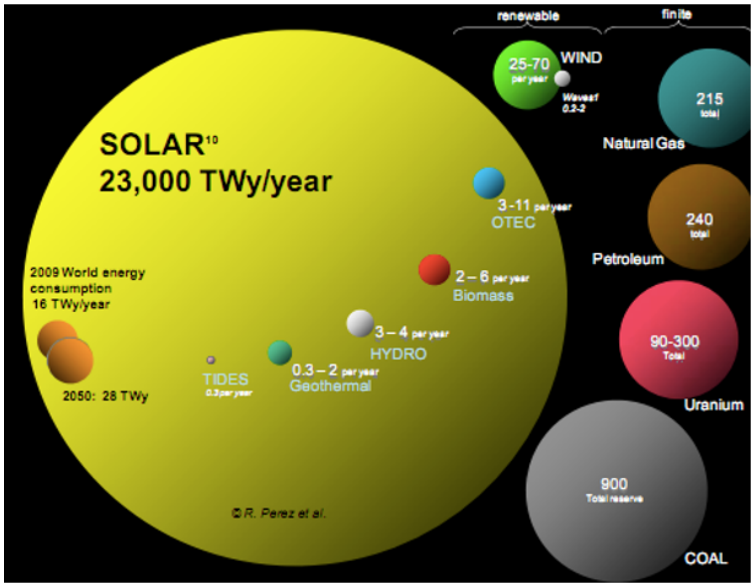

Figure 1 Annual renewable energy output and non-renewable energy storage, and global energy consumption. [1]

1-2 Evolution of Photovoltaic/Solar Cell Technology

Photovoltaic (PV)/solar cell technology can directly convert solar energy into electricity. Dissimilar to other energy resources, solar energy can be environmentally friendly for sustainable use, which is ideal. PV technology can be divided into three generations (Figure 2). First-generation PV technologies are mainly based on an elemental semiconductor (silicon). In 1954, Bell Laboratories first presented silicon-based PVs that exclusively relied on solar power. The *New York Times* wrote, "the silicon solar cell may mark the beginning of a new era, leading eventually to the realization of one of mankind's most cherished dreams–the harnessing of the almost limitless energy of the sun for the use of civilization." Silicon-based PVs, specifically crystalline silicon PVs, have been developed and are one of the most historic technologies. Silicon-based PVs demonstrate high power conversion efficiencies (PCEs) of approximately 23%–27%, depending on the crystalline motifs.

Second-generation PV technologies include silicon-based PVs that use amorphous silicon (thin film) and polycrystalline silicon. Amorphous silicon that exhibits a PCE of up to 14% can be deposited as a thin film and can be processed on glass substrates or even on flexible substrates. The second generations include PVs based on compound semiconductors, such as copper indium gallium selenide (CIGS) and cadmium telluride (CdTe), which can also be made as thin films. CIGS and CdTe typically exhibit PCEs in the range of 20%–23% that are slightly lower than that of crystalline silicon. The use of silicon wafers is avoided for second-generation PVs to lower the consumption of materials and possibly reduce the production cost. However, second-generation cells require a vacuum and high-temperature process, which largely consume energy. There is also the

pollution of heavy metals, particularly in compound semiconductor-based PVs, in which those scarce elements are a limiting factor for this generation.

The third-generation PVs are based on organic or organic–inorganic hybrid semiconductive materials, such as dye-sensitized solar cells (DSSC), organic solar cells (organic photovoltaics (OPVs)), and perovskite solar cells. A striking feature of these PVs is solution-processability, which should result in low production costs, compared with those of other PVs. As the solution process is a low-temperature methodology, these PVs can even be manufactured on plastic substrates. Recently, the PCE of perovskite solar cells dramatically increased to 25%, which is comparable to that of crystalline silicon-based PVs. However, perovskite solar cells use toxic lead-based semiconductors, which is a serious issue in practical application. OPVs, without the problem of materials, are promising and flexible. Owing to the high light absorption of organic materials, the thickness of the photoactive layer of OPVs is in the order of hundreds of nanometers. Therefore, OPVs can be semitransparent PVs, which greatly expands the scope of application. A major issue for OPVs is their lower PCE, compared with that of inorganic solar cells, such as silicon solar cells.

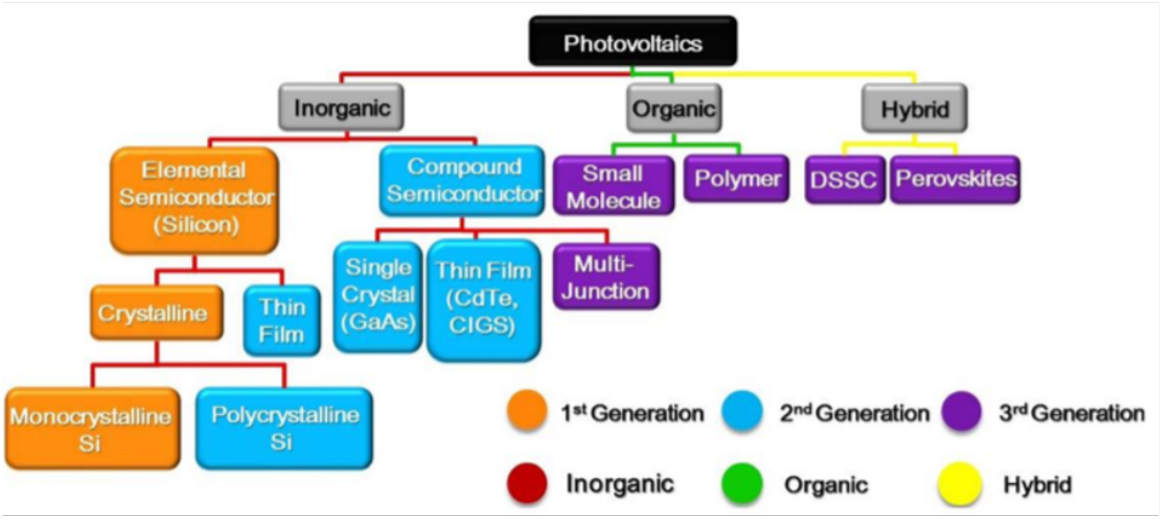

Figure 2 Generation of photovoltaic technology [2]

The National Renewable Energy Laboratory (NREL) reported a chart of PCEs for different types of solar cells, called the "Best Research-Cell Efficiency Chart", as shown in Figure 3. OPVs had been known to exhibit PCEs of only approximately 5% in the 2000s. However, owing to the development of organic semiconductors, specifically p-type semiconductive polymers, the PCE of OPVs has remarkably increased in the early 2010s to 10%. Recently, owing to the development of n-type organic semiconductors, called "non-fullerene acceptors (NFAs)," the PCE has exceeded 18%. Although OPVs still face several challenges including stability and low PCEs, their features such as low-cost and low-energy consumption production, flexibility, semitransparency, and lightweight offer great possibilities to become a popular PV technology.

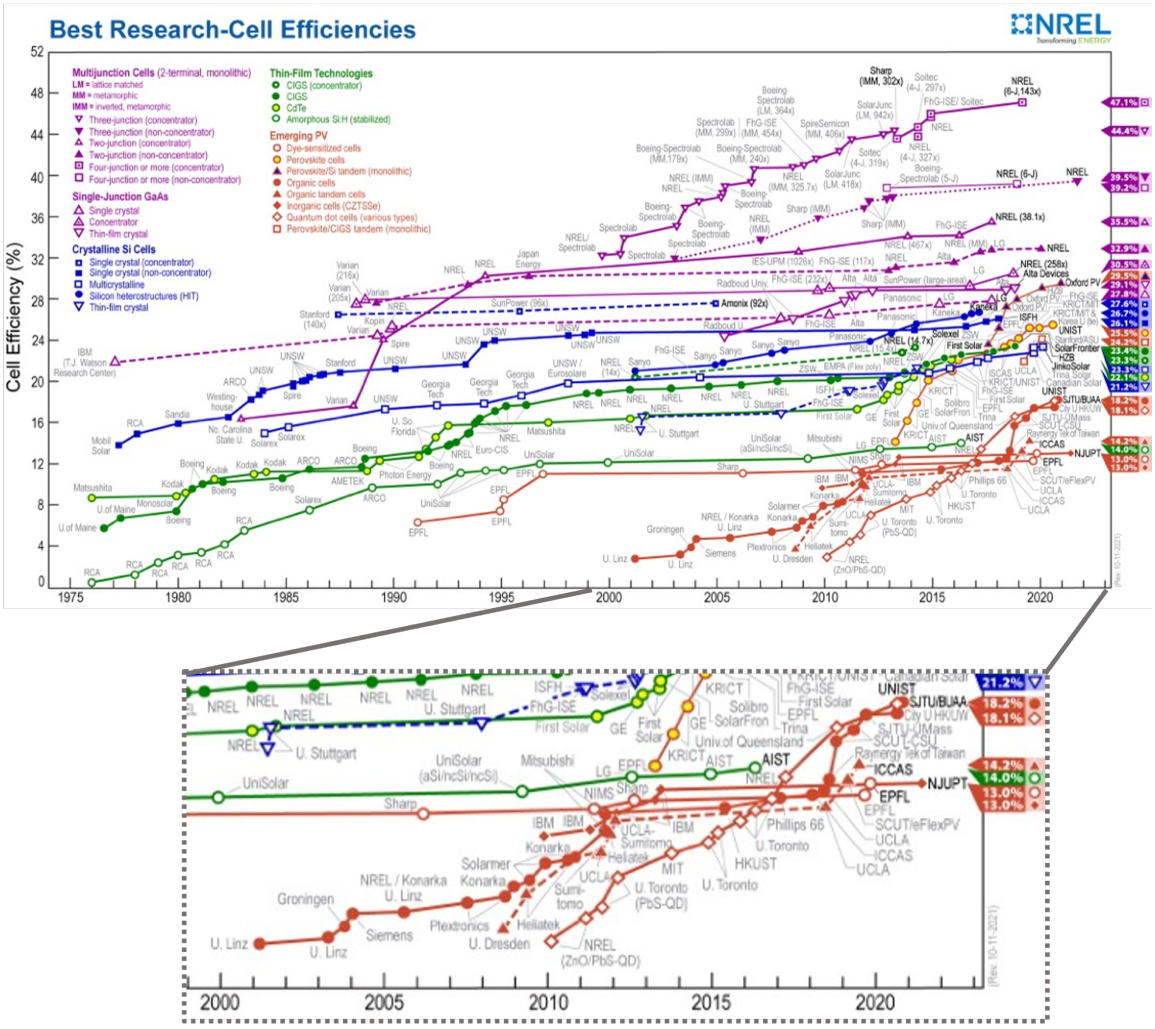

Figure 3 Best research-cell efficiency chart reported by NREL in November 2021, and the magnification for emerging PVs including OPVs.

1-3 Characteristics of Solar Cell

1-3-1 Basic Introduction

A solar cell is a semiconductor/PN junction diode. Normally, cells do not have an external bias. Nevertheless, they can provide/convert sunlight into electricity when solar cells are illuminated. (Figure 4)

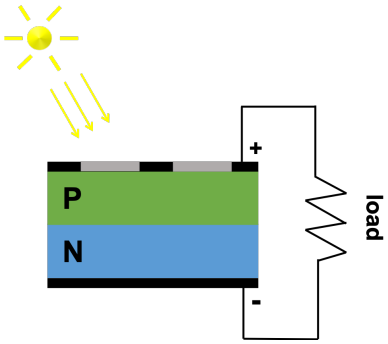

Figure 4 Basic structure of the solar cell.

The typical characteristics of solar (photovoltaic) cells are shown as a current–voltage curve (*I–V*). Figure 5 shows the *I–V* curve of a cell without light illumination as a green line. In an ideal situation, without illumination, there is no current flow through the solar cell unless an external bias is applied. With incident sunlight, the *I–V* curve shifts down, generating an external current flow.

As the solar cell is illuminated by sunlight, the active (photoactive) layer creates several electron-hole pairs (excitons) by the photoelectric effect. The incident light breaks the thermal equilibrium condition of the junction. The free electrons in the depletion region diffuse into the n-type side of the junction. Similarly, the holes diffuse to the p-type side. When an external potential bias that is greater than the depletion barrier potential is applied, the carriers migrate throughout the solar cell, thereby generating electricity.

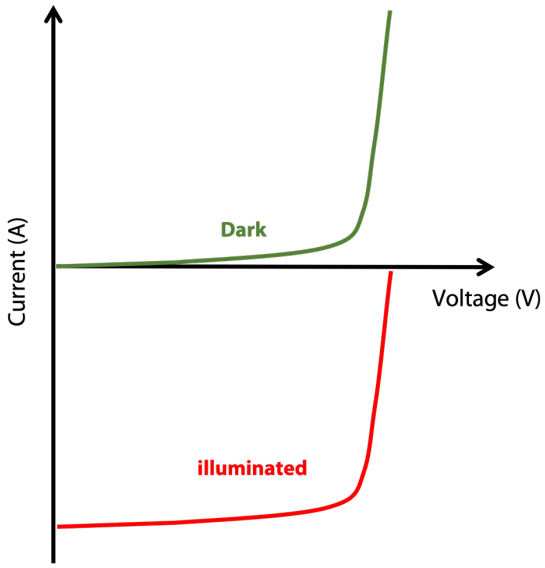

Figure 5 Characteristics current- voltage (*I-V*) curve under dark and light illumination.

1-3-2 Characteristics Curves

Through the *I–V* measurement, we obtained various parameters that determine the quality of a solar cell (Figure 6). One of such parameters is the short-circuit current (I_{SC}), commonly shown as the short-circuit current density (J_{SC}) when considering the area of the solar cell. Other parameters include the open-circuit voltage (V_{OC}), fill factor (FF), maximum current density (J_{max}), maximum voltage (V_{max}), and maximum output power (P_{max}). Certain additional parameters, including series and shunt resistances (R_s and R_{sh}), are also used to fully characterize the solar cell.

The quantum efficiency of a solar cell represents the current that the cell would generate when irradiated by photons through wavelength. The current can be evaluated by integrating the quantum efficiency over the spectrum. Two types of quantum efficiency of the solar cell are typically considered: External/internal quantum efficiency (EQE and IQE). EQE is defined as the ratio of the number of electrons in an external circuit to the number of incident photons (Figure 6b); it can be directly obtained from the spectral

response, which is also known as the incident photon to current conversion efficiency (IPCE). The EQE result can be modified to factor in the reflectance and transmittance to consider the portion of the incident light in an active region. IQE is defined as the number of absorbed photons in the solar cell to the number of collected carriers. This allows a better understanding of the material properties of solar cells.

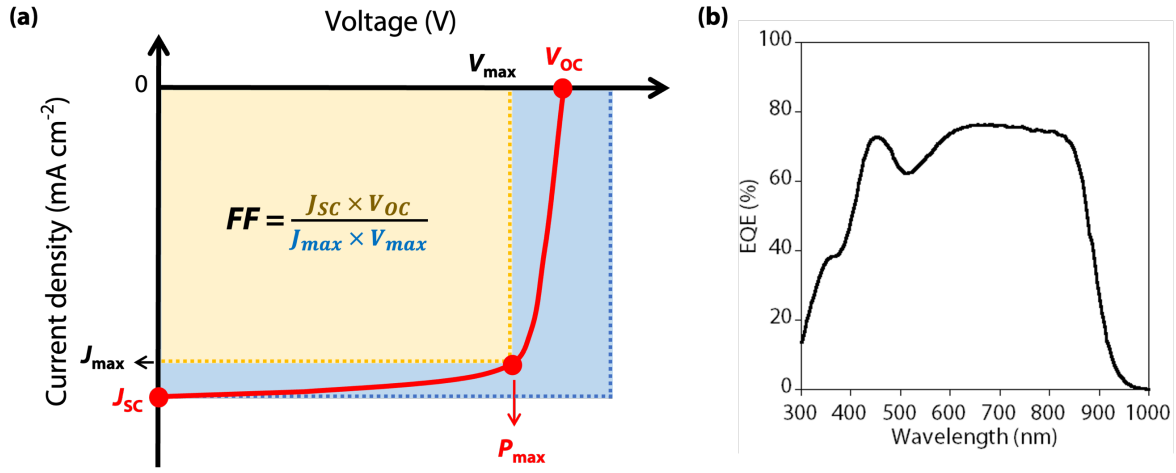

Figure 6 (a) Important parameters in the *I–V* curve and (b) a quantum efficiency spectrum.

(1) Open-circuit Voltage, V_{OC}

The open-circuit voltage is the maximum voltage available from a solar cell when the current is zero. This voltage corresponds to the amount of forward bias on the solar cell due to the bias of the solar cell junction with the light-generated current. The open-circuit voltage is shown on the *J–V* curve above.

(2) Short-circuit Current, I_{SC} (Short-circuit Current Density, J_{SC})

The short-circuit current is the current through the solar cell when the voltage across the cell is zero. The I_{SC} is due to the generation and collection of light-generated

carriers, which is the largest current that may be drawn from the solar cell. The I_{SC} from a solar cell is directly dependent on the illumination light intensity; it decreases at a lower intensity of illumination light.

(3) Fill Factor, FF

The FF is used to define the ratio of cell to the ideal cell. The maximum power point (P_{max}) is the multiplication of the maximum voltage output point (V_{max}) and the maximum current density output point (J_{max}) (yellow area). The multiplication of V_{OC} and J_{SC} can obtain the blue area in Figure 6. Owing to the structural design and process conditions of solar cells, the cell cannot achieve the ideal output power, and there are new parameters to define the cells. The yellow area represents the maximum ideal power that the cell can output. The ratio of the blue to the yellow areas represents the FF. Additionally, Equation (1-1) can be used to express it as follows:

The FF varies with the type of solar cell and the quality of the solar cell and generally falls between 0.5 and 0.85. The larger the fill factor, the closer the solar cell to the ideal diode.

$$\mathrm{FF} = \frac{V_{oc} \times J_{sc}}{J_{max} \times V_{max}} \qquad (1\text{-}1)$$

(4) Power Conversion Efficiency, PCE

The photoelectric conversion efficiency is the ability to convert light energy into electrical energy. Equation (1-2) shows the definition of PCE as the ratio of the maximum power to the energy (E) of the incident sunlight.

The PCE would be different if the irradiated sunlight energy changed; therefore, it

has been internationally defined as uniform standard solar energy. Solar radiation is approximately 6000 K blackbody radiation, and the radiant energy reaching the surface of the earth's atmosphere is approximately 1353 kW/m^2. The radiant energy will be reduced because of atmospheric absorption, and the strength of the path through different atmospheres is also different. Here, the solar spectrum outside the atmosphere is defined as AM0, where the air mass (AM) is used to express the characteristics of the absorption of the atmosphere, which leads to a decrease in the solar spectrum and radiant energy. Standard sunlight is defined when the air quality of solar radiation is AM1.5, and the temperature is 25 °C; the incident sunlight intensity (P_{light}) at this time is 100 mW cm^{-2}, as shown in Equation (1-3). Therefore, to improve the PCE, it is necessary to improve the quality of the solar cell and increase the V_{OC}, J_{SC}, and FF. These parameters reflect the quality of the material. In addition, the overall component structure and manufacturing process of the solar cell is a controlling factor.

$$PCE = \frac{V_{max} \times J_{max}}{E} \times 100\% = \frac{P_{max}}{E} \times 100\% \qquad (1\text{-}2)$$

$$PCE = \frac{V_{OC} \times J_{SC} \times FF}{P_{light}} \times 100\% = \frac{V_{OC} \times J_{SC} \times FF}{100 \frac{mW}{cm^2}} \times 100\% \qquad (1\text{-}3)$$

CHAPTER 2 Introduction of Organic Solar Cells

2-1 Working Principle of Organic Solar Cells

The organic solar cell is a promising device for solar energy conversion. It has attracted considerable interest among researchers and the industrial community because of its potential advantages (lightweight, low cost, and mechanical flexibility).[3-7] Typically, semiconductive polymers have been used as an electron donor (p-type material), combined with a fullerene derivative [8-10] or non-fullerene material [11-14] as an electron acceptor (n-type material). In the past decade, extensive efforts were devoted to developing a wide variety of p-type semiconductive polymers [15-17] to obtain high-performance organic solar cells and n-type semiconductive polymers. [18-22]

It is possible to promote charge carrier transport ability through molecular design. Therefore, the design of the semiconductive polymer is important for a high-performance solar cell. The chemistry of semiconductive polymers offers powerful methods for easy control of their properties. Recently, the PCE of single-junction devices exceeded 19%, owing to the fine-tuning of light utilization and the photophysical process of the active layers [23].

2-2 Requirements for Semiconducting Polymers

For semiconductive polymers, the optical bandgap (E_g), deep highest occupied molecular orbital (E_{HOMO}), and lowest unoccupied molecular orbital (E_{LUMO}) energy levels are important parameters for organic solar cells. The energy difference between the E_{HOMO} of a p-type material and the E_{LUMO} of an n-type material (ΔE_{HL}) is known to correlate with

the V_{OC} (Figure 7).[24] Regarding the electronic properties, the requirements to improve the performance include a narrow E_g with a deep E_{HOMO}, which is crucial for optimizing the V_{OC} and J_{SC}. Additionally, the energy difference (ΔE_{LL}) between the p-type and n-type materials serves as a driving force to ensure an efficient photoinduced charge transfer, in which $\Delta E_{LL} \geq 0.3$ eV is necessary.

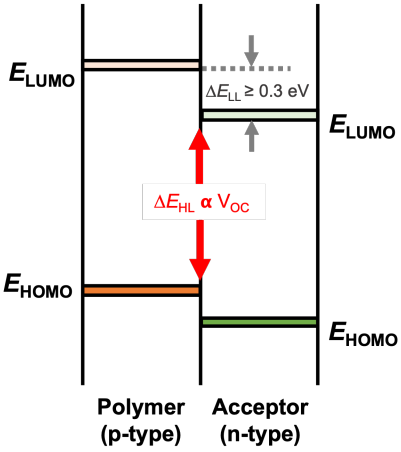

Figure 7 Schematic diagram of band structure of organic photovoltaic.

Organic solar cells exhibit lower efficiency, compared with inorganic photovoltaic cells based on Si, CIGS, or perovskite solar cells, owing to a serious loss in photoenergy. Photoenergy loss in organic solar cells is defined as $E_{loss} = E_g - eV_{OC}$, where e is the elementary charge.[25-26] To further enhance the PCE, the E_{loss} must be reduced. The E_{LUMO} of the p-type material should be as close as the n-type material to minimize the offset energy loss and increase the V_{OC}.

Charge carrier transport is an important function in semiconductive polymers mainly governed by intramolecular transport along the polymer backbone and intermolecular transport along the π–π overlaps that significantly influence the performance.[27] Therefore, the desired structural features for semiconductive polymers are as follows. First, the

polymer backbone must be coplanar, and the π–π stacking distance should be as close as possible; this can be regarded as a highly crystalline structure. Second, the backbone orientation should be ‘‘face-on’’ (Figure 8b) because the out-of-plane charge carrier transport is required for organic solar cells (‘‘edge-on’’ orientation is essential for in-plane transport in organic field-effect transistors (OFETs), [28] as shown in Figure 8a.

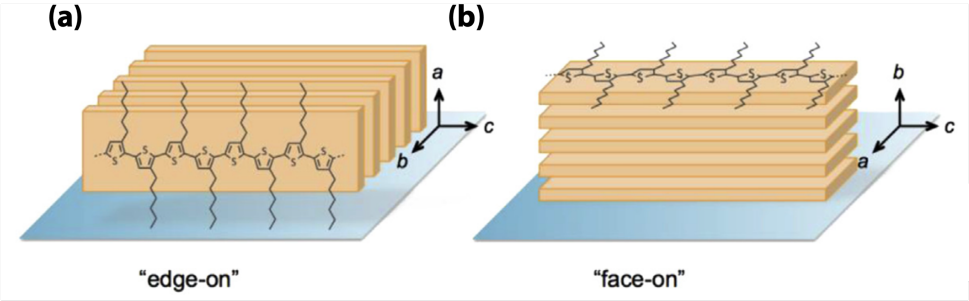

Figure 8 Representation of backbone orientation for semiconducting polymers with respect to the substrate.[29]

2-3 Semiconducting Polymers

π-Conjugated (semiconductive) polymers have attracted considerable attention because of their feature advantages of solution processability and excellent electronic properties. Representative semiconductive polymers are shown in Figure 9a. These polymers are significant functional materials that can be utilized for organic electronic devices. Studies on organic electronics such as organic light-emitting diodes (OLEDs) [30-31], organic field-effect transistors (OFETs) [32-33], and organic solar cells (Figure 9b) have recently been conducted worldwide.

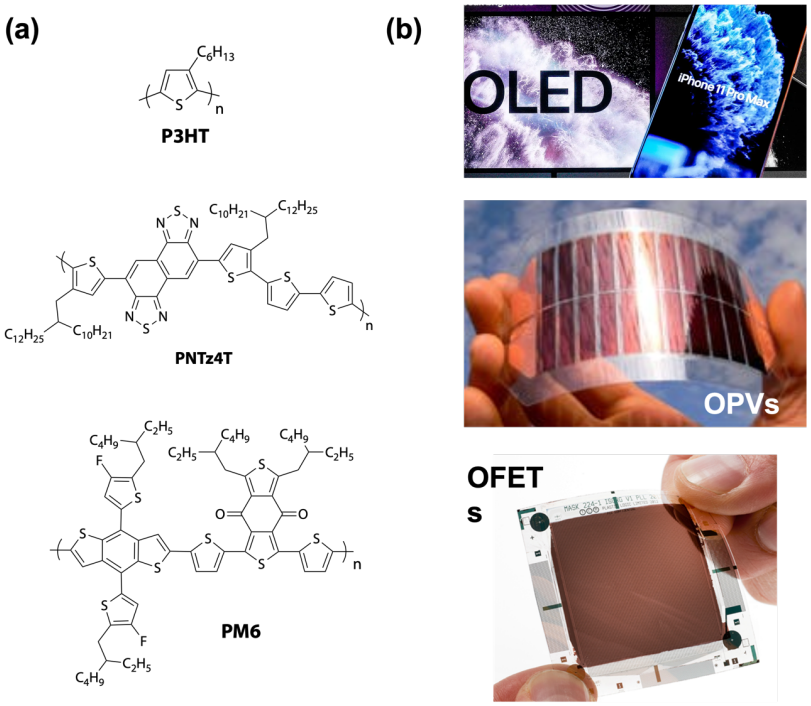

Figure 9 (a) Chemical structures of representative semiconductive polymers. (b) Images of organic electronics such as organic light-emitting diodes (OLEDs), organic field-effect transistors (OFETs), and organic photovoltaics (OPVs).[34-36]

2-4 Evolution of Semiconducting Materials for Organic Solar Cells

In general, semiconductive polymers comprise electron-rich (D) and electron-deficient (A) heterocyclic π-building units alternately incorporated in the backbone, which is a state of an art material system that greatly functions in organic solar cells, called donor–acceptor semiconductive polymers. Polymer solar cells based on conjugated p-type polymers and fullerene derivatives have been intensively investigated in the last decade.[8] Regioregular poly(3-hexylthiophene) (**P3HT**, Figure 10) and [6,6]-phenyl C_{61}vbutyric acid methyl ester ($PC_{61}BM$) represent two of the most successful systems with PCEs in the range of 4–5% (Figure 10).[37-39] However, further improvement of the performance was limited to its narrow absorption spectrum (300–650 nm) and high E_{HOMO} (−4.9 eV). Therefore, great effort has been devoted to developing new conjugated polymer donors and new fullerene derivative acceptors [40-42] to solve these issues.[43-44] An efficient way to broaden absorption without sacrificing the E_{HOMO} is to narrow the optical bandgaps of the polymers. The combination of electron-rich and electron-deficient moieties (so-called donor–acceptor systems) has been effectively demonstrated to obtain a small bandgap of alternating conjugated polymers, which has greatly influenced solar cells. [45-48] Poly[4,8-bis[(2-ethylhexyl)oxy]benzo[1,2-*b*:4,5-*b′*]dithiophene-2,6-diyl][3-fluoro-2-[(2-ethylhexyl)carbonyl]thieno[3,4-*b*]thiophenediyl] (**PTB7**) (Figure 10) was developed and exhibited a PCE of 7.4%, which indicated great potential and a bright future for polymer solar cells.[45]

Considerable efforts have been dedicated to the development of NFAs since 2012.[49-51] A novel electron acceptor, **ITIC** (Figure 10), was designed, and a PTB7:ITIC-based solar cell exhibited better performance than a fullerene-based solar cell. This result greatly

promoted the development of alternative acceptors for organic solar cells.[11] The E_{loss} of the NFA-based organic solar cells was significantly suppressed, thereby improving the PCE to 15%.[52] Recently, an NFA (**Y6**, Figure 10) and its Y-derivative attracted huge attention because of their remarkable photovoltaic performances. [12-14, 53-55] These advances are extremely encouraging and initiate a critical question of how to further improve the PCEs by designing new materials.

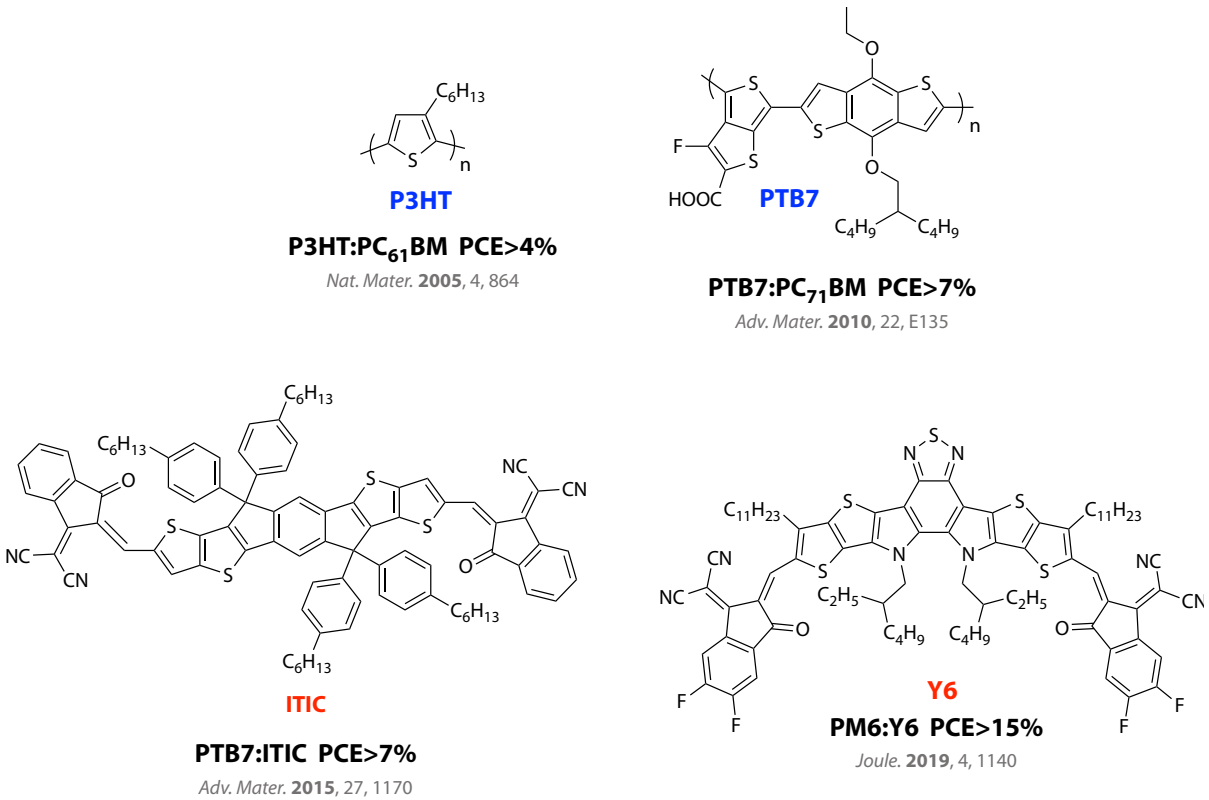

Figure 10 Chemical structure of semiconducting polymers, and non-fullerene acceptor materials.

2-5 Naphthobisthiadiazole-based Semiconducting Polymers

Among various building units for D–A polymers, naphtho[1,2-*c*:5,6-*c*′]bis[1,2,5]thiadiazole (NTz) (Figure 11) has been confirmed to be a high-potential A unit because of its electron-deficient nature that offers a relatively deep E_{HOMO}, small bandgaps, and rigid and large planar structures that promote strong intermolecular interactions.[56-57]

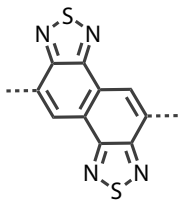

NTz

Figure 11 Chemical structure of acceptor unit: NTz.

In previous studies, we demonstrated that a semiconductive polymer based on NTz with a quarter-thiophene moiety and long branched alkyl chains, **PNTz4T** (Figure 12), exhibited a highly crystalline structure with the face-on orientation in combination with $PC_{71}BM$ and achieved a PCE of approximately 10%, which was extremely high for a fullerene-based solar cell.[48, 58] However, the energy level of **PNTz4T** limited the V_{OC} and affected the performance. The introduction of halogen substitution is an efficient strategy to tune the energy level and ensure the coplanarity of the polymer backbone.[44, 59-60] Recently, we developed a **PNTz4T** family (Figure 12), in which fluorine atoms were introduced into the polymer backbone.[17, 61]

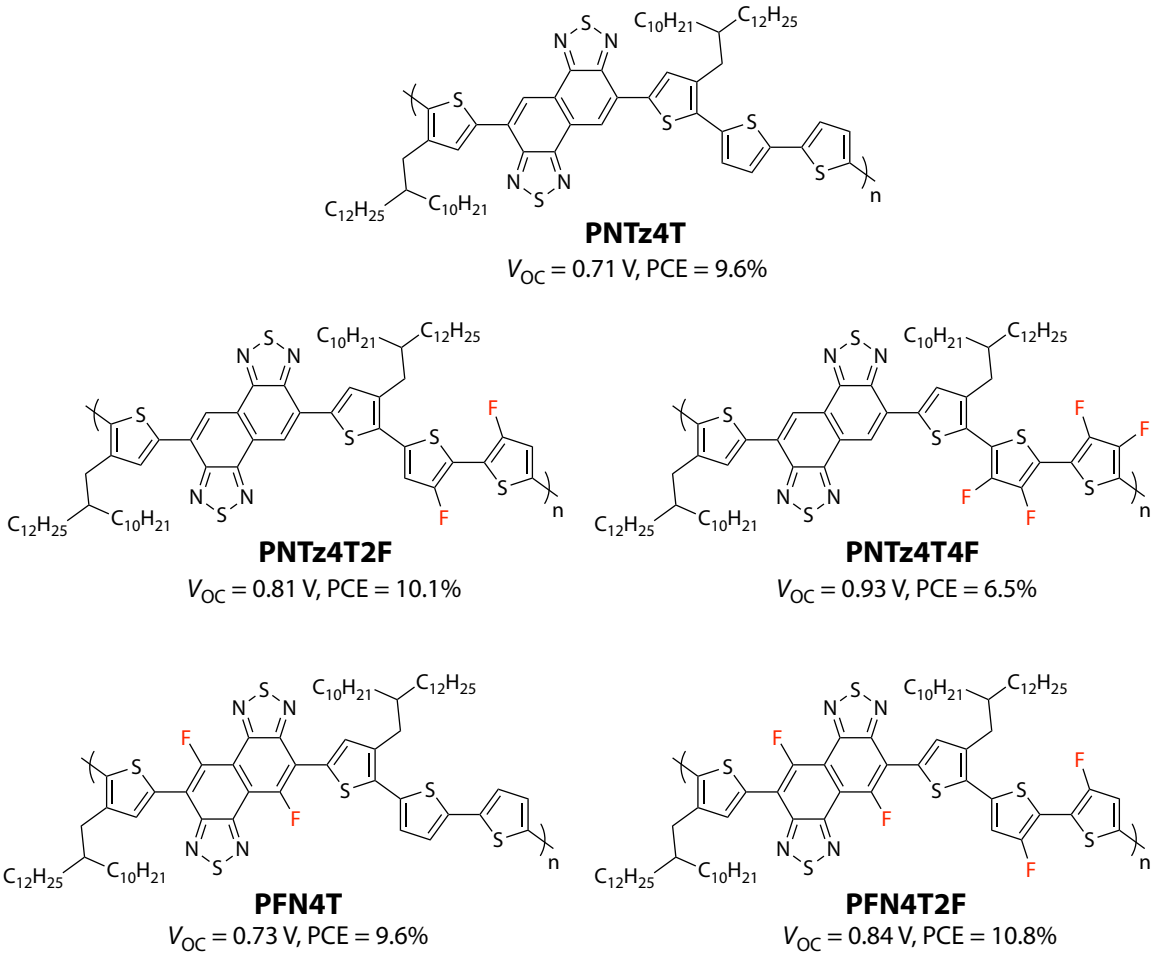

Figure 12 Chemical structure of **PNTz4T** and a series of PNTz4T family: **PNTz4T2F**, **PNTz4T4F**, **PFN4T** and **PFN4T2F**.[17, 48, 61]

All the fluorinated polymers had a deeper E_{HOMO} than **PNTz4T**, which improved the V_{OC} to 0.90 V, thereby achieving a high PCE of 11%. However, the introduction of the fluorine atom enhanced the backbone coplanarity, owing to the intramolecular noncovalent interactions between the fluorine and sulfur atoms in the thiophene ring, thereby significantly influencing the solubility. **PNTz4T** and these fluorinated polymers had sufficiently high M_n values in the range of 40000–50000 kDa, which were soluble in hot chlorinated solvents, such as chlorobenzene (CB) and *o*-dichlorobenzene (DCB). Therefore, these studies were fundamentally based on a fullerene-based solar cell system

($PC_{71}BM$). The solubility issues of these polymers can limit their solution-processability and affect their miscibility with acceptor materials, resulting in poor photovoltaic performances, particularly for NFA-based solar cells.

To obtain good solubility and high photovoltaic performance, we alternatively designed NTz-based D–A polymers for a non-fullerene solar cell. First, we discuss the performances of **PNTz4T** in the role of a non-fullerene solar cell. Afterward, the new π-conjugated polymers (NTz-BDT polymers), which possess a benzodithiophene (BDT) unit with alkylthienyl substituents, are discussed. The energetic properties, photovoltaic performances, polymer packing, and film morphology were investigated. Consequently, PNTzBDT-F obtained a PCE exceeding 13% in combination with **Y6**. Thereafter, the NTz-TPTz random copolymers were investigated while collaborating with Prof. Tajima in Riken. Triphenyleno[1,2-*c*:7,8-*c'*]bis([1,2,5]thiadiazole) (TPTz) was introduced in a small amount (2.5%–10%) while preserving the intermolecular interaction of **PNTz4T** and improving the solubility. The characteristics and photovoltaic performances of these random copolymers were carefully investigated.

CHAPTER 3 EXPERIMENTAL SECTION

3-1 Materials

3-1-1 NTz Monomer

The synthetic route of NTz monomer was listed in Scheme 1, and further synthesized the brominated NTz2T with different alkyl sidechain (R = BO, DT). And 5,10-bis(5-bromo-4-(2-butyloctyl)thiophen-2-yl)naphtho[1,2-c:5,6- c']bis([1,2,5]thiadiazole (**NTz2T-Br$_2$**) will be used for further polymerization through stille-coupling reaction in this research.[48]

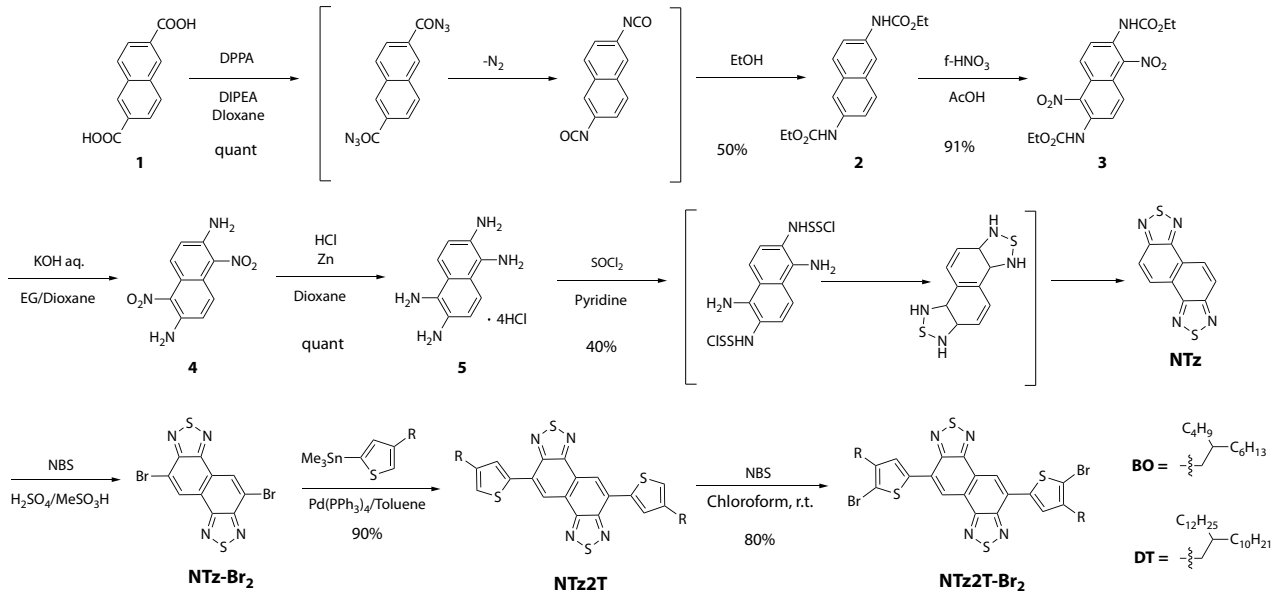

Scheme 1. Synthetic route to the NTz monomer.

3-1-2 NTz-BDT Polymers

All the reagents were purchased from commercial sources and used without further purification. 2,6-bis(trimethytin)-4,8-bis(5-(2-ethylhexyl)-4-thiophen-2-yl)benzo[1,2-*b*:4,5-*b*′]dithiophene (**1**) and 2,6-bis(trimethytin)-4,8-bis(5-(2-ethylhexyl)-4-fluorothiophen-2-yl)benzo[1,2-*b*:4,5-*b*′]dithiophene (**2**) were purchased from Ossila Ltd. 2,6-Bis(trimethytin)-4,8-bis(5-(2-ethylhexyl)-4-chlorothiophen-2-yl)benzo[1,2-*b*:4,5-*b*′]dithiophene (**3**)[62], 5,10-bis(5-bromo-4-(2-butyloctyl)thiophen-2-yl)naphtho[1,2-*c*:5,6-*c*′]bis([1,2,5]thiadiazole (**4**)[48] and **PNTz4T**[48] were synthesized according to published procedure. Polymerization was carried out with a microwave reactor, Biotage Initiator. Molecular weight of the polymers was evaluated by a high-temperature GPC (140 °C), TOSOH HLC-8121GPC/HT, using *o*-dichlorobenzene as the eluent and calibrated with polystyrene standard. High-resolution mass spectrometry (HRMS) was performed with an LTQ Orbitrap XL spectrometer.

Polymerization was carried out with a microwave reactor, Biotage Initiator. Molecular weight of the polymers was evaluated by a high-temperature GPC (140 °C), TOSOH HLC-8121GPC/HT, using o-dichlorobenzene as the eluent and calibrated with polystyrene standard. High-resolution mass spectrometry (HRMS) was performed with an LTQ Orbitrap XL spectrometer.

***PNTzBDT*: 1** (45.2 mg, 0.05 mmol), **4** (45.2 mg, 0.05 mmol), $Pd(PPh_3)_4$ (1.16 mg, 2 mol%) and toluene (2 mL) were added to reaction tube, then heated to 200 °C for 2 hours in microwave reactor. After cooling to room temperature, the reaction solution was poured into 50 mL of methanol containing 2 mL of hydrochloric acid and stirred for 1 hour. Then the precipitate was collected sequentially with methanol, hexane, and dichloromethane through Soxhlet extraction to remove the impurities and low-molecular weight fractions. The residue was then extracted with chloroform, and reprecipitated in 50 mL of methanol. The precipitate was collected and dried in vacuum to yield the polymer as dark blue solid (56 mg, 85%). Anal. Calced for $C_{78}H_{100}N_4S_8$: C, 69.15; H, 7.18, N, 4.24. Found: C, 68.94; H, 7.18, N, 4.12. M_n = 63 kDa, M_w = 106 kDa, $Đ$ = 1.7.

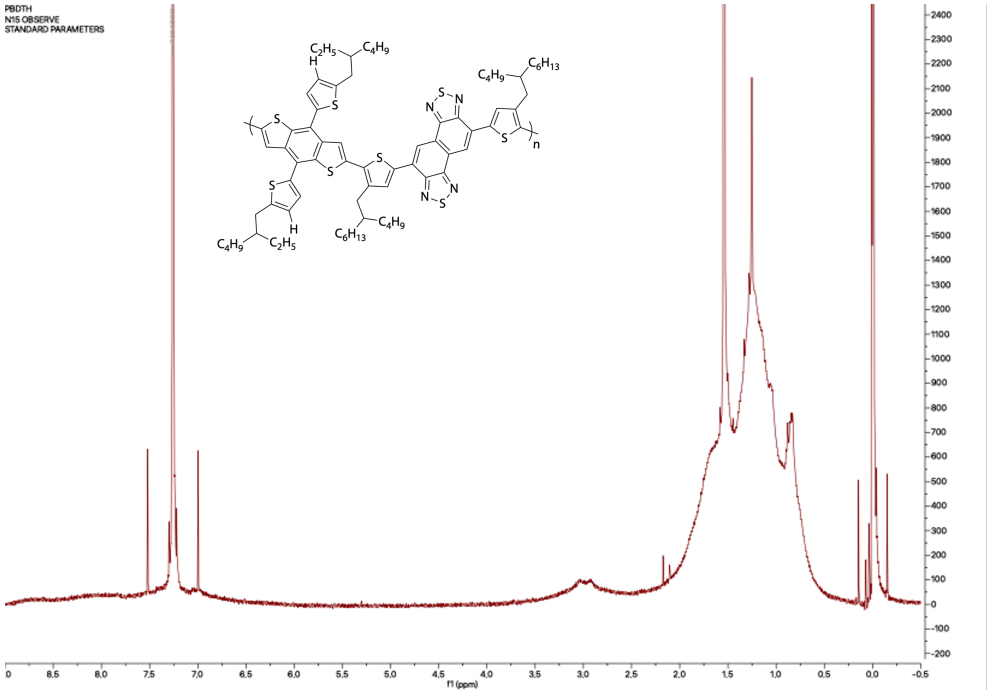

^{1}H-NMR spectrum of ***PNTzBDT***.

PNTzBDT-F: **2** (47.0 mg, 0.05 mmol), **4** (45.2 mg, 0.05 mmol), $Pd(PPh_3)_4$ (1.16 mg, 2 mol%) and toluene (2 mL) were added to reaction tube, then heated to 200 °C for 2 hours in microwave reactor. After cooling to room temperature, the reaction solution was poured into 50 mL of methanol containing 2 mL of hydrochloric acid and stirred for 1 hour. Then the precipitate was collected sequentially with methanol, hexane, and dichloromethane through Soxhlet extraction to remove the impurities and low-molecular weight fractions. The residue was then extracted with chloroform, and reprecipitated in 50 mL of methanol. The precipitate was collected and dried in vacuum to yield the polymer as dark blue solid (62 mg, 91%). Anal. Calced for $C_{78}H_{98}F_2N_4S_8$: C, 67.31; H, 6.84, N, 4.13. Found: C, 67.02; H, 6.75, N, 4.06. M_n = 41 kDa, M_w = 94 kDa, $Đ$ = 2.3.

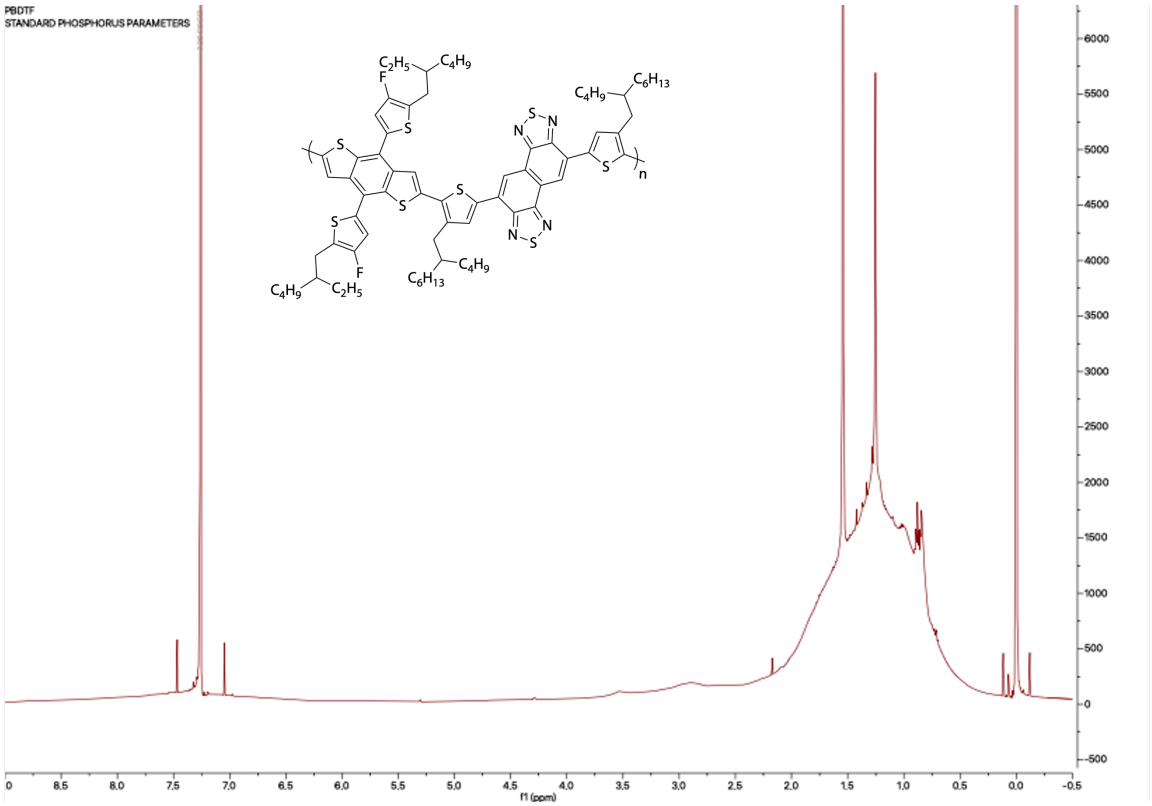

^{1}H-NMR spectrum of ***PNTzBDT-F***.

***PNTzBDT-Cl*: 3** (48.7 mg, 0.05 mmol), **4** (45.2 mg, 0.05 mmol), $Pd(PPh_3)_4$ (1.16 mg, 2 mol%) and toluene (2 mL) were added to reaction tube, then heated to 200 °C for 2 hours in microwave reactor. After cooling to room temperature, the reaction solution was poured into 50 mL of methanol containing 2 mL of hydrochloric acid and stirred for 1 hour. Then the precipitate was collected sequentially with methanol, hexane, and dichloromethane through Soxhlet extraction to remove the impurities and low-molecular weight fractions. The residue was then extracted with chloroform, and reprecipitated in 50 mL of methanol. The precipitate was collected and dried in vacuum to yield the polymer as dark blue solid (54 mg, 78%). Anal. Calced for $C_{78}H_{98}Cl_2N_4S_8$: C, 65.72; H, 6.68, N, 4.03. Found: C, 65.81; H, 6.64, N, 3.90. M_n = 63 kDa, M_w = 166 kDa, $Đ$ = 2.7.

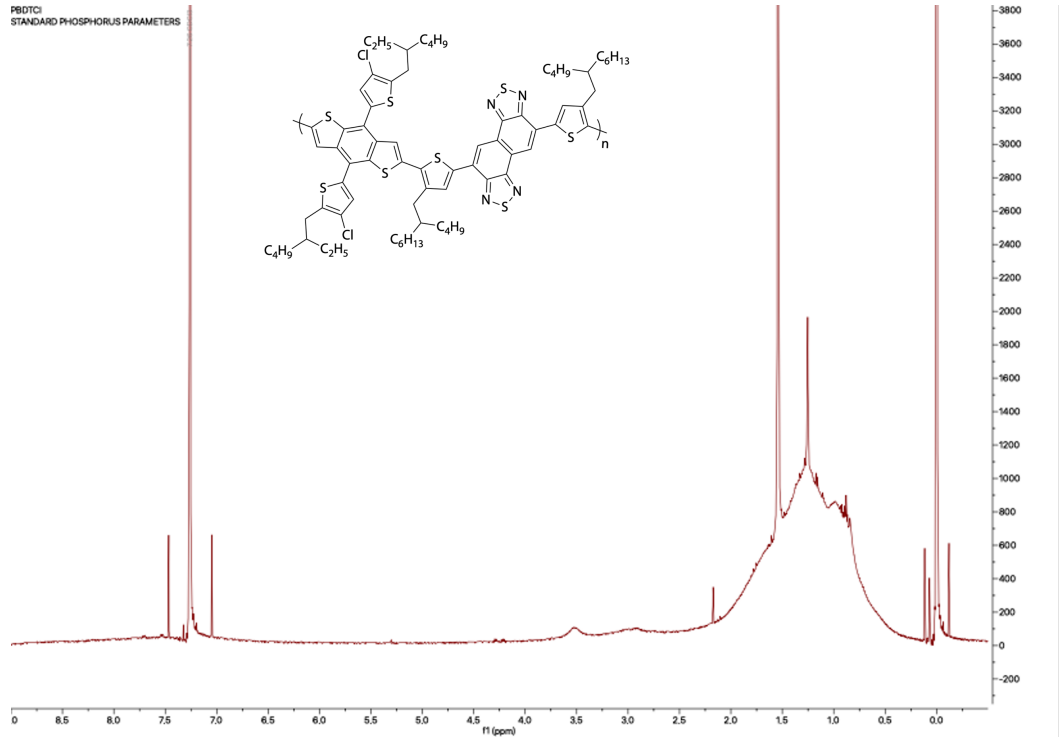

^{1}H-NMR spectrum of ***PNTzBDT-Cl***.

Table 1 Polymerization results of NTz-BDT polymers.

Polymer	M_n[a] (g mol^{-1})	M_w[a] (g mol^{-1})	$Đ$
PNTz4T	31,000	110,000	3.5
PNTzBDT	63,000	106,000	1.7
PNTzBDT-F	41,000	94,000	2.3
PNTzBDT-Cl	63,000	166,000	2.7

[a] Determined by high-temperature GPC (*o*-dichlorobenzene, 140 °C) calibrated with polystyrene standard.

3-1-3 NTz-TPTz Random Copolymers

All the reagents were purchased from commercial sources and used without further purification. 5,10-bis(5-bromo-4-(2-butyloctyl)thiophen-2-yl)naphtho[1,2-c:5,6-c']bis([1,2,5]thiadiazole (**NTz2T-Br$_2$**), distannylated bithiophene **(2T-(SnMe$_3$)$_2$)** and **PNTz4T** were synthesized according to published procedure.[48] 4,7-Dibromo-12,13-bis((2-R)oxy)triphenyleno[1,2-c:7,8- c']bis([1,2,5]thiadiazole) (TPTz-Br) with different alkyl side chain (R= C8, CEH, C12 and CBO) were provided by Prof. Tajima and synthesized according to published procedure.[63]

Polymerization was carried out with a microwave reactor, Biotage Initiator. Molecular weight of the polymers was evaluated by a high-temperature GPC (140 °C), TOSOH HLC-8121GPC/HT, using o-dichlorobenzene as the eluent and calibrated with polystyrene standard. High-resolution mass spectrometry (HRMS) was performed with an LTQ Orbitrap XL spectrometer.

***CR-5%* (R=C8, C12, EH, BO):** NTz2T-Br$_2$ (0.0475 mmol), A3-CR (0.0025 mmol), 2T-(SnMe$_3$)$_2$ (0.05 mmol), Pd(PPh$_3$)$_4$ (1.16 mg, 2 mol%) and toluene (2 mL) were added to reaction tube, then heated to 200 °C for 2 hours in microwave reactor. After cooling to room temperature, the reaction solution was poured into 50 mL of methanol containing 2 mL of hydrochloric acid and stirred for 1 hour. Then the precipitate was collected sequentially with methanol, hexane, and dichloromethane through Soxhlet extraction to remove the impurities and low-molecular weight fractions. The residue was then extracted

with chloroform, and reprecipitated in 50 mL of methanol. The precipitate was collected and dried in vacuum to yield the polymer as dark blue solid (85% for **C8-5**, 91% for **C12-5**, 95% for **EH-5** and 85% for **BO-5**).

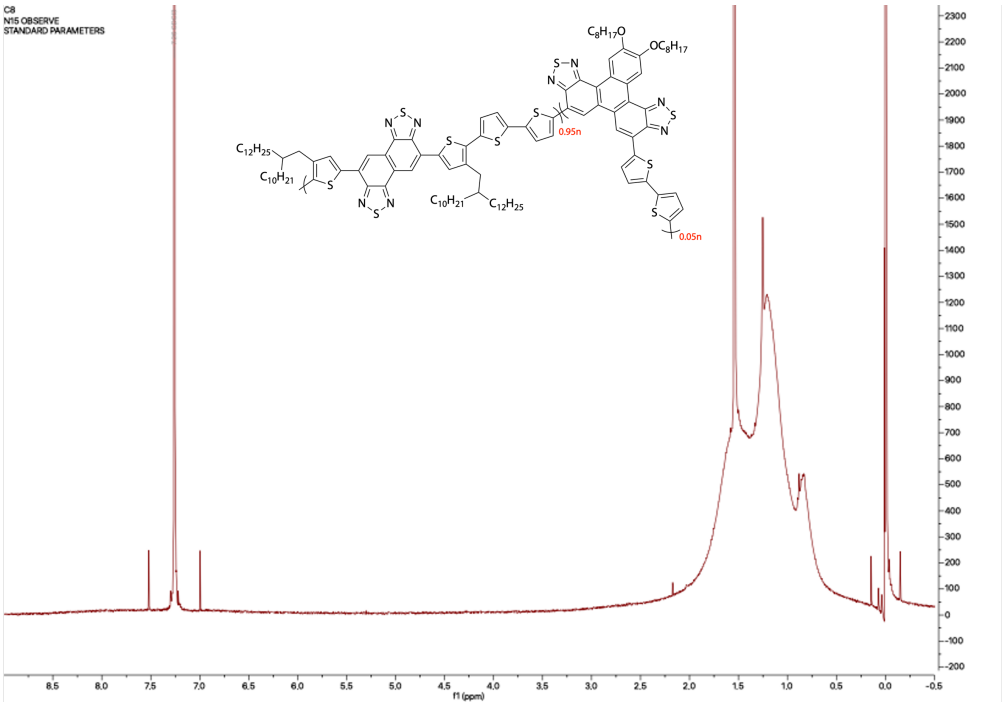

^{1}H-NMR spectrum of **C8-5**.

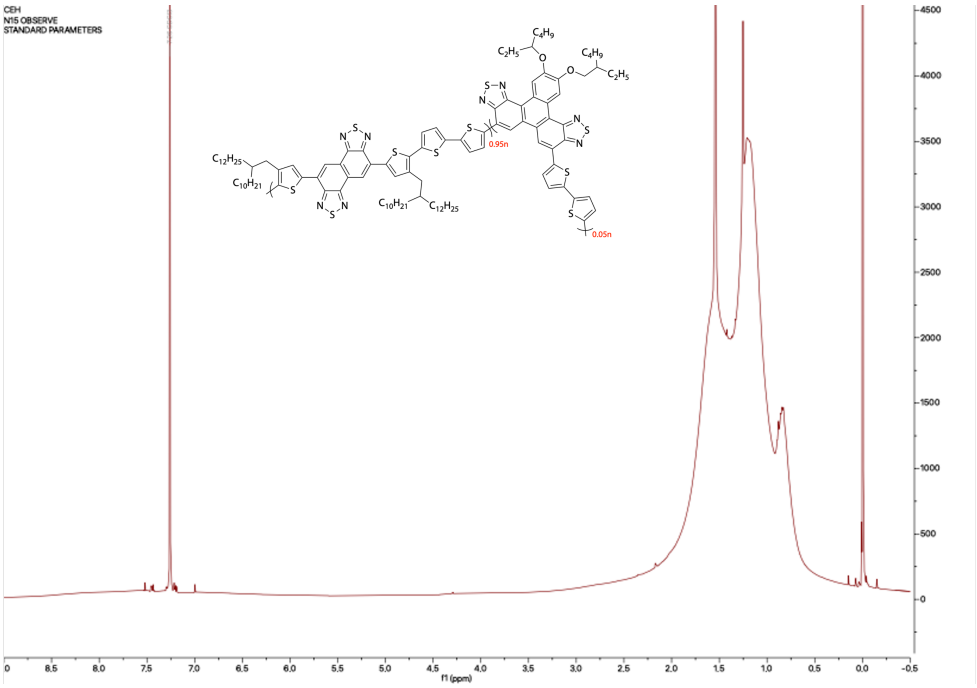

^{1}H-NMR spectrum of **EH-5**.

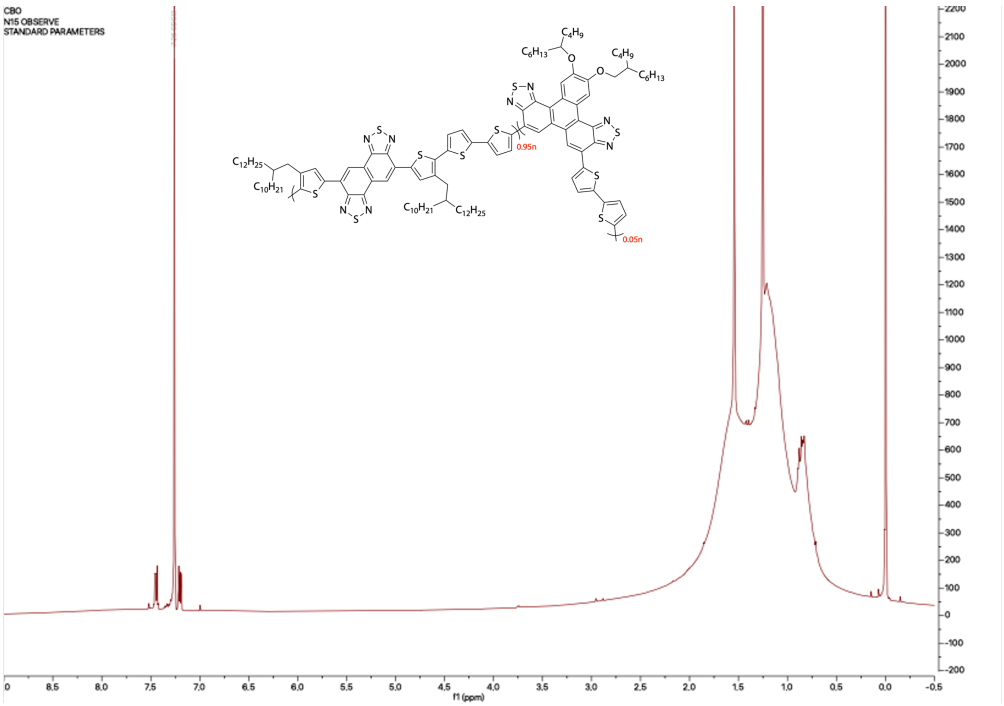

^{1}H-NMR spectrum of **BO-5**.

***C12-x* (x= 2.5, 5, 7.5 & 10%):** NTz2T-Br_2 (0.04875, 0.0475, 0.04625 or 0.045 mmol for 2.5%, 5%, 7.5% or 10%, respectively), A3-CR (0.00125, 0.0025, 0.00375 or 0.005 mmol

for 2.5%, 5%, 7.5% or 10%, respectively), 2T-$(SnMe_3)_2$ (0.05 mmol), $Pd(PPh_3)_4$ (1.16 mg, 2 mol%) and toluene (2 mL) were added to reaction tube, then heated to 200 °C for 2 hours in microwave reactor. After cooling to room temperature, the reaction solution was poured into 50 mL of methanol containing 2 mL of hydrochloric acid and stirred for 1 hour. Then the precipitate was collected sequentially with methanol, hexane, and dichloromethane through Soxhlet extraction to remove the impurities and low-molecular weight fractions. The residue was then extracted with chloroform, and reprecipitated in 50 mL of methanol. The precipitate was collected and dried in vacuum to yield the polymer as dark blue solid (yield: 87% for **C12-2.5**, 91% for **C12-5**, 89% for **C12-7.5** and 93% for **C12-10**).

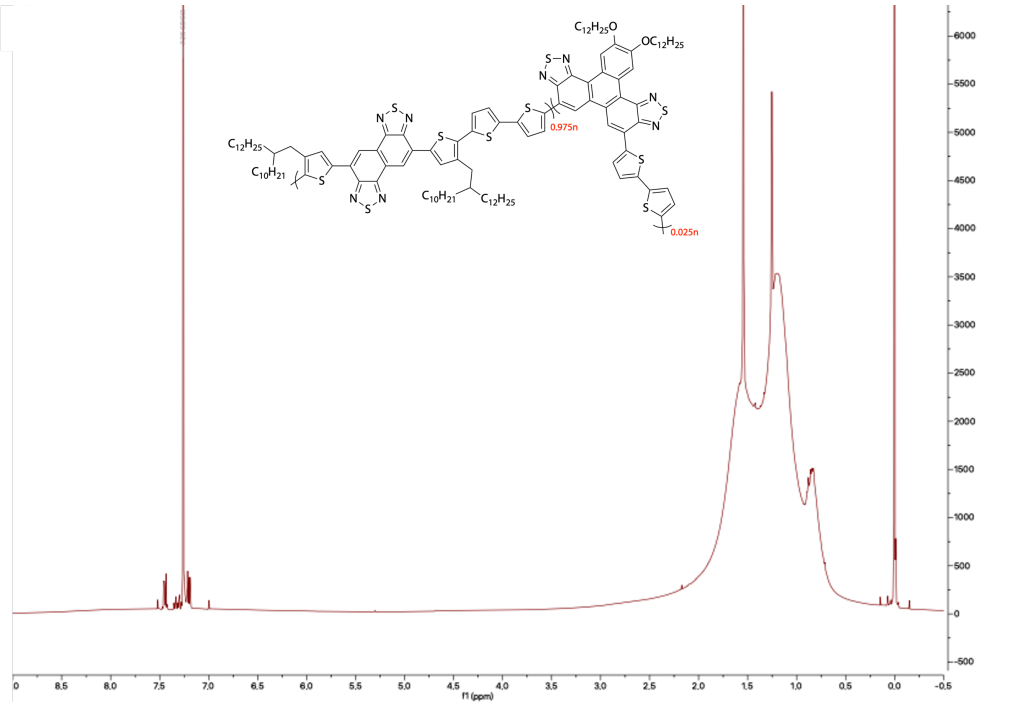

^{1}H-NMR spectrum of **C12-2.5**.

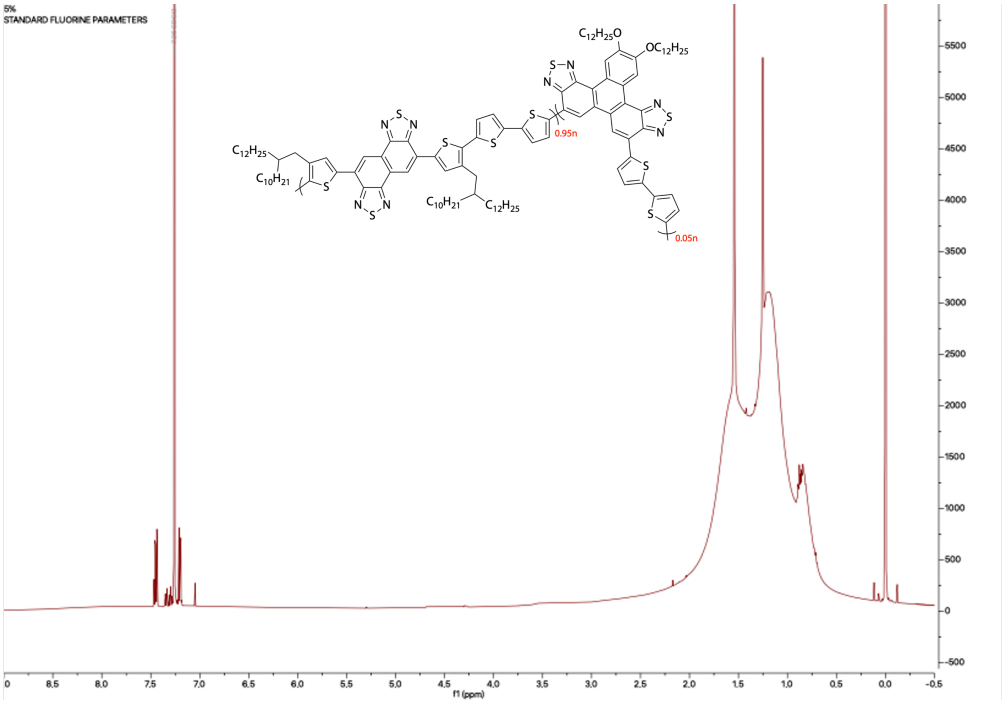

^{1}H-NMR spectrum of **C12-5**.

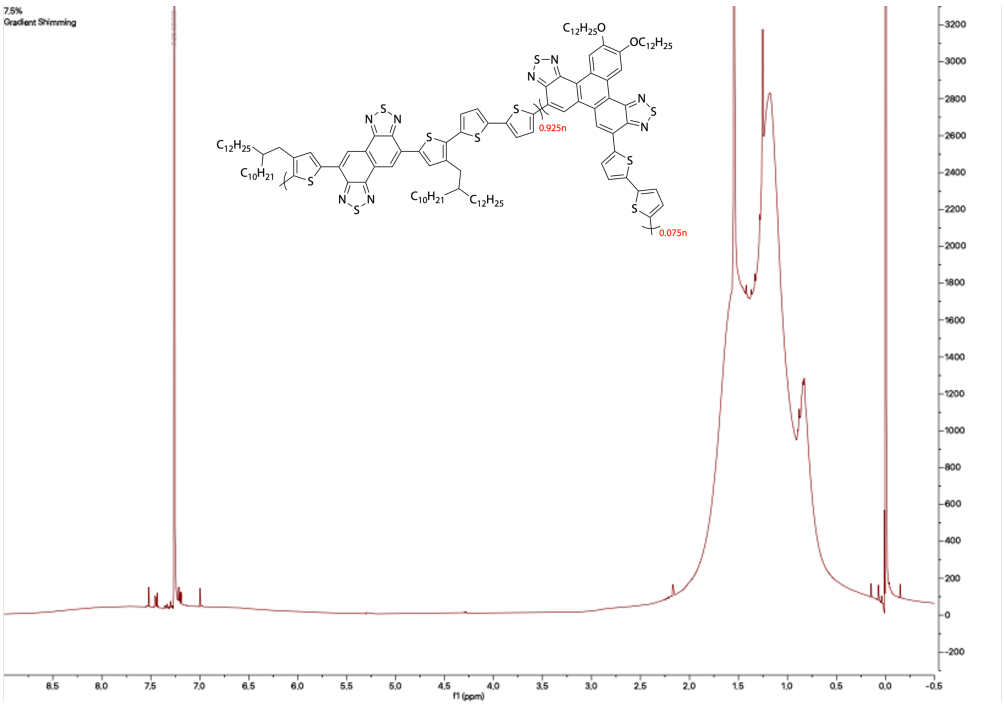

^{1}H-NMR spectrum of **C12-7.5**.

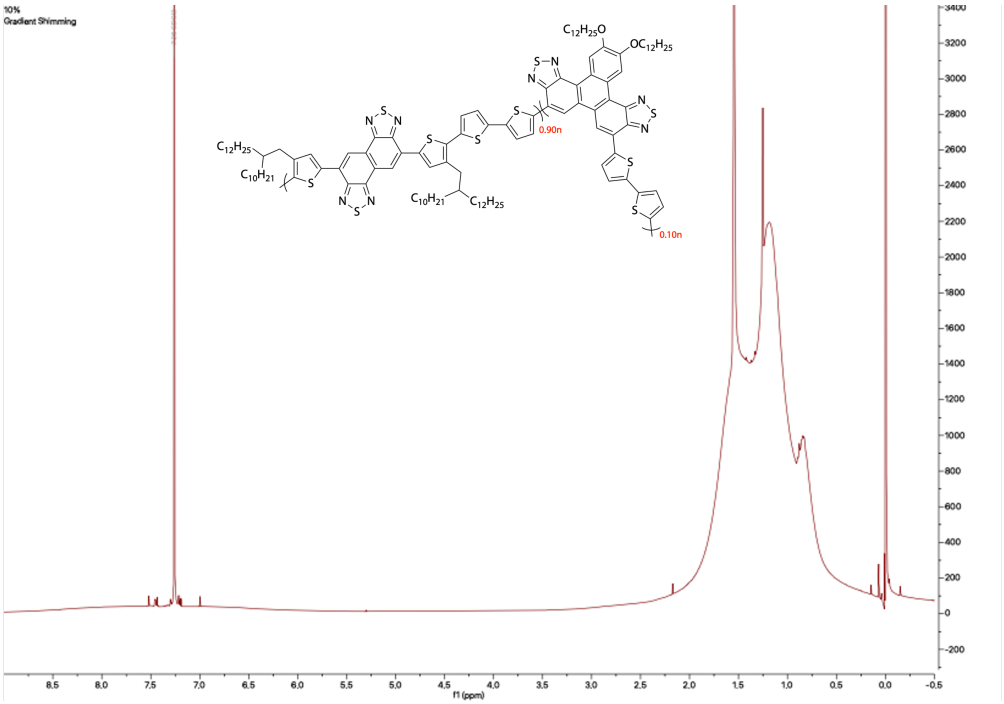

^{1}H-NMR spectrum of **C12-10**.

Table 2 Polymerization results of NTz-TPTz polymers.

Polymer	M_n[a] (g mol^{-1})	M_w[a] (g mol^{-1})	$Đ$
PNTz4T	31,000	110,000	3.5
C8-5	35,000	80,500	2.3
EH-5	33,000	69,300	2.1
BO-5	46,000	96,600	2.1
C12-2.5	35,000	66,500	1.9
C12-5	35,000	94,500	2.7
C12-7.5	36,000	68,400	1.9
C12-10	48,000	86,400	1.8

[a] Determined by high-temperature gel permeation chromatography (GPC) using DCB at 140 °C.

3-2 Solar Cell Fabrication

3-2-1 Solar Cell Fabrication of NTz-BDT Polymers

Indium tin-oxide (ITO) substrates were first pre-cleaned sequentially by sonicating in a detergent bath, deionized water, acetone, and 2-propanol at room temperature, and in boiled 2-propanol for 10 min each, and then baked at 120 °C for 10 min in air. Following the substrates were then subjected to a UV/ozone treatment at room temperature for 20 min. The PEDOT:PSS layer was prepared by spin-coating at 5000 rpm for 30 s then annealed at 120 °C for 10 min. The photoactive layers were fabricated in glove box (KOREA KIYON, KK-011AS-EXTRA) by spin-coating with chloroform solution containing 3.5 mg mL^{-1} of the polymer sample with Y6 (polymer: Y6 = 1:1.2 w/w). The solution was kept at 50 °C for 30 min and the hot solution was spin-coated on the substrate at 600 rpm for 20 s and thermal annealing at 90 °C for 5 min. The thickness of the optimal device was around 100 nm. A PNDI-F3N-Br layer was prepared by spin-coating (1000 rpm, 30 s) with methanol solution at concentration of 0.5 mg mL^{-1} (AcOH 0.5 vol%).

Finally, thin films were transferred to vacuum evaporator (ALS Technology, E-100J) which it is connected to the glove box and Ag (220 nm) were deposited by thermal evaporation under ~10^{-5} Pa, where the active area of the cells was 0.1256 cm^2.

3-2-2 Solar Cell Fabrication of NTz-TPTz Random Copolymers

Indium tin-oxide (ITO) substrates were first pre-cleaned sequentially by sonicating in a detergent bath, deionized water, acetone, and 2-propanol at room temperature, and in boiled 2-propanol for 10 min each, and then baked at 120 °C for 10 min in air. Following the substrates were then subjected to a UV/ozone treatment at room temperature for 20

min. The PEDOT:PSS layer was prepared by spin-coating at 5000 rpm for 30 s then annealed at 120 °C for 10 min. The photoactive layers were fabricated in glove box by spin-coating with chloroform solution containing 3.5 mg mL^{-1} of the polymer sample with Y6 (polymer: Y6 = 1:1.2 w/w, without solvent additive). The solution was kept at 50 °C for 30 min and the hot solution was spin-coated on the substrate at 600 rpm for 20 s and thermal annealing at 90 °C for 5 min. The thickness of the optimal device was around 90-100 nm. Then, ZnO layer was prepared by spin-coating (6000 rpm, 20 s) from a diluted solution of ZnO nanoparticles.

Finally, thin films were transferred to vacuum evaporator which it is connected to the glove box and Ag (220 nm) were deposited by thermal evaporation under ~10^{-5} Pa, where the active area of the cells was 0.1256 cm^2.

3-3 Instrumentation

J-V characteristics of the solar cells were measured using Keithley 2400 source in the glove box under 100 mW cm^{-2} (AM 1.5G) condition using solar simulator (SAN-EI Electric, XES-40S1). The light intensity was calibrated with a reference PV cell (KONICA MINOLTA AK-100 certified at National Institute of Advanced Industrial Science and Technology, Japan). EQE spectra was measured with a Spectral Response Measuring System (Soma Optics, Ltd., S-9241). The thickness of the photoactive layers were measured with an ET200 (Kosaka Laboratory, Ltd.).

UV-vis absorption spectra were measured using a Shimadzu UV-3600 spectrometer. 2D-grazing incidence X-ray diffraction (GIXD) measurements were performed on the beamline BL46XU at the SPring-8. The sample was irradiated at a fixed incident angle on

the order of 0.12° through a Huber diffractometer with an X-ray energy of 12.39 keV (λ = 1 Å).

Two dimensional (2D) GIXD patterns were recorded with a 2D image detector (Pilatus 300K). The polymer neat films were coated on the PEDOT:PSS-coated ITO glass substrate under same conditions that used in device fabrication while the blend thin films were directly used for measurement after device fabrication. Atomic force microscopy (AFM) was carried out with a SPM-9700HT scanning probe microscope (Shimadzu Corp).

3-3-1 Cyclic Voltammetry Measurements

Cyclic voltammetry (CV) measurements were carried out with ALS Electrochemical Analyzer Model 610E, in acetonitrile containing tetrabuthylammonium hexafluorophosphate (Bu4NPF6, 0.1 M) as the supporting electrolyte. The counter and working electrodes were made of Pt while the reference electrode was Ag/Ag^{+}. The polymer thin films were obtained on the working electrode through directly dipping the electrode into the polymer solution. All potentials were calibrated with the standard ferrocene/ferrocenium redox couple (Fc/Fc^{+}: $E^{1/2}$ = + 0.13 V measured under the identical conditions). HOMO energy levels (E_H) and LUMO energy levels (E_L) were calculated through the following equations:

$$E_H \text{ (eV)} = -4.67 - E_{ox}$$

$$E_L \text{ (eV)} = -4.67 + E_{red}$$

where E_{ox} and E_{red} are the onset oxidation and reduction potential of CV, respectively, and −4.80 eV represent the E_H of ferrocene against the vacuum level.

3-3-2 Hole/Electron-Only Device Fabrication & Measurements

For hole-only devices, the pre-cleaned ITO glass were coated with PEDOT:PSS by spin-coating at 5000 rpm for 30 s. The polymer blend film (polymer/Y6=1:1.2) was then deposited through spin-coating as described in solar cell fabrication. Then, they were transferred into vacuum evaporator, and MoO_x (7 nm) and Ag (100 nm) were deposited sequentially through a shadow mask. For electron-only devices, a ZnO layer was prepared on the pre-cleaned ITO glass by spin-coating (1200 rpm) from a diluted solution of ZnO nanoparticles. The polymer blend film was deposited as described. Then, the ZnO layer was directly spin-coated on the photoactive layer. The thin films were transferred into vacuum evaporator and Ag (100 nm) were deposited through a shadow mask under ~10^{-5} Pa.

The *J–V* characteristics were measured in the range of 0–7 V using a Keithley 2400 source–measure unit in the dark in the glovebox. The mobility (μ_{SCLC}) was calculated by fitting the *J–V* curves to a space charge limited current model described by the following equation:

$$J = \frac{8}{9}\varepsilon_r\varepsilon_0\mu_{SCLC}\frac{V^2}{L^3}$$

where ε_r is the relative dielectric constant of the polymer, ε_0 is the permittivity of free space, μ_{SCLC} is the mobility, $V = V_{appl} - V_{bi}$, where V_{appl} is the applied voltage to the device and V_{bi} is the built-in voltage due to the difference in work function of the two electrodes (determined to be 0.1 V), and L is the polymer thickness. The dielectric constant ε_r is assumed to be 3, which is a typical value for semiconducting polymers.

CHAPTER 4 PNTz4T in Non-Fullerene Solar Cells

PNTz4T, as a novel semiconductive polymer, exhibited a crystalline structure with the face-on orientation in the **PNTz4T**:$PC_{71}BM$ blend film, resulting in a PCE of approximately 10% in the fullerene solar cell.[17, 48] The emergence of the so-called Y-series of acceptors is the latest impetus to further push OPVs.[12, 64] In 2019, Zou *et al*. first reported Y6 (Figure 13) as a new class of near-infrared (NIR)-absorbing NFA material based on a multifused ring central unit with an electron-deficient benzothiadiazole unit.[12] Solar cells based on Y6 and polymer, PM6[15] , exhibited low energy losses and achieved a PCE of 15.7%. Y6 was also compatible with other polymer donor materials.[16, 65-68] Therefore, to understand the role of **PNTz4T** in the non-fullerene solar cell, we investigated **PNTz4T** in combination with Y6.

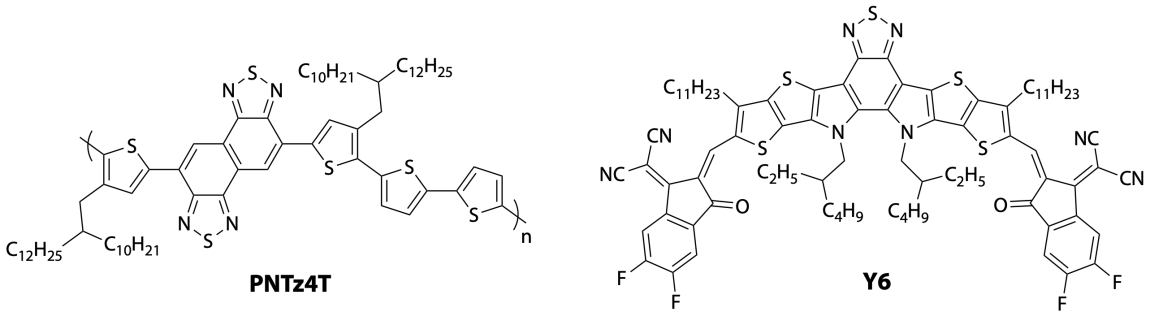

Figure 13 Chemical structure of semiconducting polymer, **PNTz4T**; and non-fullerene acceptor Y6.

The ultraviolet–visible (UV–vis) absorption spectra for **PNTz4T** in the polymer thin films are shown in Figure 14. The absorption of Y6 is shown in the thin film spectra. The **PNTz4T** thin film offered a spectrum with the main absorption band ≈ 500–800 nm,

whereas **Y6** offered a spectrum in a longer wavelength with the main absorption band ≈ 600–900 nm. **PNTz4T** exhibited λ_{max} = 714 nm, in which a 0–0 band was observed, indicating good molecular ordering, probably due to the rigid π-extended structure. The absorption onset in the thin film for **PNTz4T** was 776 nm, and E_g was calculated to be 1.60 eV. To effectively harvest the solar energy, the optical absorption of the active layer in the polymer organic solar cells must optimally match the region of the maximum photon flux. As shown in Figure 14, the main absorption band for **PNTz4T** and Y6 was rather overlapped, which affected the light harvesting, thereby lowering the J_{SC}.

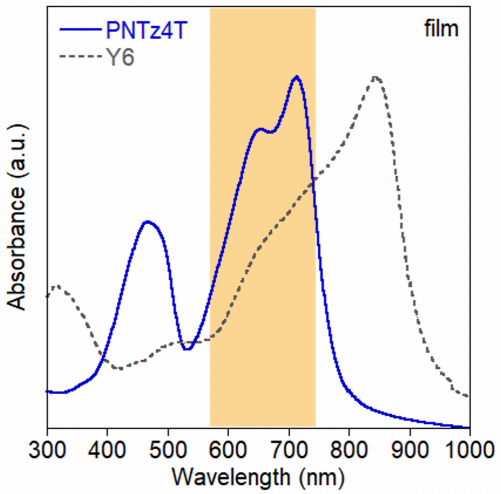

Figure 14 UV-vis absorption spectra of the **PNTz4T** thin film. The absorption of Y6 is also shown in the thin film spectra.

The E_{HOMO} and E_{LUMO} of **PNTz4T** and Y6 were estimated by conducting cyclic voltammetry (CV) using the thin films. **PNTz4T** had an E_{HOMO} and E_{LUMO} of −5.20 and −3.46 eV, respectively, whereas Y6 had an E_{HOMO} and E_{LUMO} of −5.62 and −4.11 eV. The V_{OC} linearly correlated with the difference between the E_{HOMO} of the donor and the E_{LUMO}

of the acceptor.[69] Narrowing the E_g of the polymer while maintaining a proper driving force for charge separation would minimize the E_{loss}, resulting in the maximum value of the V_{OC}.[24] The mismatch of the energy level of **PNTz4T** and Y6 would lead to a poor V_{OC}.

The photovoltaic performances of **PNTz4T** were investigated by fabricating the devices with a conventional architecture (ITO/PEDOT:PSS/**PNTz4T**/Y6/PNDI-F3N-Br/Ag). The optimal weight ratio of **PNTz4T** to **Y6** was observed to be 1:1.2, and the optimized thickness of the active layer was within a range of 90–100 nm. Figure 15 shows the representative current density versus voltage ($J-V$). **PNTz4T** exhibited a V_{OC} of 0.71 V, J_{SC} of 23.4 mA cm^{-2}, and FF of 67%, thereby achieving a PCE of 11.1%. As expected from the energy level mismatch, the V_{OC} was rather low in organic solar cells.

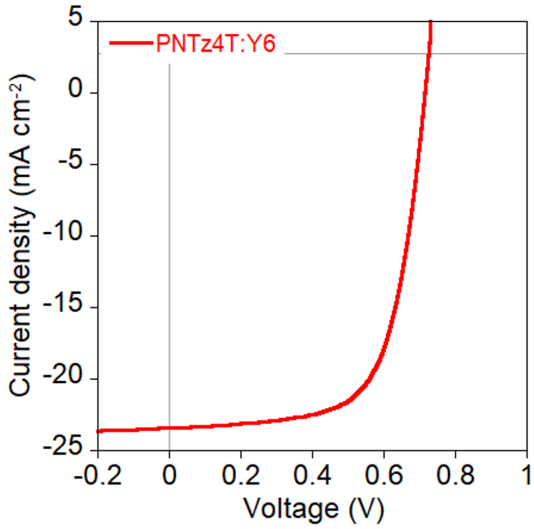

Figure 15 $J-V$ curves of the optimized organic solar cells using the **PNTz4T** combined with Y6.

The solubility of **PNTz4T** is an issue because it was soluble in hot chloroform (CF), which hampered the solution-processability, owing to its high crystallinity. In addition, it further

affected the miscibility with the acceptor whether with Y6 or other acceptor materials. Therefore, it is necessary to design a new series of polymers based on the NTz unit with the appropriate energy level for a high V_{OC} with a short wavelength absorption band and good solubility.

Subsequently, we demonstrated a new series of NTz-based polymers, NTz-BDT polymers (Chapter 5) and NTz-TPTz random copolymers (Chapter 6), which exhibited better performances in non-fullerene solar cells. The optical and electrochemical properties, photovoltaic performances, polymer packing, and film morphology were investigated and are discussed herein.

CHAPTER 5 NTz-BDT Polymers

It is unsatisfactory that these low solubilities in π-conjugated polymers would limit the solution-processability and miscibility with acceptor materials, in particular, non-fullerenes, resulting in poor photovoltaic performances. To develop highly soluble polymers, benzo[1,2-*b*:4,5-*b*′]dithiophene (BDT) is important as a high-potential D unit.[70-71] BDT possesses a planar conjugated structure, thereby [70, 72-73] allowing the attachment of various side chains at the 4 and 8 positions to relatively easily tune the solubility. Thus, we expected that the introduction of a BDT unit in the polymer backbone would endow the NTz-based polymers with high solubility, thereby ensuring high photovoltaic performances in non-fullerene cells. [62, 74-76]

Here, we synthesized a series of NTz-based polymers with BDT units that possess alkylthienyl substituents, named **PNTzBDT** and **PNTzBDT-F** and **PNTzBDT-Cl** containing fluorine and chlorine groups in the alkylthienyl side chain, respectively (Figure 16). The alkylthienyl side chains provided torsion with respect to the BDT moiety, owing to the steric repulsion from the peripheral hydrogen atom, which reduced the intermolecular interaction between the backbones. As a result, these NTz-BDT polymers exhibited significantly improved solubility, compared with **PNTz4T**. In addition, they had slightly wider E_g and deeper HOMO energy levels because of the weaker electron-donating nature of BDT, compared with that of oligothiophenes; halogenation further deepened the HOMO energy level. As a result, the photovoltaic parameters of the cells based on the NTz-BDT polymers, where Y6 was blended, simultaneously improved relative to that based on **PNTz4T**.

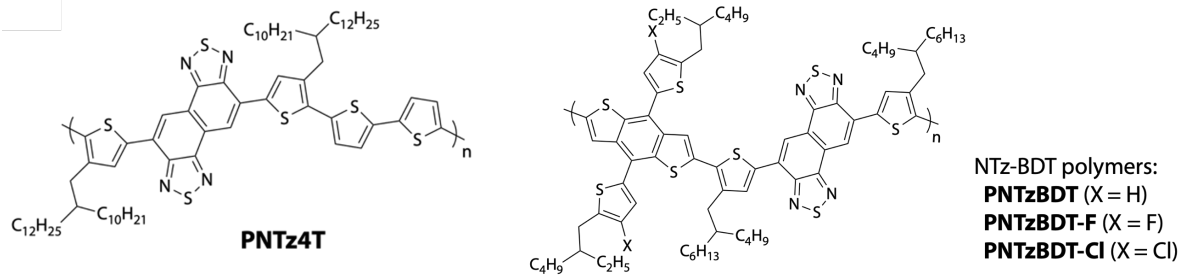

Figure 16 Chemical structure of **PNTz4T** and NTz-BDT polymers, i.e., **PNTzBDT, PNTzBDT-F** and **PNTzBDT-Cl**.

The synthetic route for the NTz-BDT polymers is shown in Scheme 2, where the BDT-containing monomers (**1**–**3**) were copolymerized with the NTz-containing monomer (**4**) via the Stille coupling reaction to yield the corresponding copolymers, **PNTzBDT**, **PNTzBDT-F**, and **PNTzBDT-Cl**, at yields in the range of 80%–90%. The number-average and weight-average molecular weights (M_n and M_w) of the polymers are summarized in Table 1. The polymers had M_n values within the range of 40000–60000 with polydispersities ($Đ$) of approximately 2.0. In addition, they were soluble in CF even at room temperature. **PNTz4T** was also synthesized according to our previous report.[48] Notably, the molecular weight of **PNTz4T** was controlled by modifying the synthetic conditions to be soluble in CF to fabricate the solar cells under conditions similar to those of the NTz-BDT polymers. **PNTz4T** had an M_n of 34200 ($Đ$ = 2.5) and was soluble in hot CF. Typically, **PNTz4T** is obtained with a high M_n of over 50000 and is soluble in hot CB (insoluble in CF). Thus, the NTz-BDT polymers had a significantly improved solubility than **PNTz4T**.

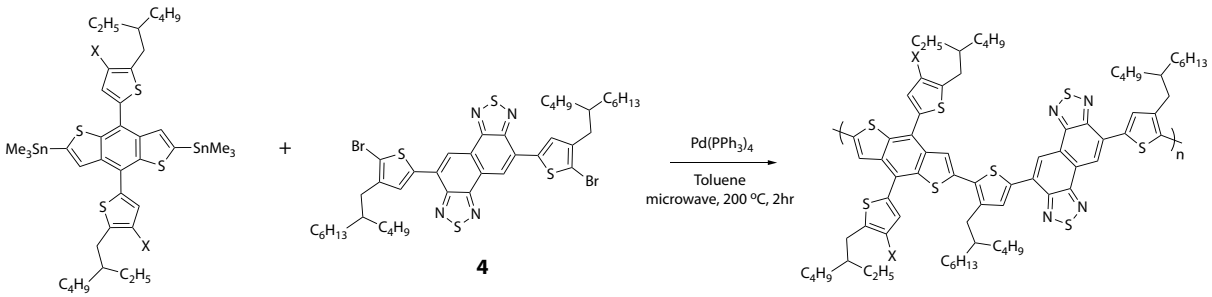

1 (X = H)
2 (X = F)
3 (X = Cl)

PNTzBDT (X = H)
PNTzBDT-F (X = F)
PNTzBDT-Cl (X = Cl)

Scheme 2. Synthetic route to the NTz-BDT polymers.

5-1 Physical Property Evaluation

The chemical structure of **PNTz4T** and the NTz-BDT polymers are shown in Figure 16. The use of the alkylthienyl chain on the BDT moiety provided the torsion of the peripheral thienyl rings relative to BDT, which reduced the intramolecular interaction, thereby increasing the solubility. The NTz-BDT polymers were soluble in CF solvent at room temperature, whereas **PNTz4T** needed to be dissolved in hot CF, which might have affected the solution processability. The thermal properties of these polymers were examined by differential scanning calorimetry (DSC) (Figure 17). The DSC curves showed that **PNTzBDT**, **PNTzBDT-F**, and **PNTzBDT-Cl** had no melting peak and phase-transition peaks below 350 °C, whereas **PNTz4T** exhibited a melting peak at 317 °C. This implied that the polymers were thermally stable in this temperature range.

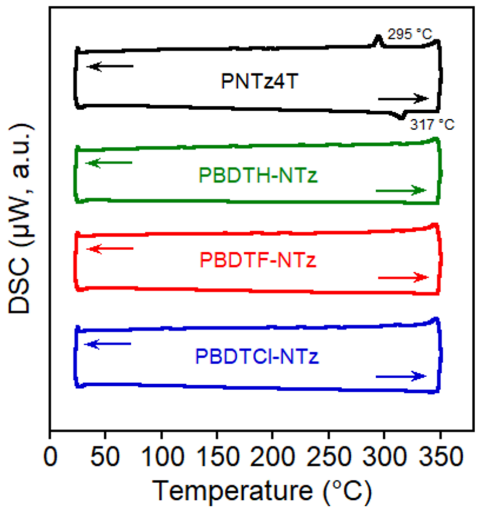

Figure 17 DSC thermograms of **PNTz4T** and NTz-BDT polymers.

The UV–VIS absorption spectra of the solution and polymer thin films are presented in Figure 18. The absorption maximum (λ_{max}), absorption edge (λ_{edge}), and optical bandgap (E_g^{opt}) were calculated and are summarized in Table 3. The polymers exhibited a spectrum with the main absorption band ≈ 500–800 nm. In the polymer solution (Figure 18a), the NTz-BDT polymers exhibited spectra with a broad single peak, where λ_{max} was approximately 650 nm. However, **PNTz4T** exhibited a relatively sharp peak with a λ_{max} of 716 nm assignable to the 0–0 transition band along with a shoulder at approximately 650 nm assignable to the 0–1 band. The change in the absorption shape of the NTz-BDT polymers, compared with that of **PNTz4T**, was probably due to the enhancement of the linkage rotation along the backbone originating in a higher solubility and suppressed intermolecular interactions. **PNTzBDT-Cl** exhibited a blue-shifted spectrum, compared with those of **PNTzBDT** and **PNTzBDT-F**, which could be correlated with the shift of the energy levels, as discussed below. In the thin film (Figure 18b), the NTz-BDT polymers exhibited absorption spectra similar to those in the solution, whereas **PNTz4T** exhibited a spectrum that was more sharpened, compared to that in the solution. This suggested that the aggregation was significantly suppressed by the introduction of the BDT unit in the backbone.

The HOMO and LUMO energy levels (E_{HOMO} and E_{LUMO}) of the polymers were estimated by conducting CV using the polymer thin films (Figure 18c). **PNTzBDT** exhibited an E_{HOMO} and E_{LUMO} of −5.26 and −3.46 eV, respectively, in which the E_{HOMO} slightly downshifted from that of **PNTz4T** (−5.20 eV). The E_{LUMO} remained unchanged, resulting in a larger HOMO–LUMO gap, compared with that of **PNTz4T**. This suggested that the replacement of the bithiophene moiety with the BDT moiety had a greater

influence on the E_{HOMO} than on the E_{LUMO}. The E_{HOMO} and E_{LUMO} of **PNTzBDT-F** (−5.36 and −3.56 eV) and **PNTzBDT-Cl** (−5.41 and −3.60 eV) were observed to be lower than those of **PNTzBDT**. This can be explained by the effect of the electron-withdrawing nature of the fluorine and chlorine groups on the alkylthienyl sidechains. These trends in the energy levels correlated with the results obtained by the density functional theory (DFT) calculation (B3LYP/6-31g(d)) using the model compounds (Figure 19).

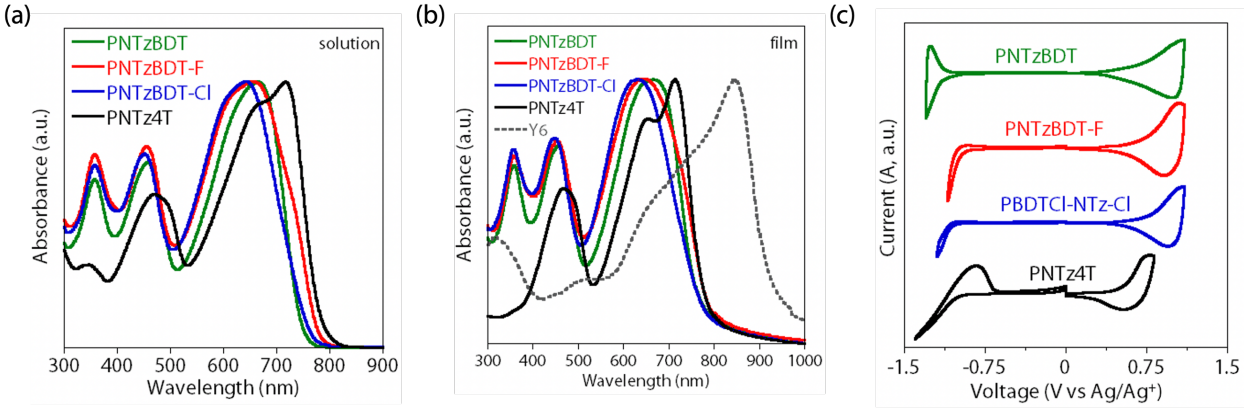

Figure 18 (a,b) UV-vis absorption spectra of the NTz-BDT polymers in the solution (a) and thin film (b). The absorption of Y6 is also shown in the spectra. (c) CV of the thin films for the NTz-BDT polymers vs Ag/Ag^+ as the reference electrode.

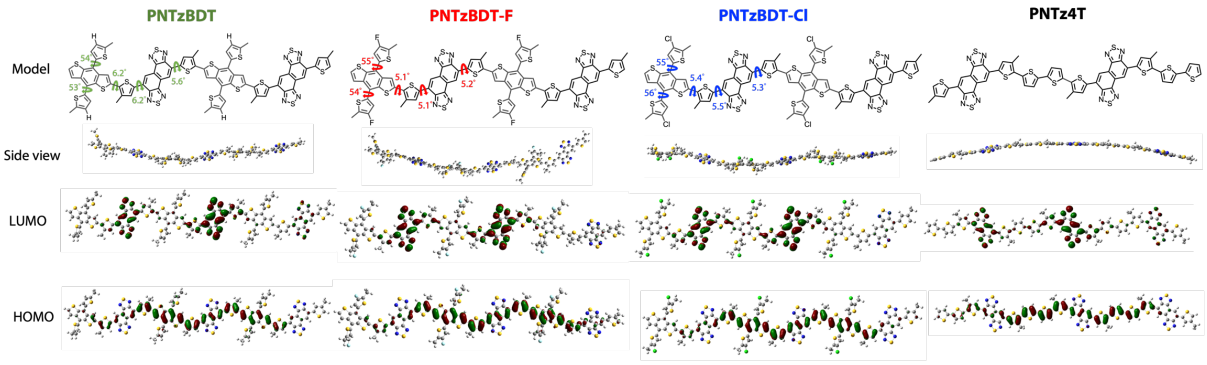

Figure 19 Optimized geometry of the polymer backbone, and E_{LUMO}s and E_{HOMO}s for the compounds calculated by the density functional theory (DFT) method at the B3LYP/6-31G(d) level.

Table 3 Optical and electrochemical properties of the polymer thin films.

Polymer	λ_{max} (nm)[a]		λ_{edge} (nm)[b]	E_g^{opt} (eV)[c]	E_{LUMO} (eV)[d]	E_{HOMO} (eV)[d]
	solution	film				
PNTzBDT	664	666	762	1.63	−3.46	−5.26
PNTzBDT-F	657	643	786	1.58	−3.56	−5.36
PNTzBDT-Cl	643	628	776	1.60	−3.60	−5.41
PNTz4T	716	657, 714	776	1.60	−3.46	−5.20

[a]Absorption maximum. [b]Absorption onset. [c]Optical bandgap determined from the absorption onset. [d]E_{HUMO} and E_{LUMO} determined by the onset oxidation and reduction potential of the cyclic voltammograms, respectively,

5-2 OPV Properties of NTz-BDT Polymers in Non-Fullerene System

The photovoltaic performances of the NTz-BDT polymers and **PNTz4T** were investigated by fabricating organic solar cells with conventional architecture (ITO/PEDOT:PSS/polymer/Y6/PNDI-F3N-Br/Ag). The optimal weight ratio of polymer/**Y6** was 1:1.2, and the optimal active layer thickness was ≈ 90–100 nm. The representative *J*–*V* characteristic and the EQE of the optimized devices are shown in Figures 20a and b, respectively, and the corresponding parameters including the V_{OC}, J_{SC}, FF, and PCE are summarized in Table 4. As expected from the deeper E_{HOMO} of **PNTzBDT**, the device exhibited a higher V_{OC} of 0.77 V, compared to that of the **PNTz4T** device (0.71 V). Moreover, the E_{HOMO} shifted deeper by the halogenation alkylthienyl side chain of the BDT moiety. **PNTzBDT-F** and **PNTzBDT-Cl** exhibited significantly improved V_{OC} values of 0.79 and 0.83 V, respectively. **PNTzBDT-F** exhibited a J_{SC} of 24.5 mA cm^{-2}, which was slightly higher than those of **PNTzBDT** (24.0 mA cm^{-2}) and **PNTz4T** (23.4 mA cm^{-2}). The slight difference between **PNTzBDT-F** and **PNTz4T** for the J_{SC} might be attributed to the blueshift of the absorption that offered a better combination with **Y6**, and this was consistent with the results of the EQE investigation. Nevertheless, the **PNTzBDT-F** devices achieved a PCE of 13.3%, which was higher than those of the **PNTz4T** (11.1%) and **PNTzBDT** devices (12.6%). Although the **PNTzBDT-Cl** devices exhibited good performances for the V_{OC} over 0.80 V, it was discovered that the poor J_{SC} and FF mainly restricted the device performances, resulting in a low PCE of 10.3%.

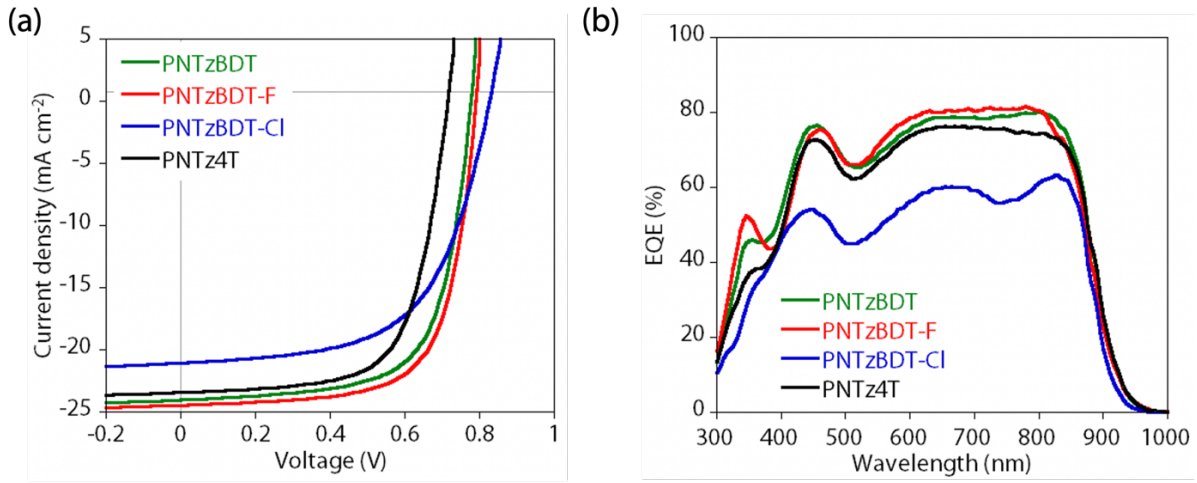

Figure 20 (a) *J*−*V* curves and (b) EQE spectra of the optimized organic solar cells using the NTz-BDT polymers combined with Y6.

Table 4 Summary of photovoltaic parameters of the optimized polymer/Y6 devices.

Polymer	V_{OC} (V)	J_{SC} [J_{SC}^{EQE}]^a (mA cm^{-2})	FF (–)	PCE_{max} [PCE_{ave}] (%) ^{b}
PNTzBDT	0.77	24.0 [24.2]	0.68	12.6 [11.9 ± 0.8]
PNTzBDT-F	0.79	24.5 [24.4]	0.69	13.3 [12.9 ± 0.4]
PNTzBDT-Cl	0.83	21.0 [18.1]	0.60	10.3 [10.0 ± 0.5]
PNTz4T	0.71	23.4 [21.6]	0.67	11.1 [10.4 ± 0.6]

$^a J_{SC}$ calculated from the EQE spectrum ^{b}Maximum PCE and the average PCE, obtained from more than 10 cells, with standard deviation in the square bracket.

5-3 Reason for the Differences in OPV Performances

5-3-1 Charge Transport Ability

The charge carrier mobilities of the blend films were evaluated based on the space-charge limited current (SCLC) model to correlate with the performance. Hole-only and electron-only devices with device structures of ITO/PEDOT:PSS/active layer/MoO_x/Ag and ITO/ZnO/ active layer /ZnO/Ag, respectively, were prepared. Typical *J–V* curves of the hole-only and electron-only devices are shown in Figure 21. According to the Mott–Gurney equation, the hole mobility (μ_h) for the **PNTzBDT**/**Y6** blend film was observed to be 4.2×10^{-4} cm^2 V^{-1} s^{-1}, which was slightly higher than that of the **PNTz4T**/**Y6** blend film (3.3×10^{-4} cm^2 V^{-1} s^{-1}). Although the **PNTzBDT-F**/**Y6** blend film exhibited a slightly higher μ_h (5.3×10^{-4} cm^2 V^{-1} s^{-1}) than the **PNTzBDT**/**Y6** blend film (4.2×10^{-4} cm^2 V^{-1} s^{-1}), the **PNTzBDT-Cl**/**Y6** exhibited a slightly lower μ_h (3.1×10^{-4} cm^2 V^{-1} s^{-1}). These data were consistent with the trend in the performances, although the difference may be insignificant. The electron mobilities (μ_e) of **PNTz4T**/**Y6**, **PNTzBDT**/**Y6**, **PNTzBDT-F**/**Y6**, and **PNTzBDT-Cl**/**Y6** were 4.5×10^{-4}, 6.2×10^{-4}, 8.4×10^{-4} and 5.8×10^{-4} cm^2 V^{-1} s^{-1}, respectively. The electron mobilities were similar for **PNTz4T**/Y6 and the NTz-BDT polymer/**Y6**, which was reasonable because the major electron carrier in the device was **Y6**.

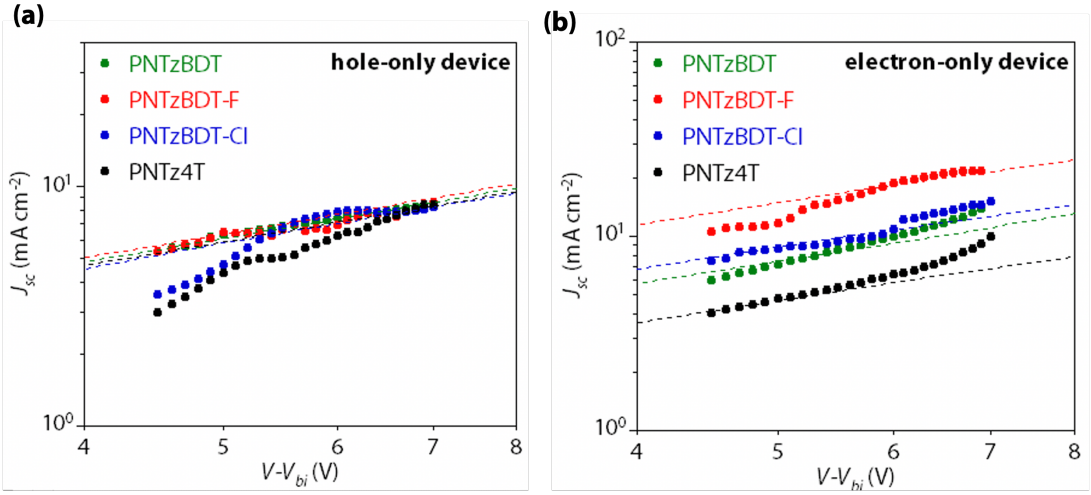

Figure 21 *J*–*V* curves of the (a) hole-only devices; and (b) electron-only devices using the polymer/Y6 blend films based on the space-charge limited current (SCLC) model.

5-3-2 Charge Recombination Behavior

Charge recombination is a crucial factor that affects photovoltaic performance. Thus, we investigated the devices by probing the dependence of J_{SC} and V_{OC} on the light intensity (P_{light}). Figure 22a shows the light-intensity dependence of J_{SC}. According to the following equation, $J_{SC} \propto P_{light}{}^{\alpha}$,[77-78] an α value closer to 1 indicates that the charge carriers can be efficiently collected at the electrodes by avoiding bimolecular recombination, whereas an α value varying from 1 indicates that bimolecular recombination is not negligible under the short-circuit condition that the charge carrier can be efficiently collected at the electrode. As shown in Figure 22a, the devices showed similar α values in the range of 0.98–1.01, suggesting that the bimolecular recombination was not serious and that there was no significant difference between these devices.

Figure 22b illustrates the light-intensity dependence of the V_{OC}, which can be used to analyze trap-assisted recombination. The V_{OC} was fitted to the linear law, $V_{OC} \propto nk_BT/q\ln(P_{light})$,[78-79] where k_B, q, and T are the Boltzmann constant, elementary charge,

and Kelvin temperature, respectively. Factor n for the V_{OC}–ln(P_{light}) plot being equal to 1 suggested that the trap-assisted recombination was negligible; however, n deviating from 1 suggested that the trap-assisted recombination existed under the open-circuit condition. As shown in Figure 22b, the **PNTzBDT** device exhibited an n of 1.41 that was slightly closer to 1, compared with that for the **PNTz4T** device (1.48), indicating that the trap-assisted recombination slightly reduced. This correlated with the fact that the **PNTzBDT** device exhibited a slightly larger FF than that of the **PNTz4T** device. Furthermore, although the **PNTzBDT-F** devices exhibited an n considerably closer to 1 (1.18), the **PNTzBDT-Cl** device exhibited an n significantly farther from 1 (1.83*)*, which correlated with the variation in the FF.

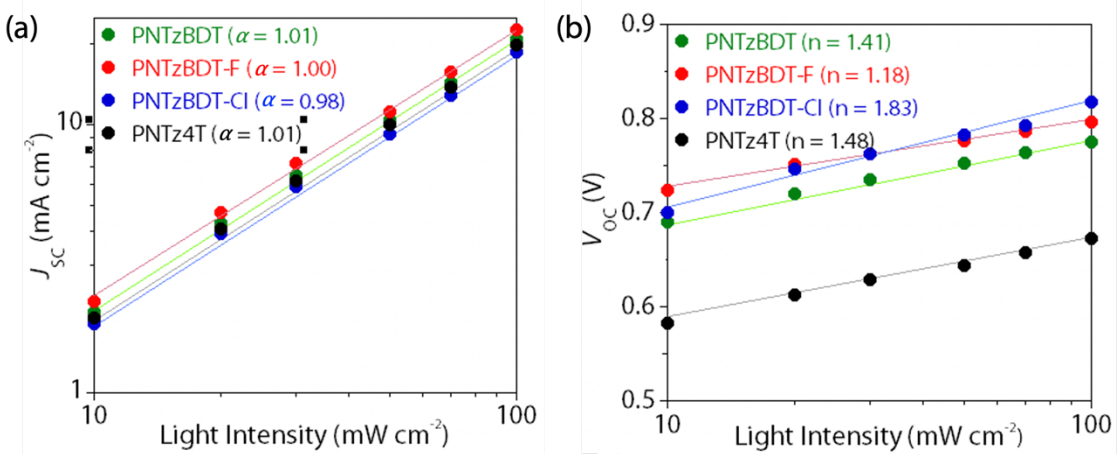

Figure 22 Light-intensity-dependence of (a) J_{SC} and (b) V_{OC} for the polymer/Y6 devices.

5-3-3 Thin-Film Structure

To understand the differences in the photovoltaic performances, we conducted grazing-incidence wide-angle X-ray scattering (GIWAXS) measurements and studied the structural order of the materials, such as the backbone orientation and packing. Figures 23a–d depict the two-dimensional (2D) diffraction patterns of the polymer neat films, and the corresponding diffraction profiles along the q_z and q_{xy} axes extracted from the 2D patterns are shown in Figure 23i. For the **PNTz4T** neat film (Figure 23a), diffractions assignable to the lamellar (h 0 0) and π–π stacking (0 1 0) structures were observed along the ~ q_z and q_{xy} axes, respectively, as previously reported, suggesting that the polymer formed the edge-on orientation. For the NTz-BDT polymers, contrarily, the lamellar and π–π stacking diffractions were observed along the q_{xy} and ~ q_z axes, respectively, indicating the face-on orientation. These results indicated that the use of alkylthienyl-BDT as a donor unit made the polymer backbone oriented parallel to the substrate plane. This probably originated from the weaker intermolecular interactions in the NTz-BDT polymers, compared with that of **PNTz4T**, probably because the bulky alkylthienyl side chains on the BDT unit was twisted from the backbone plane. This was evident because the d-spacing for the π–π stacking (d_π) of the NTz-BDT polymers (3.7–3.9 Å) was significantly wider than that for **PNTz4T** (3.54 Å). Furthermore, the NTz-BDT polymers provided smaller coherence length (L_C) for the π–π stacking (16–18 Å), calculated using the Scherrer's equation, compared with that for **PNTz4T** (32 Å). This result was reasonable because the torsion of the alkylthienyl side chain with respect to the BDT unit might have affected the intramolecular interaction, thereby decreasing the polymer crystallinity. Notably, halogenated polymers, **PNTzBDT-F** and **PNTzBDT-Cl**, had d_π

values of 3.71 and 3.81 Å, respectively, which were shorter than that of **PNTzBDT** (3.91) Å. This was probably because the halogenation induced the local dipole, owing to their electron-withdrawing nature, which enhanced the intermolecular interaction.

The 2D GIWAXS patterns of the polymer/**Y6** blend films are shown in Figures 23e–h, and the corresponding diffraction profiles are shown in Figure 23j. The blend thin films exhibited a π–π stacking diffraction along the q_z axis. Thus, it was assumed that the orientation of **PNTz4T** changed to the face-on orientation in the blend film, which was also observed when **PNTz4T** was blended with PCBM. Here, the d_π observed for the blend films of the NTz-BDT polymers were approximately 3.6 Å, which was significantly shorter than that observed for the neat film (3.7–3.9 Å) and was similar to that observed for the **Y6** neat film (3.60 Å) (Figure 24). Therefore, the π–π stacking diffraction observed for the blend films of the NTz-BDT polymers were assignable to that of **Y6**. This indicated that the NTz-BDT polymers were possibly amorphous in these blend films. For **PNTz4T**, in contrast, the d_π observed for the neat and blend films were practically unchanged at approximately 3.6 Å. Thus, we assumed that the π–π stacking diffraction of **PNTz4T** and **Y6** overlapped in the blend film. Therefore, it was difficult to compare the crystallinity of the blend films for **PNTz4T** and the NTz-BDT polymers. Although we can compare the crystallinity of **Y6** in the blend films of the NTz-BDT polymers, the L_C values of the π–π stacking of **Y6** were practically the same for all the blend films of **PNTzBDT** (19 Å), **PNTzBDT-F** (20 Å), and **PNTzBDT-Cl** (18 Å).

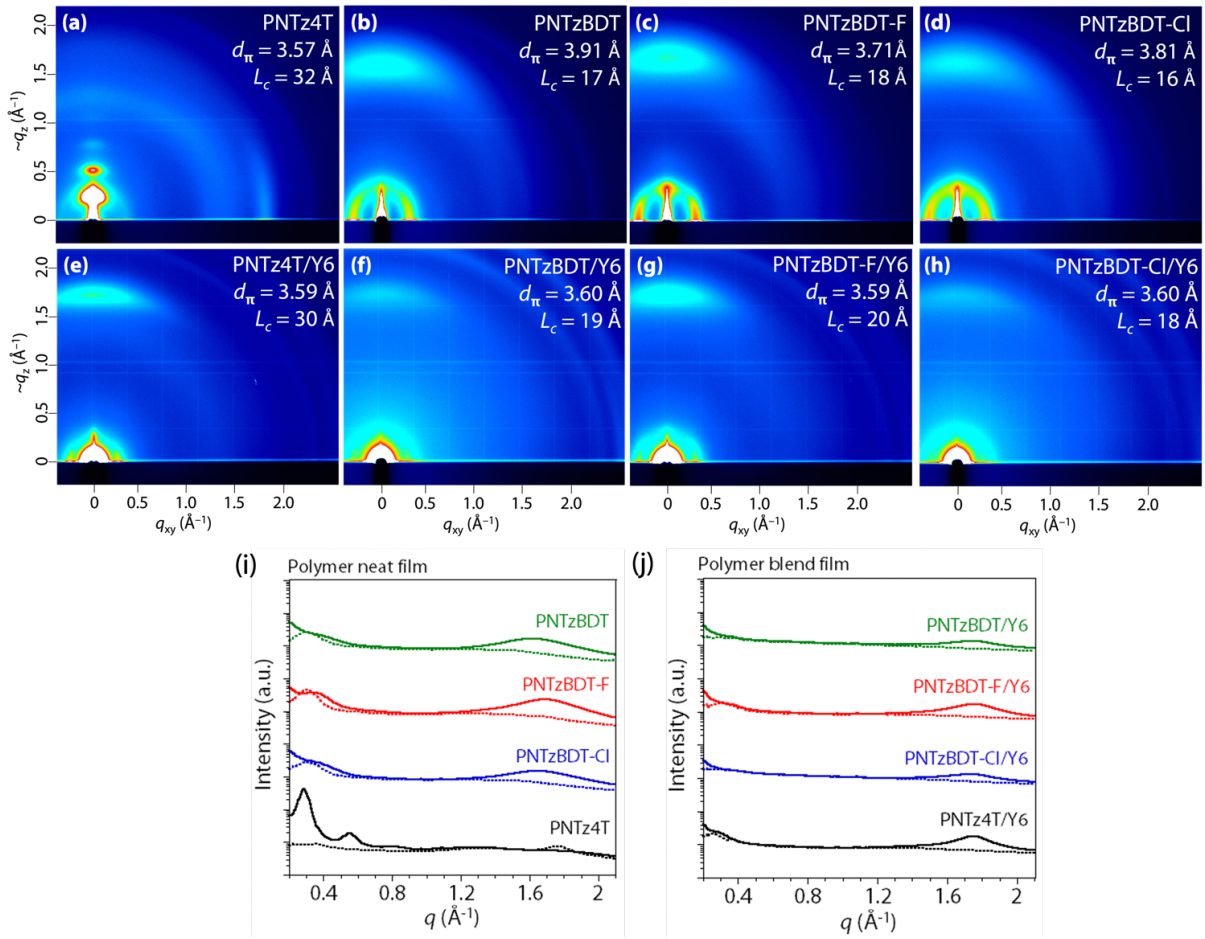

Figure 23 GIWAXS patterns of (a-d) polymer neat films and, (e-h) polymer/Y6 blend films. Corresponding intensity profiles along the out-of-plane (solid line) and in-plane (dotted lines) direction of (i) polymer neat films and, (j) polymer/Y6 blend films.

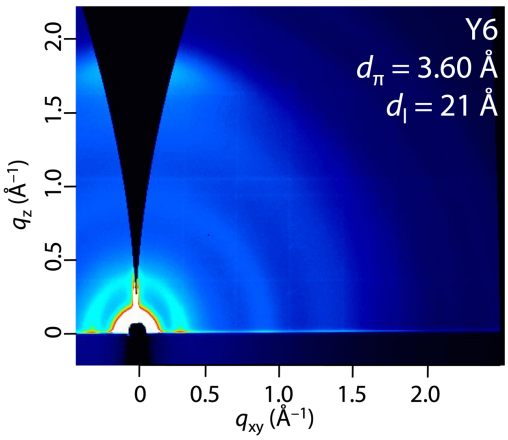

Figure 24 GIWAXS patterns of Y6 non-fullerene acceptor neat film.

Subsequently, we conducted transmission electron microscopy (TEM) to investigate the morphology of the blend films (Figures 25a–d). The **PNTz4T/Y6** and **PNTzBDT/Y6** blend films formed similar fibrillar structures with fine networks as typically observed in many blend systems that provide high photovoltaic performances. This facilitated exciton dissociation and charge transport, although **PNTz4T** and **PNTzBDT** exhibited a rather distinct solubility. For the halogenated polymers, the **PNTzBDT-F/Y6** blend film also exhibited a similar morphology, and the **PNTzBDT-Cl/Y6** blend film exhibited large aggregations, which might have been detrimental to their photovoltaic performance. Therefore, the difference in the photovoltaic performance between **PNTz4T** and the NTz-BDT polymers cannot be well explained by TEM. The low performance for the **PNTzBDT-Cl** can be ascribed to the large aggregations. We performed atomic force microscopy (AFM) to further investigate the morphology of the blend films (Figures 25e–h). The blend films of the NTz-BDT polymers exhibited smaller domains with smoother surfaces than those of the **PNTz4T/Y6** blend film. These internal and surface morphologies could partially explain the difference in the photovoltaic performances in these polymers.

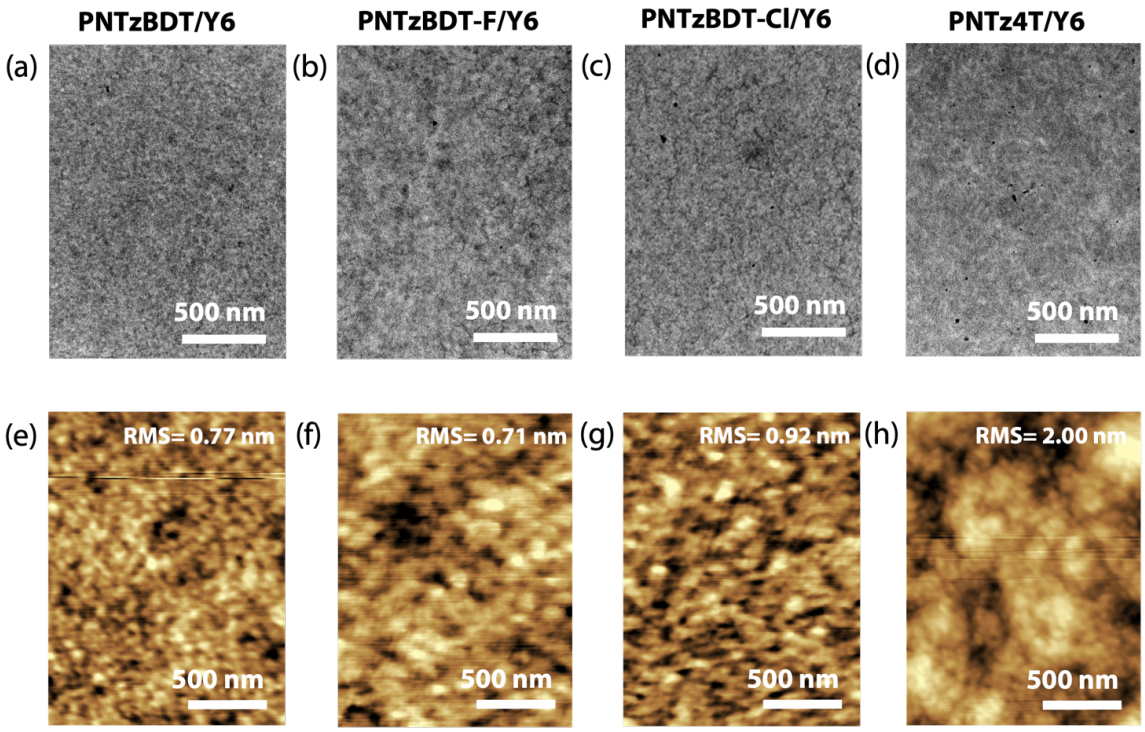

Figure 25 TEM and AFM images of the Y6-blend films for (a, e) **PNTzBDT**/Y6, (b, f) **PNTzBDT-F**/Y6, (c, g) **PNTzBDT-Cl**/Y6, and (d, h) **PNTz4T**/Y6.

In addition, we measured the contact angles of the neat films of the polymers and Y6 (Figure 26) and calculated their surface and interfacial energies, which are summarized in Table 5, to discuss their miscibility.[80-81] The interfacial energy, *i.e.*, the Flory–Huggins interaction parameter, χ, is expressed by the following equation, $\chi = k(\sqrt{\gamma_D} - \sqrt{\gamma_A})^2$, where k is a constant, and γ_D and γ_A are the surface energies of the neat films of the polymers and **Y6**, respectively. The $(\sqrt{\gamma_D} - \sqrt{\gamma_A})^2$ values are also summarized in Table 4. The large difference in the surface energy corresponded to a large interfacial energy and thus large repulsive interaction (low miscibility) between the two materials.[82] The NTz-BDT polymers exhibited higher γ_D values (28–31 mN m^{-1}) than that of **PNTz4T** (24 mN m^{-1}). Among the NTz-BDT polymers, **PNTzBDT** exhibited lower surface energy than **PNTzBDT-F** and **PNTzBDT-Cl**, which could have originated from the larger polarity of

the halogen atoms.[83] Although the NTz-BDT polymers exhibited significantly higher solubility than **PNTz4T**, the $(\sqrt{\gamma_D} - \sqrt{\gamma_A})^2$ values for the blend films of the NTz-BDT polymers (0.035–0.191) were larger than that for the **PNTz4T** (0.030). Notably, because the surface roughness and crystallinity between the neat films of the NTz-BDT polymers and **PNTz4**T differed, it may be inappropriate to discuss the miscibility between polymer and **Y6** using the $(\sqrt{\gamma_D} - \sqrt{\gamma_A})^2$ values. Nevertheless, the NTz-BDT polymers mostly exhibited similar surface roughnesses and crystallinities, which enabled us to compare the miscibility using this method. **PNTzBDT/Y6** and **PNTzBDT-F/Y6** had $(\sqrt{\gamma_D} - \sqrt{\gamma_A})^2$ values of 0.035 and 0.082, respectively, which were smaller than that of **PNTzBDT-Cl/Y6** (0.191), suggesting that the first two exhibited better miscibility than the latter, correlating with the TEM results.

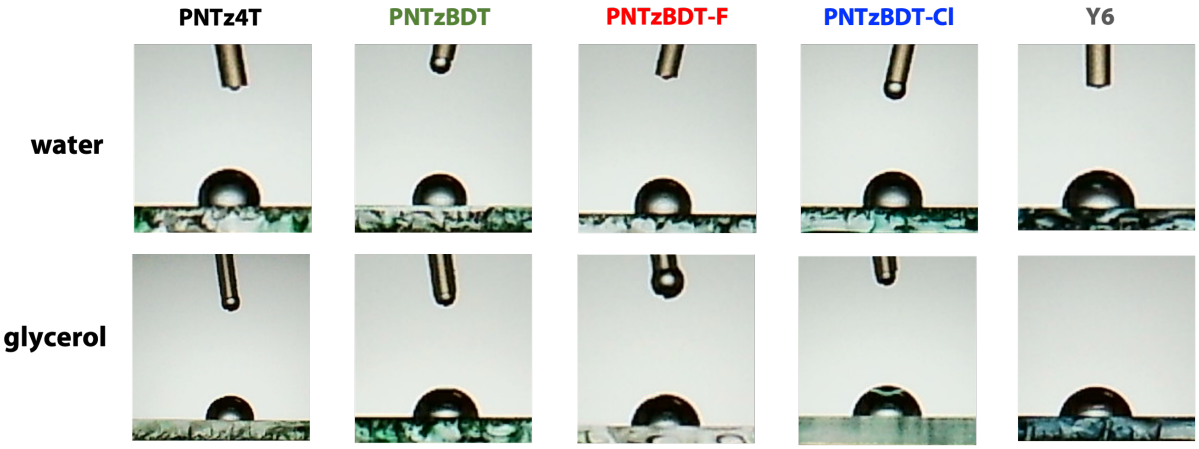

Figure 26 Contact angle of water and glycerol on **PNTzBDT**, **PNTzBDT-F**, **PNTzBDT-Cl, PNTz4T** and Y6 films.

Table 5 Summary of contact angle of water and glycerol on each polymer, the surface tensions of and the corresponding χ parameters of all blend films.

polymer	θ_{water}	$\theta_{glycerol}$	γ_D (mN m^{-1}) [a]	γ_A (mN m^{-1}) [b]	$(\sqrt{\gamma_D}-\sqrt{\gamma_A})^2$
PNTzBDT	99	82	27.86	–	0.035
PNTzBDT-F	101	82	28.94	–	0.082
PNTzBDT-Cl	102	82	30.58	–	0.191
PNTz4T	104	89	24.21	–	0.030
Y6	91	81	–	25.94	-

[a] γ_D: surface energy of the polymers. γ_A: surface energy of Y6. [b]parameter for the interfacial energy χ, which is defined as $\chi = k(\sqrt{\gamma_D} - \sqrt{\gamma_A})^2$

5-4 Summary

Here, we synthesized a series of NTz-BDT semiconductive polymers, **PNTzBDT**, **PNTzBDT-F**, and **PNTzBDT-Cl**. On the one hand, the alkylthienyl side chains provided torsion with respect to the BDT moiety, which suppressed the crystallinity of the polymers, compared with that of the crystalline NTz-based polymer, **PNTz4T**. On the other hand, these side chains probably improved the solubility of the polymer and in turn, the solution processability and possibly better miscibility with Y6. The NTz-BDT polymers exhibited wider optical bandgaps and deeper HOMO energy levels than **PNTz4T** because of the weak electron-donating nature of BDT; the halogenation of the alkylthienyl substituents further deepened the E_{HOMO}. The photovoltaic performance of the NTz-BDT polymers was studied by fabricating photovoltaic cells with a conventional structure using Y6 as the acceptor material. All the cells based on the NTz-BDT polymers exhibited a higher V_{OC} than that of **PNTz4T**. Among them, the PNTzBDT-F cell exhibited the highest PCE of 13.3%, which was significantly higher than that of the **PNTz4T** cell (11.1%). To the best of our knowledge, we reported for the first time organic photovoltaic cells using NTz-based polymers. The results indicated that semiconductive polymers based on NTz, by rational molecular design, offer high potential for use in non-fullerene cells.

CHAPTER 6 NTz-TPTz Random Copolymers

Triphenyleno[1,2-*c*:7,8-*c'*]bis([1,2,5]thiadiazole (TPTz, Figure 27) was designed and synthesized by Dr. Tajima's research group in Riken. The TPTz unit exhibited strong electron-accepting capability and an expanded aromatic plane. The target was to use the TPTz unit to construct a copolymer with a V-shape structure through the D–A system, which offers a new way to design a new semiconductive polymer.[63] Therefore, what is the reason behind using this kind of TPTz unit in this study?

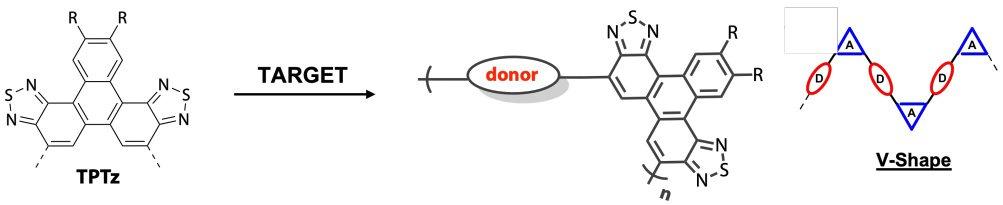

Figure 27 Chemical structure of TPTz unit unit and the illustration of V-shape structure.

The natural structure of **PNTz4T** constituting a linear and rigid polymer structure backbone enabled **PNTz4T** to densely pack together, thereby ensuring high polymer crystallinity. In contrast, it indicated that **PNTz4T** had relatively low solubility. Therefore, we considered that the polymer structure would be a critical point affecting the solubility. Here, our strategy was to introduce a small amount of the TPTz unit into **PNTz4T** to partially destroy the linear structure and construct a foldable NTz-based random copolymer. It was expected that the random copolymers could improve the solubility while preserving the polymer crystallinity. Here, we investigated NTz-TPTz random copolymers in which the TPTz unit was added in small amounts to construct a new semiconductive random polymer. According to the results of a previous study, the side chain on the TPTz

unit had a major effect on performance and solubility. The effect of the different alkyl sidechains on the TPTz unit and the adding ratio of TPTz on the photovoltaic performance and molecular orientation are discussed herein.

The synthetic route for the NTz-TPTz random copolymers is shown in Scheme 3, where NTz2T-Br_2 and the corresponding TPTz unit were copolymerized via the Stille coupling reaction in a yield of approximately 90%. NTz2T-Br_2 and **PNTz4T** were synthesized according to the previous report.[48] Here, we synthesized NTz-TPTz random copolymers with a TPTz unit that possesses different alkyl sidechain substituents, including **C8-5**, **EH-5**, **C12-5**, and **BO-5** (Figure 28). Furthermore, we synthesized NTz-TPTz random copolymers in which the blending ratio of the TPTz units was investigated (blending ratio of 2.5%–10%), namely **C12-2.5**, **C12-5**, **C12-7.5**, and **C12-10**. The NTz-TPTz random copolymers exhibited a significantly improved solubility, compared with that of **PNTz4T** (Table 6). **PNTz4T** exhibited a solubility of 3 mg mL^{-1}. When 2.5% of TPTz was introduced into **PNTz4T,** the solubility significantly improved (27 mg mL^{-1}). However, as the ratio increased to 10%, the solubility (15.6 mg mL^{-1}) decreased but remained better than the initial value, which was consistent with a previous report[63] that the D–A copolymer of the TPTz unit exhibited a low solubility (0.3 mg mL^{-1}). The optical and electrochemical properties, photovoltaic performances, and morphology were carefully investigated. Consequently, we obtained a PCE of 10.8% in the non-fullerene solar cell.

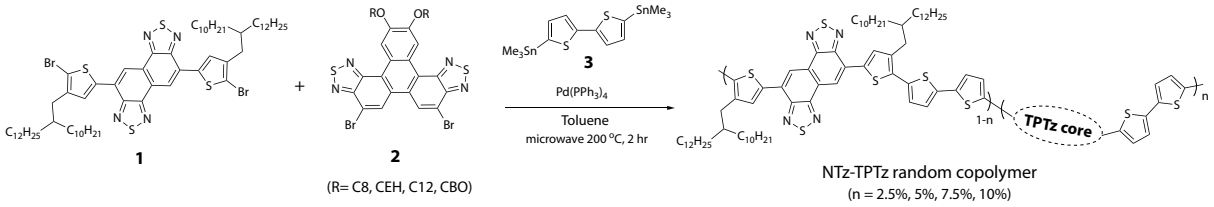

Scheme 3. Synthetic route to the NTz-TPTz random copolymers.

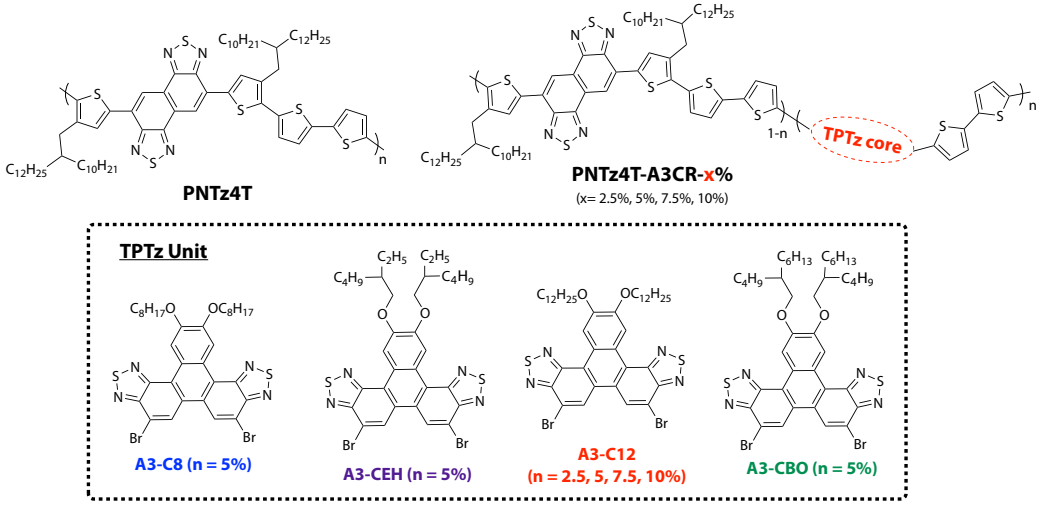

Figure 28 Chemical structure of **PNTz4T** and NTz-TPTz random copolymers.

Table 6 Solubility Estimation of **PNTz4T** and NTz-TPTz random copolymers.

polymer	solubility (mg ml^{-1})	polymer	solubility (mg ml^{-1})
PNTz4T	3.0	C12-2.5	27.3
C8-5	23.1	C12-5	15.4
EH-5	26.2	C12-7.5	27.2
BO-5	27.9	C12-10	15.6

6-1 Physical Property Evaluation

The chemical structure of **PNTz4T** and the NTz-TPTz random copolymers are shown in Figure 28. The NTz-TPTz random copolymers were soluble in CF solvent at room temperature whereas **PNTz4T** needed to be dissolved in hot CF, which might have affected its solution processability. The thermal properties of these polymers were examined by DSC (Figure 29). **C8-5**, **EH-5**, **C12-5**, and **BO-5** exhibited melting points at 313, 313, 312, and 316 °C, respectively. Additionally, **C12-2.5**, **C12-7.5**, and **C12-10** exhibited melting points at 313, 308, and 308°C, respectively, whereas **PNTz4T** exhibited a melting peak at 317 °C. This implied that the polymers were thermally stable in this temperature range.

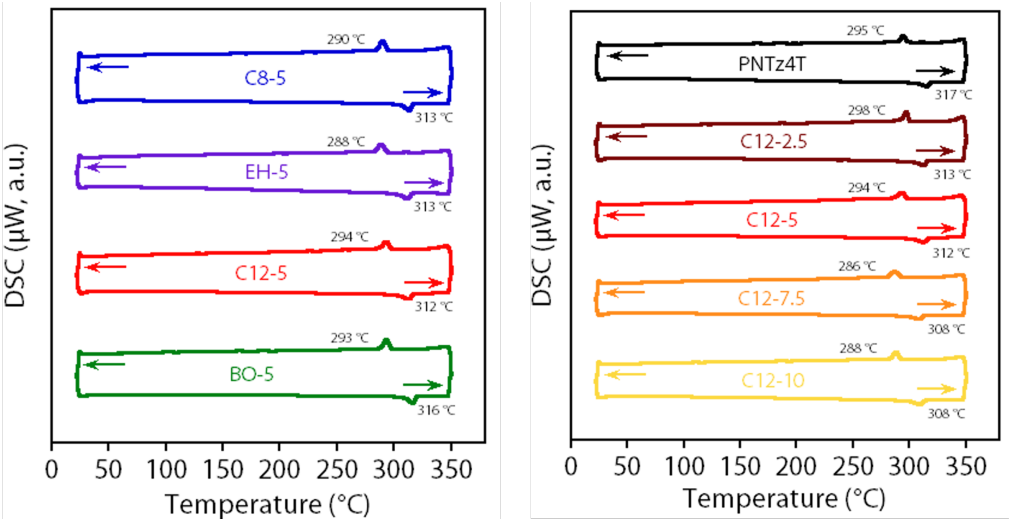

Figure 29 DSC thermograms of **PNTz4T** and NTz-TPTz random copolymers.

6-1-1 Different Alkyl Sidechain on TPTz Unit

The UV–VIS absorption spectra for these polymers in solution and the polymer thin films are shown in Figure 30. The absorption maximum (λ_{max}), absorption edge (λ_{edge}), and optical bandgap (E_g^{opt}) were calculated and are summarized in Table 7. The polymer solution and thin film exhibited a spectrum with the main absorption band ≈ 500–800 nm. In the polymer solution (Figure 30a), **PNTz4T** exhibited λ_{max} = 716 nm, in which a 0–0 band was observed, indicating strong aggregation in the solution. The NTz-TPTz random copolymers exhibited λ_{max} = 664, 666, 672, and 661 nm for **C8-5**, **EH-5**, **C12-5**, and **BO-5**, respectively. The introduction of TPTz reduced the polymer coplanarity, producing a significant blueshift, compared with **PNTz4T**, indicating the weaker intermolecular interactions of the NTz-TPTz random copolymers. A platform-like absorption peak was observed in the solution. In the thin film (Figure 30b), the NTz-TPTz random copolymers significantly redshifted from that of **PNTz4T** (λ_{max} = 714 nm), indicating a stronger aggregation for the NTz-TPTz random copolymers in the thin film. Additionally, **PNTz4T** and the NTz-TPTz random copolymers exhibited two peaks, revealing that the polymers were highly ordered in the thin film, and the alkyl side chain on the TPTz unit hardly influenced the molecular ordering.

The E_{HOMO} and E_{LUMO} of the polymers were estimated by conducting CV using the polymer thin films (Figure 30c). First, **PNTz4T** had an E_{HOMO} of −5.20 eV and E_{LUMO} of −3.46 eV, whereas the NTz-TPTz random copolymers exhibited a lower E_{HOMO} than that of **PNTz4T**, resulting in a larger electrochemical HOMO–LUMO gap of > 1.80 eV for the NTz-TPTz random copolymers, compared with that for **PNTz4T** (1.7 eV). This suggested that the introduction of TPTz (with different alkyl sidechains) had a greater influence on

the E_{HOMO} than the E_{LUMO}. Notably, the NTz-TPTz random copolymers exhibited similar energy levels, **C8-5** (−5.36 and −3.60 eV), **EH-5** (−5.37 and −3.57 eV), **C12-5** (−5.36 and −3.56 eV), and **BO-5** (−5.38 and −3.54 eV) because of the use of the electron-withdrawing TPTz unit. However, the alkyl sidechain hardly influenced the energy level.

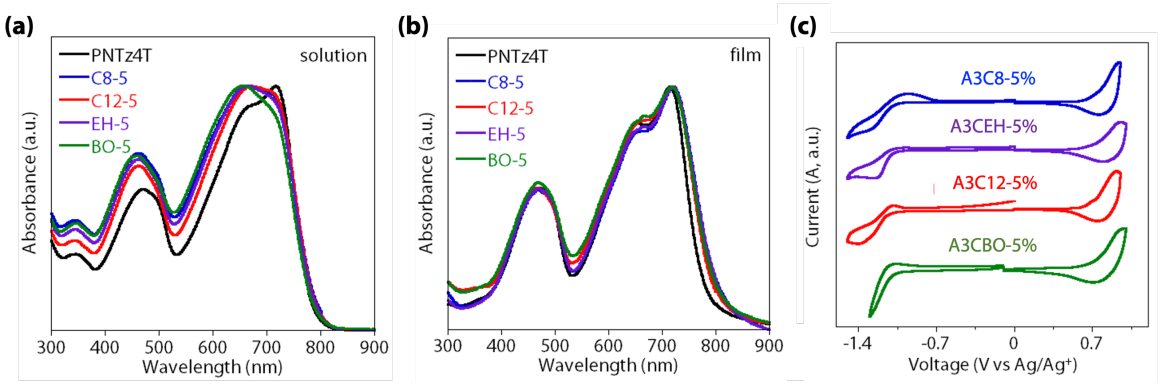

Figure 30 (a,b) UV-vis absorption spectra of the NTz-TPTz random copolymers (different alkyl sidechain on TPTz unit depend) in the solution (a) and thin film (b). (c) Cyclic voltammograms of the thin films for the NTz-TPTz random copolymers vs Ag/Ag^+ as the reference electrode.

Table 7 Optical and electrochemical properties of the polymer thin films.

Polymer	E_{LUMO} (eV) [a]	E_{HOMO} (eV) [a]	λ_{max}^{sol} (nm) [b]	λ_{max}^{film} (nm) [c]	λ_{edge} (nm) [c]	E_g^{opt} (eV) [b]
PNTz4T	−3.46	−5.20	716	657, 714	776	1.60
C8-5	-3.60	−5.36	664	650, 722	805	1.54
C12-5	−3.56	−5.36	672	651, 721	803	1.55
EH-5	−3.57	−5.37	666	653, 720	808	1.53
BO-5	−3.54	−5.38	661	664, 717	803	1.55

[a] E_{LUMO} and E_{HOMO} determined by the onset oxidation and reduction potential of the cyclic voltammograms; [b] Absorption maximum determined from solution absorption spectrum; [c] Absorption maximum, absorption edge and optical bandgap determined from thin film absorption spectrum.

6-1-2 Different TPTz Ratio

The UV–VIS absorption spectra for these polymers in solution and the polymer thin films are shown in Figure 31. The absorption maximum (λ_{max}), absorption edge (λ_{edge}), and optical bandgap (E_g^{opt}) were calculated and are summarized in Table 8. The polymer solution and thin film exhibited a spectrum with the main absorption band ≈ 500–800 nm. In the polymer solution (Figure 31a), the NTz-TPTz random copolymers significantly blue-shifted, compared with that of **PNTz4T** (λ_{max} = 716), which afforded λ_{max} = 678, 672, 669, and 669 nm for **C12-2.5**, **C12-5**, **C12-7.5**, and **C12-10**, respectively. This suggested that the introduction of the TPTz unit affected the coplanarity, owing to the weak intermolecular interactions of the NTz-TPTz random copolymers. In the thin film (Figure 31b), **C12-2.5** (λ_{max} = 720), **C12-5** (λ_{max} = 721), and **C12-7.5** (λ_{max} = 717) slightly redshifted from that of **PNTz4T** (λ_{max} = 714), implying that the small proportion of TPTz in **PNTz4T** slightly enhanced the intermolecular interactions of the NTz-TPTz random copolymers. Nevertheless, **C12-10** blueshifted, compared with **PNTz4T** and the NTz-TPTz random copolymers (2.5%–7.5%), owing to the strong electron-withdrawing effect of the TPTz unit, in which the donor–acceptor interaction weakened because the TPTz unit exceeded a certain amount. Moreover, **PNTz4T** and the NTz-TPTz random copolymers were observed to exhibit two peaks; the peak in the shorter wavelength region appeared as a shoulder. The peaks were assigned to the 0–0 (700–720 nm) and 0–1 (650–670 nm) vibrational bands. The intensity ratio of the 0–0 to 0–1 band decreased as the ratio increased, implying that **C12-2.5** and **C12-5** were relatively ordered, compared with **C12-7.5** and **C12-10**.

The E_{HOMO} and E_{LUMO} of the polymers were estimated by conducting CV using the

polymer thin films (Figure 31c). The NTz-TPTz random copolymers exhibited a lower E_{HOMO} than those of **PNTz4T** (−5.20 eV), **C12-2.5** (−5.38 eV), **C12-5** (−5.36 eV), **C12-7.5** (−5.37 eV), and **C12-10** (−5.37 eV). However, the adding ratio of TPTz did not affect the energy level, resulting in larger electrochemical HOMO–LUMO gaps of **C12-2.5** (1.84 eV), **C12-5** (1.80 eV), **C12-7.5** (1.83 eV) and **C12-10** (1.80 eV), compared with that of **PNTz4T** (1.75 eV).

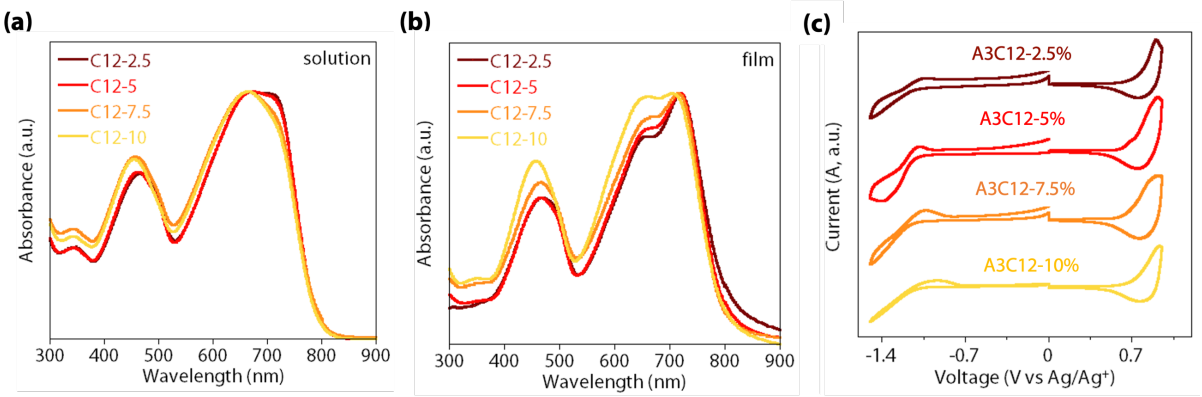

Figure 31 (a,b) UV-vis absorption spectra of the NTz-TPTz random copolymers in the solution (a) and thin film (b). (c) Cyclic voltammograms of the thin films for the NTz-TPTz polymers random copolymers vs Ag/Ag^+ as the reference electrode.

Table 8 Optical and electrochemical properties of the polymer thin films.

Polymer	E_{LUMO} (eV) [a]	E_{HOMO} (eV) [a]	λ_{max}^{sol} (nm) [b]	λ_{max}^{film} (nm) [c]	λ_{edge} (nm) [c]	E_g^{opt} (eV) [b]
PNTz4T	−3.46	−5.20	716	657, 714	776	1.60
C12-2.5	−3.54	−5.38	678	654, 720	800	1.55
C12-5	−3.56	−5.36	672	651, 721	803	1.55
C12-7.5	−3.54	−5.37	669	663, 717	795	1.56
C12-10	−3.57	−5.37	669	654, 702	795	1.56

[a] E_{HOMO} and E_{LUMO} determined by the onset oxidation and reduction potential of the cyclic voltammograms; [b] Absorption maximum determined from solution absorption spectrum; [c] Absorption maximum, absorption edge and optical bandgap determined from thin film absorption spectrum.

6-2 OPV Properties of NTz-TPTz Polymers

6-2-1 Different Alkyl Sidechain on TPTz Unit

The photovoltaic performances of the polymers were investigated by fabricating devices with a conventional architecture (ITO/PEDOT:PSS/active layer/ZnO/Ag). The optimal polymer to **Y6** weight ratio was observed to be 1:1.2, and the optimal active layer thickness was 90–100 nm for all cases. The representative $J-V$ and EQE characteristics of the optimized cells are shown in Figures 32a and b, respectively. The corresponding photovoltaic parameters including the V_{OC}, J_{SC}, FF, and PCE (maximum and average) are summarized in Table 9.

Although **C8-5**, **EH-5**, **C12-5**, and **BO-5** (−5.37 eV) exhibited slightly lower E_{HOMO} values than that of **PNTz4T** (−5.31 eV), the cells with NTz-TPTz random copolymers exhibited a slightly higher $V_{OC} \approx 0.72$–0.74 V, compared with that of **PNTz4T** (0.72 V). The devices exhibited a similar J_{SC} of approximately 21 mA cm^{-2}. Notably, the main difference was the FF. The PNTz4T devices had an FF of 0.68. After the introduction of the TPTz unit, the FF slightly decreased for the **C8-5** and **EH-5** devices (0.65 and 0.62, respectively). As the alkyl sidechain on the TPTz unit lengthened, the **C12-5** device exhibited a higher FF (0.70), compared with that of **PNTz4T** (0.68), but the FF reduced for the **BO-5** device (0.64). This indicated that although the alkyl sidechain length was the same, the linear or branch alkyl chain could still influence the polymer structure, resulting in a slight difference in the performances. These J_{SC} values were consistent with the EQE spectra. Overall, the **C12-5** device achieved a PCE of 10.8%, which was higher than that of the **PNTz4T** device (10.1%), owing to the slightly higher V_{OC} and FF. In Chapter 6-2-2, we discuss the NTz-TPTz random copolymers with different TPTz ratios, in which the

alkyl sidechain on the TPTz unit is fixed with C12.

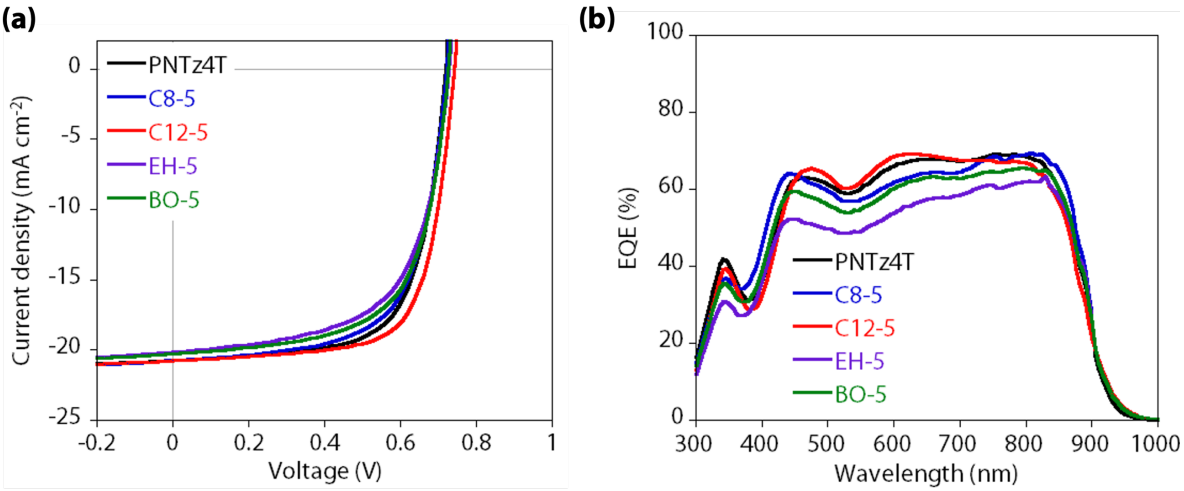

Figure 32 (a) *J*−*V* curves and (b) EQE spectra of the optimized organic solar cells using the NTz-TPTz random copolymers combined with Y6.

Table 9 Summary of photovoltaic parameters of the optimized polymer/Y6 devices.

Polymer	V_{OC} (V)	J_{SC} [J_{SC}^{EQE}]^a (mA cm^{-2})	FF (–)	PCE_{max} [PCE_{ave}] (%) ^{b}
PNTz4T	0.72	20.7 [20.7]	0.68	10.1 [9.7 ± 0.6]
C8-5	0.72	20.7 [20.5]	0.65	9.8 [9.5 ± 0.2]
C12-5	0.74	20.7 [20.8]	0.70	10.8 [10.4 ± 0.4]
EH-5	0.73	20.1 [18.0]	0.62	9.1 [8.8 ± 0.3]
BO-5	0.73	20.2 [19.5]	0.64	9.5 [9.3 ± 0.2]

$^a J_{SC}$ calculated from the EQE spectrum ^{b}Maximum PCE and the average PCE, obtained from more than 10 cells, with standard deviation in the square bracket.

6-2-2 Different TPTz Ratio

The photovoltaic performances of the polymers were investigated by fabricating devices with a conventional architecture (ITO/PEDOT:PSS/polymer/Y6/ZnO/Ag). The optimal polymer to **Y6** weight ratio was observed to be 1:1.2, and the optimal active layer thickness was 90–100 nm for all cases. The representative *J*–*V* and EQE characteristics of the optimized organic solar cells are shown in Figures 33a and b, respectively. The corresponding photovoltaic parameters including the V_{OC}, J_{SC}, FF, and PCE (maximum and average) are summarized in Table 10.

The NTz-TPTz random copolymers with different TPTz ratios exhibited similar E_{HOMO} values but were lower than that of **PNTz4T**. The cells with NTz-TPTz random copolymers exhibited V_{OC} values in the range of 0.74−0.75 V, which were slightly higher than those of the cells with **PNTz4T** (0.72 V). **C12-2.5** exhibited a J_{SC} of 19.6 mA cm^{-2}, which was similar to that of **PNTz4T** (20.7 mA cm^{-2}). When the TPTz ratio increased to 5%, **C12-5** exhibited a J_{SC} of 20.7 mA cm^{-2}, which was slightly higher than that of **C12-2.5**. However, as the TPTz ratio exceeded 7.5%, the cells with **C12-7.5** and **C12-10** exhibited significantly lower J_{SC} values of 18.3 and 19.1 mA cm^{-2}, respectively. These J_{SC} values were consistent with the EQE spectra. The **C12-2.5**, **C12-7.5**, and **C12-10** devices exhibited high V_{OC}; their slightly low J_{SC} and FF limited their photovoltaic performances.

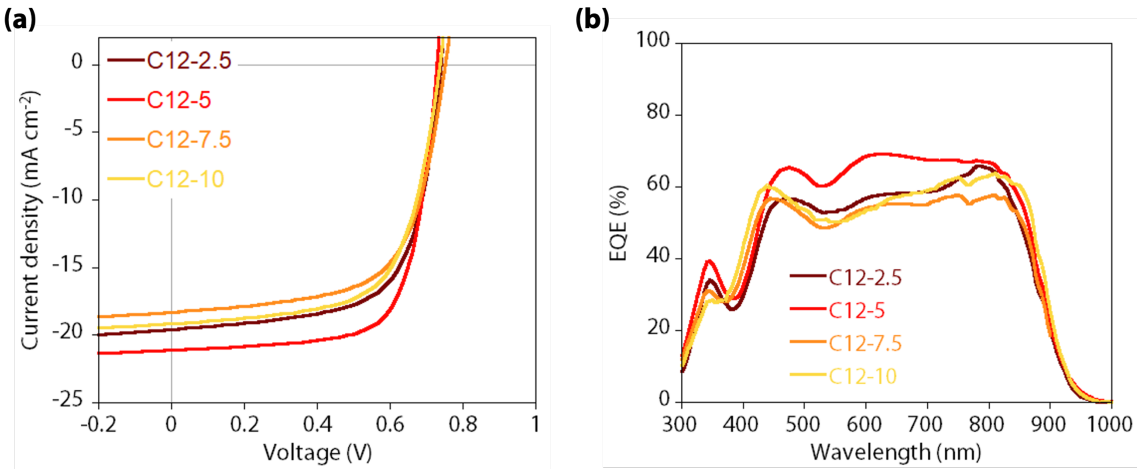

Figure 33 (a) $J-V$ curves and (b) EQE spectra of the optimized organic solar cells using the NTz-TPTz random copolymers combined with Y6.

Table 10 Summary of photovoltaic parameters of the optimized polymer/Y6 devices.

Polymer	V_{OC} (V)	J_{SC} [J_{SC}^{EQE}]^a (mA cm^{-2})	FF (–)	PCE_{max} [PCE_{ave}] (%) ^{b}
PNTz4T	0.72	20.7 [20.7]	0.68	10.1 [9.7 ± 0.6]
C12-2.5	0.74	19.6 [18.4]	0.66	9.6 [9.0 ± 0.6]
C12-5	0.74	20.7 [20.8]	0.70	10.8 [10.4 ± 0.4]
C12-7.5	0.75	18.3 [17.4]	0.64	8.8 [8.1 ± 0.9]
C12-10	0.74	19.1 [18.5]	0.65	9.1 [8.3 ± 0.6]

$^a J_{SC}$ calculated from the EQE spectrum ^{b}Maximum PCE and the average PCE, obtained from more than 10 cells, with standard deviation in the square bracket.

6-3 Charge Recombination Behavior

6-3-1 Different Alkyl Sidechain on TPTz Unit

Charge recombination is a crucial factor that affects photovoltaic performance. Thus, we investigated the devices by probing the dependence of J_{SC} and V_{OC} on the light intensity (P_{light}). Figure 34a displays the light-intensity dependence of J_{SC}. According to the following equation, $J_{SC} \propto P_{light}{}^{\alpha}$,[77-78] the α value closer to 1 indicates that the charge carriers can be efficiently collected at the electrodes by avoiding the bimolecular recombination. The α value varying from 1 indicates that bimolecular recombination is not negligible under the short-circuit condition. As shown in Figure 34a, the devices exhibited similar α values in the range of 0.99–1.01, suggesting that the bimolecular recombination was not serious, and there was no significant difference for these devices.

Figure 34b illustrates the light-intensity dependence of the V_{OC}, which can be used to analyze trap-assisted recombination. The V_{OC} was fitted to the linear law $V_{OC} \propto nk_BT/q\ln(P_{light})$,[78-79] where k_B, q, and T are the Boltzmann constant, elementary charge, and Kelvin temperature, respectively. Factor n for the V_{OC}–$\ln(P_{light})$ plot being equal to 1 suggested that the trap-assisted recombination was negligible; however, n deviating from 1 suggested that the trap-assisted recombination existed under the open-circuit condition. As shown in Figure 34b, the **C12-5** device exhibited an n of 1.06 that was slightly closer to 1, compared to that of the **PNTz4T** device (n = 1.18), indicating that the trap-assisted recombination slightly reduced. This correlated with the results that the **C12-5** device exhibited a slightly larger FF than that of the **PNTz4T** device. Furthermore, the **C8-5** (n = 1.24), **EH-5** (n = 1.41), and **BO-5** (n = 1.33) devices exhibited n values higher than that of **C12-5**, which correlated with the variation in FF.

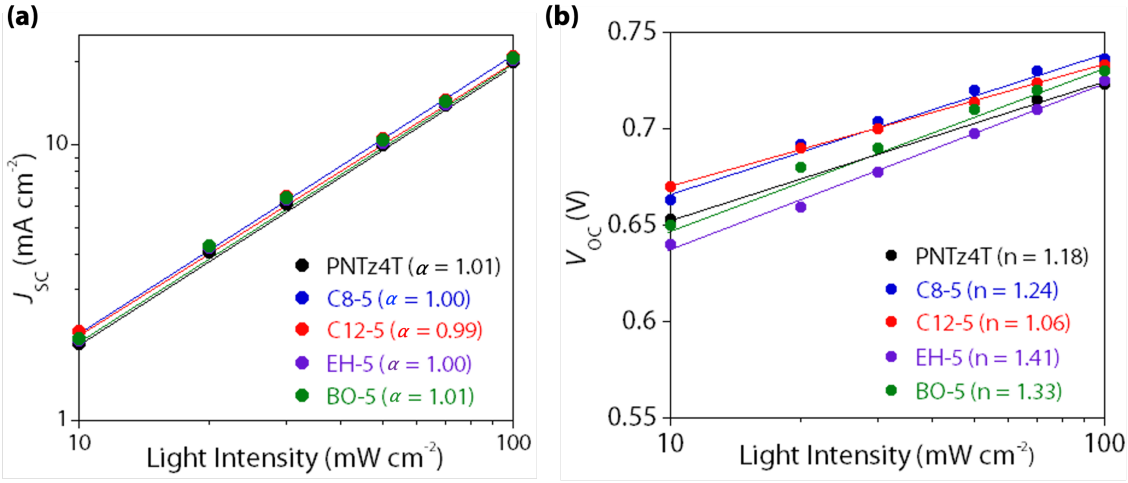

Figure 34 Light-intensity dependence of (a) J_{SC} and (b) V_{OC} for the polymer/Y6 devices.

6-3-2 Different TPTz Ratio

As previously mentioned in Chapter 5-3-1, we can analyze the bimolecular and trap-assisted recombination behavior of the devices by probing the dependence of the J_{SC} and V_{OC} on the light intensity. As shown in Figure 35a, the devices exhibited similar α values in the range of 0.99–1.01, suggesting that the bimolecular recombination was not serious, and there was no significant difference for these devices. Figure 35b illustrates the light-intensity dependence of the V_{OC}. The **C12-7.5**, **C12-7.5**, and **C12-10** (n = 1.20, 1.40, and 1.38, respectively) devices exhibited n values significantly higher than that of the **C12-5** device (n = 1.06). This suggested that the trap-assisted recombination was serious, and the results correlated with the variation in FF. As a result, the **C12-5** device suppressed the charge recombination, resulting in the highest FF among all the devices.

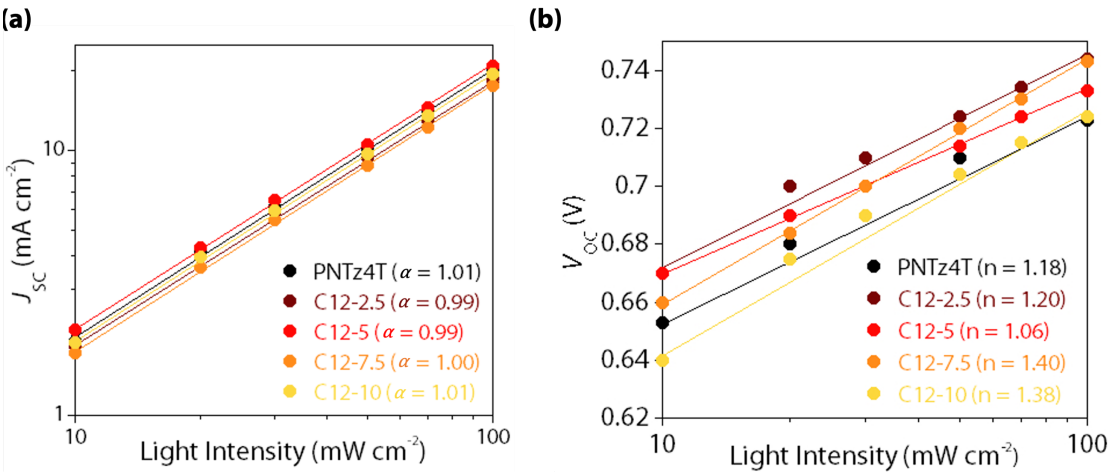

Figure 35 Light-intensity-dependence of (a) J_{SC} and (b) V_{OC} for the polymer/Y6 devices.

6-4 Thin Film Structure

6-4-1 Different Alkyl Sidechain on TPTz Unit

We performed GIWAXS measurements and studied the structural order of the materials, such as the backbone orientation and packing to understand the differences in the photovoltaic performances. Figures 36a–e show the 2D diffraction patterns of the polymer neat films with different alkyl side chains on the TPTz unit, and the corresponding diffraction profiles along the q_z and q_{xy} axes extracted from the 2D patterns are shown in Figure 36k. For the **PNTz4T** neat film (Figure 36a), diffractions assignable to lamellar (*h* 0 0) and π–π stacking (0 1 0) structures were observed along the ~q_z and q_{xy} axes, respectively, indicating that the **PNTz4T** formed the edge-on orientation. In contrast, the NTz-TPTz random copolymers exhibited the lamellar and π–π stacking diffractions along the q_{xy} and ~q_z axes, respectively, indicating the face-on orientation for these polymers. The results indicated that the introduction of the TPTz unit into **PNTz4T** made the polymer backbone oriented parallel to the substrate. The *d*-spacing of the π–π stacking (d_π) for the NTz-TPTz random copolymers (~3.55 Å) was similar with that of **PNTz4T** (3.57 Å). Although the introduction of TPTz did not significantly affect the intermolecular interaction, the lamellar distance of these NTz-TPTz random copolymers became wider (~24 Å) than that of **PNTz4T** (22 Å), implying that the introduction of TPTz suppressed the lamellar interaction, providing a better solubility than that of **PNTz4T**. Additionally, the NTz-TPTz random copolymers exhibited slightly smaller coherence length (L_C) from the π–π stacking (17–23 Å), compared to that of **PNTz4T** (32 Å), calculated using the Scherrer's equation. The results indicated that the introduction of TPTz suppressed the lamellar interaction.

The GIWAXS patterns of the polymer/**Y6** blend films are shown in Figures 36f–j, and the corresponding diffraction profiles are shown in Figure 36l. The blend thin films were observed to exhibit a π–π stacking diffraction along the q_z axis. The d_π observed for the blend films of the NTz-TPTz random copolymers was shorter than that observed for the neat film and far away from that observed for the Y6 neat film (3.60 Å). Therefore, the π–π stacking diffraction in the blend films of the NTz-TPTz random copolymers was assigned to the polymer. In contrast, the d_π for the **PNTz4T** neat and blend films were virtually unchanged at approximately 3.6 Å, and the diffraction patterns were formed differently. We assumed that the π–π stacking diffractions of **PNTz4T** and **Y6** overlapped for the **PNTz4T** blend film (Figure 36f). We calculated the variation in the crystallinity of the blend films of the NTz-TPTz random copolymers. The L_C values for the π–π stacking in the blend films of **C8-5**, **EH-5**, **C12-5**, and **BO-5** were 25, 26, 26, and 20 Å, respectively. As a result, the NTz-TPTz random copolymers with different alkyl side chains provided better solubility than that of **PNTz4T** while preserving the crystallinity of the polymer thin films.

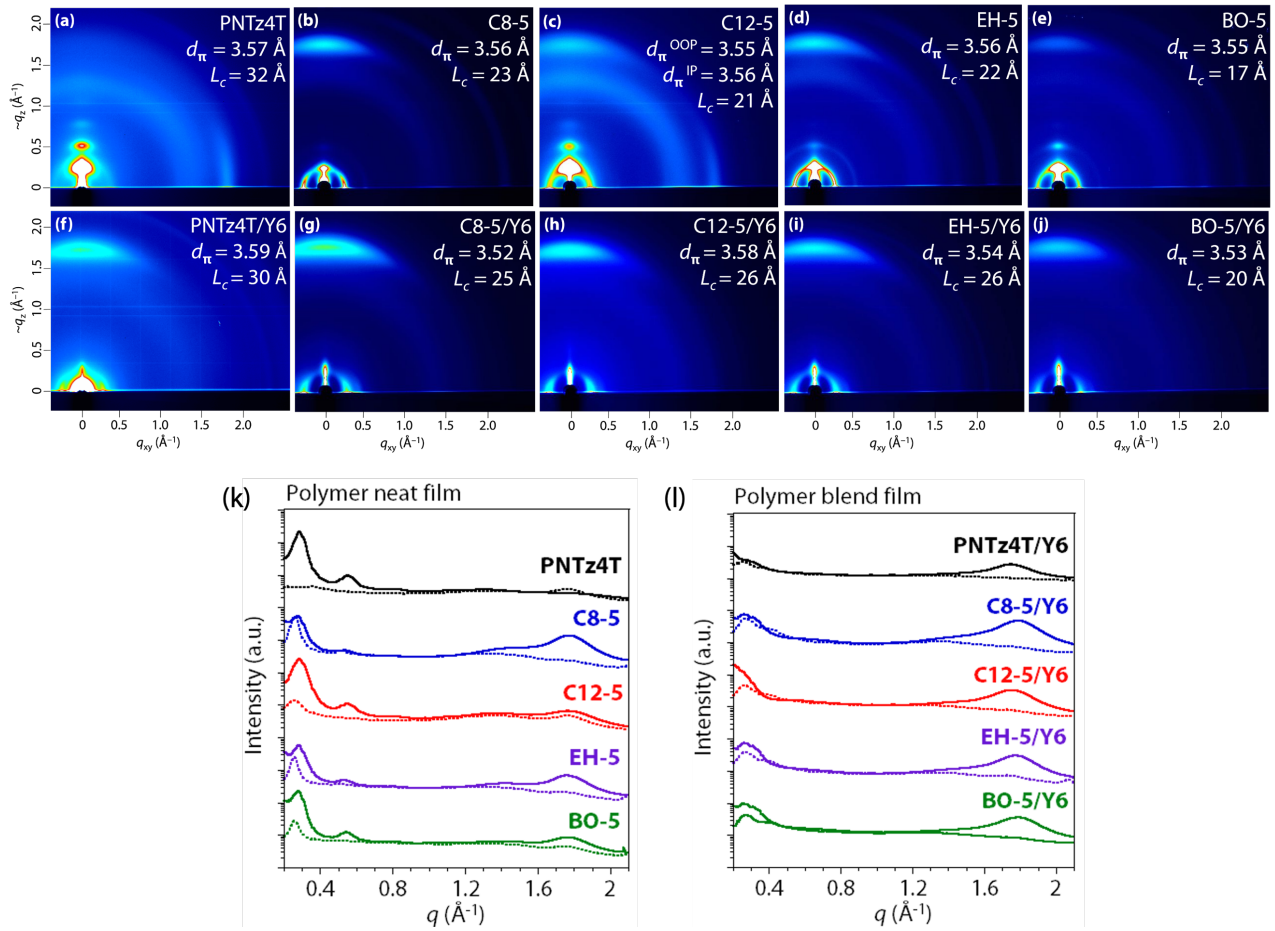

Figure 36 GIWAXS patterns of (a-e) polymer neat films and, (f-j) polymer/Y6 blend films. Corresponding intensity profiles along the out-of-plane (solid line) and in-plane (dotted lines) direction of (k) polymer neat films and, (l) polymer/Y6 blend films.

We conducted TEM to investigate the morphology of the blend films (Figure 37). The **PNTz4T**/Y6 blend film formed similar fibrillar structures with fine networks, as typically observed in many blend systems that provide high photovoltaic performance, which facilitated exciton dissociation and charge transport. The NTz-TPTz/Y6 blend film formed a similar grid-like structure different from that of the **PNTz4T**/Y6 blend film. However, the difference in the photovoltaic performance between **PNTz4T** and the NTz-TPTz random copolymers could not be explained by TEM. Therefore, we probed the relationship

between the thin film morphology and surface roughness by AFM. The **PNTz4T**/**Y6** blend film (Figure 37a, down) formed a large polymer aggregate domain that led to a coarse morphology (root mean square (RMS) = 2.0 nm). The NTz-TPTz/**Y6** blend films exhibited a smoother surface than that of the **PNTz4T**/**Y6** blend film, particularly the random copolymers with a linear alkyl sidechain on the TPTz unit, **C8-5**/**Y6** and **C12-5**/**Y6** (RMS ~ 0.8 nm). Therefore, the highest FF of the cells (0.70) with **C12-5** contributed to a more favorable surface morphology, compared with the **PNTz4T**/**Y6** blend film. We observed an increase in surface roughness to RMS ~1.5 and ~1.1 nm for **EH-5**/**Y6** and **BO-5**/**Y6**, respectively, which might have been detrimental to the FF; hence, their low photovoltaic performances.

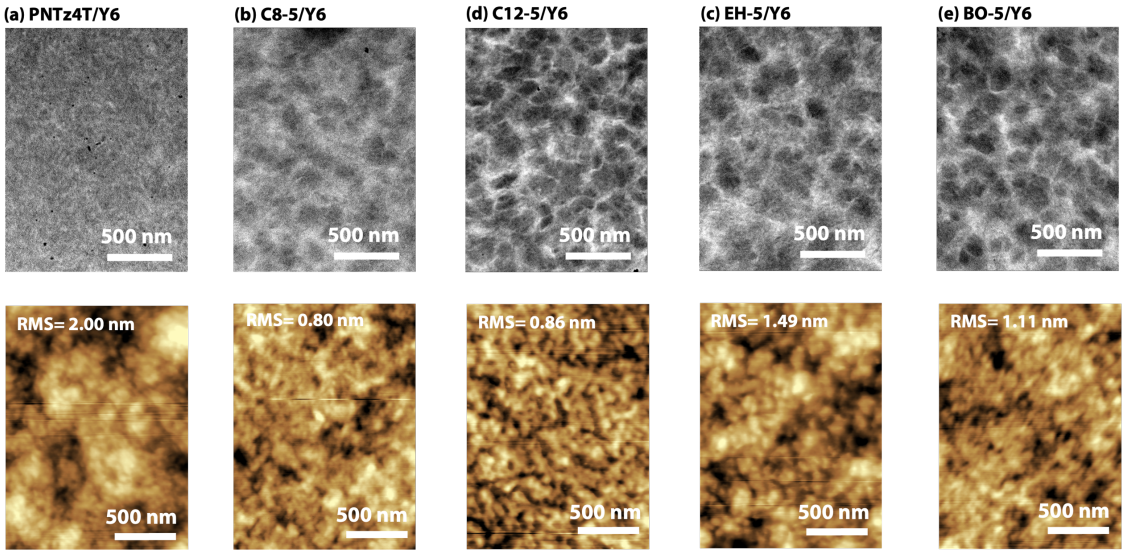

Figure 37 TEM & AFM images of polymer/Y6 blend films. (a) **PNTz4T**/Y6, (b) **C8-5**/Y6, (c) **EH-5**/Y6, (d) **C12-5**/Y6 and (e) **BO-5**/Y6.

6-4-2 Different TPTz Ratio

We performed GIWAXS measurements and studied the structural order of the materials to understand the differences in the photovoltaic performances. Figures 38a–e shows the 2D diffraction patterns of the polymer neat films with different TPTz ratios, and the corresponding diffraction profiles along the q_z and q_{xy} axes extracted from the 2D patterns are shown in Figure 38k. First, **C12-2.5** exhibited lamellar and π–π stacking diffractions along the ~q_z and q_{xy} axes, respectively, indicating edge-on orientation. Interestingly, when the ratio of the TPTz unit increased to 5%, **C12-5** exhibited π–π stacking diffractions along the ~ q_z and q_{xy} axes, suggesting that both edge-on and face-on orientations existed for the **C12-5** neat film. Furthermore, as the ratio exceeded a certain amount, **C12-7.5** and **C12-10** exhibited lamellar and π–π stacking diffractions along the q_{xy} and ~q_z axes, respectively, indicating face-on orientation. The results indicated that the introduction of the TPTz unit into **PNTz4T** gradually turned the polymer backbone into a face-on orientation. The d_π of the neat films (**C12-2.5**, **C12-5**, **C12-7.5** and **C12-10**) were 3.54, 3.55, 3.60, and 3.60 Å, respectively. The NTz-TPTz random copolymers were observed to relatively maintain their intermolecular interaction. However, lamellar interaction was suppressed because of the wider lamellar distance between these NTz-TPTz random copolymers (~24 Å), compared with that of **PNTz4T** (22 Å), which caused the better solubility of the NTz-TPTz random copolymers. Additionally, the NTz-TPTz random copolymers exhibited smaller coherence length (L_C) from the π–π stacking (16–21 Å), compared with that of **PNTz4T** (32 Å), suggesting that the introduction of TPTz slightly affected the crystallinity.

The GIWAXS patterns of the polymer/**Y6** blend films are shown in Figures 38f–j, and the corresponding diffraction profiles are shown in Figure 38l. The blend thin films were

observed to exhibit a π–π stacking diffraction along the q_z axis. First, the d_π observed for the blend films were similar, approximately ~3.58 Å, which was extremely close to that observed for the **Y6** neat film (3.60 Å). Therefore, the π–π stacking diffraction observed for the polymer blend films was assigned to that of **Y6**. The L_C values for the π–π stacking in the blend films of **C12-2.5**, **C12-5**, **C12-7.5**, and **C12-10** were 27, 26, 22, and 20 Å, respectively. Although it was difficult to use the π–π stacking diffraction distance to clarify the difference for these polymer blend films, the crystallinity gradually decreased as the ratio increased, which correlated to the PCE variation in the solar cells.

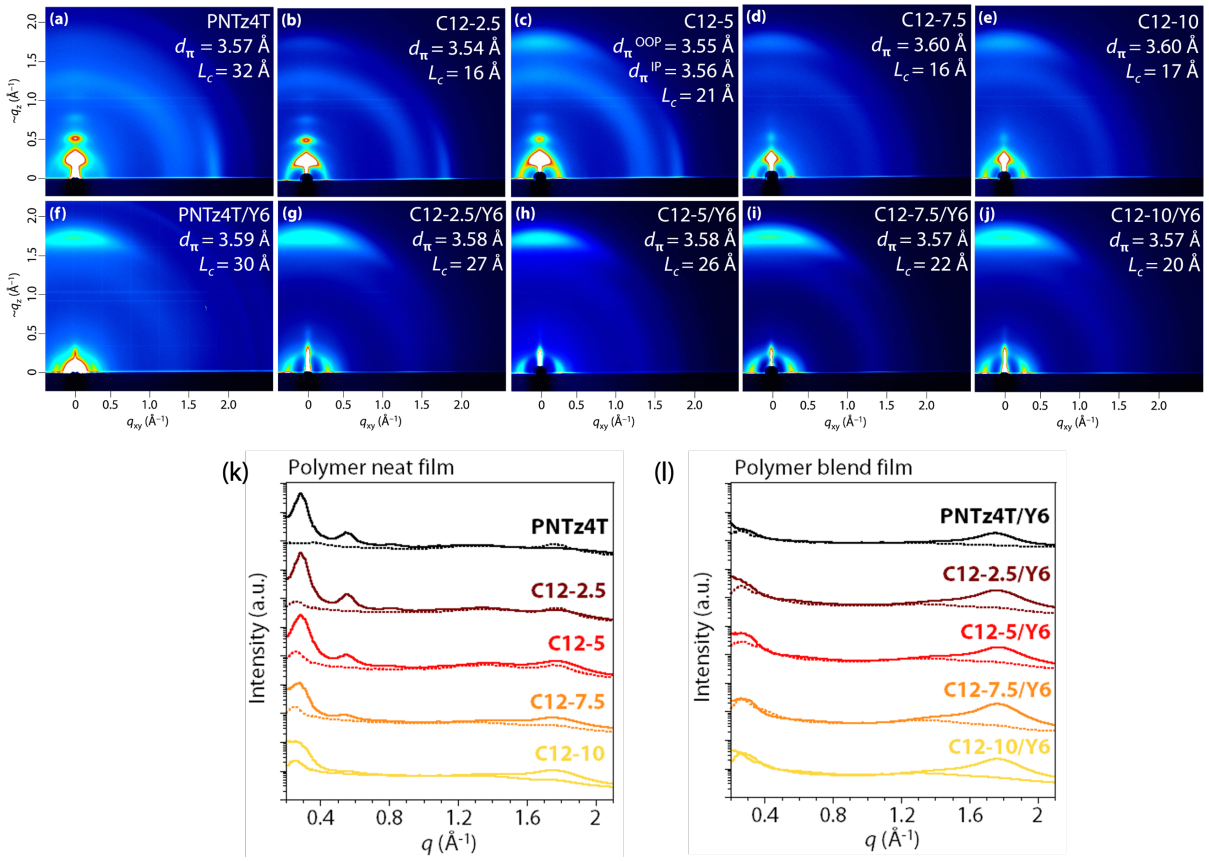

Figure 38 GIWAXS patterns of (a-d) polymer neat films and, (e-h) polymer/Y6 blend films. Corresponding intensity profiles along the out-of-plane (solid line) and in-plane (dotted lines) direction of (i) polymer neat films and, (j) polymer/Y6 blend films.

Next, we performed TEM and AFM to further understand the impact of the TPTz ratio on the surface morphology (Figure 39). The NTz-TPTz/**Y6** blend films exhibited similar grid-like structures, as shown in the TEM images; there was no huge difference. For the AFM analysis, **C12-2.5**/**Y6** and **C12-5**/**Y6** (Figures 39a and b downward) demonstrated good phase separation in their blend thin films that afforded lower surface roughness, compared with that of **PNTz4T**/**Y6** (RMS = 2 nm, Figure 37a). However, the polymer aggregated domain increased as the TPTz ratio increased, particularly the **C12-10**/**Y6** blend film that exhibited a coarse thin film (RMS = 2.4 nm). The results indicated that the surface morphology greatly influenced the photovoltaic performance. A smooth surface was beneficial for interfacial charge transfer, and it improved the performance.

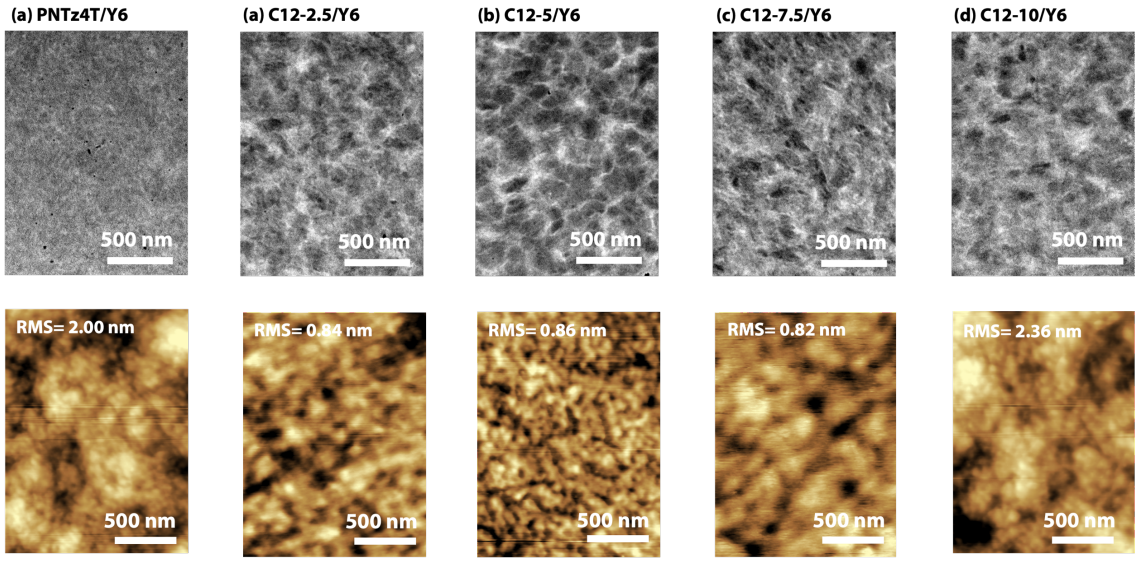

Figure 39 TEM and AFM images of polymer/Y6 blend films. (a) **C12-2.5**/Y6, (b) **C12-5**/Y6, (c) **C12-7.5**/Y6 and (d) **C12-10**/Y6.

6-5 Summary

We synthesized new semiconductive polymers, NTz-TPTz random copolymers, with a TPTz unit possessing different lengths of alkyl substituents, including **C8-5, EH-5, C12-5**, and **BO-5**. Furthermore, the impact of the TPTz ratio on **C12-2.5, C12-5, C12-7.5**, and **C12-10** are discussed. These NTz-TPTz random copolymers exhibited better solubility than that of **PNTz4T** because of the suppressed lamellar interaction through the partially destroyed linear polymer structure of **PNTz4T**. Additionally, the increase in the TPTz ratio caused the polymer packing to gradually change from edge-on (**C12-2.5**) and bimodal (**C12-5**) to face-on orientation as the ratio exceeded 7.5% (**C12-7.5** and **C12-10**). Moreover, the NTz-TPTz/Y6 polymer blend film exhibited decreased surface roughness, compared with that of **PNTz4T**/Y6, whose surface morphology was a critical point that affected the photovoltaic performances. As a result, the **C12-5** devices exhibited the highest PCE of 10.8% in combination with Y6.

CHAPTER 7 CONCLUSION

We designed and synthesized two series of NTz-based polymers, BDT-NTz polymers and NTz-TPTz random copolymers as shown below. These NTz-based polymers exhibited better solubility than the crystalline polymer (**PNTz4T**) that our group previously developed. In the BDT-NTz polymers, the BDT moiety with alkylthienyl substituents afforded steric hindrance between the polymer backbones that suppressed the crystallinity, which enhanced the solubility and electronic properties. Both of which are important for higher efficiencies in non-fullerene-based cells. In contrast, the introduction of TPTz partially destroyed the linear structure of **PNTz4T**, enhancing the solubility without sacrificing the polymer crystallinity. The BDT-NTz polymers and NTz-TPTz random copolymers exhibited face-on orientation, which was favorable for charge transport in photovoltaic cells. Consequently, these new NTz-based polymers exhibited relatively high efficiencies of ~ 13.3% (BDT-NTz polymers) and 10.8% (NTz-TPTz random copolymers) in non-fullerene-based photovoltaic cells, which were even higher than the efficiencies obtained for **PNTz4T**/non-fullerene photovoltaic cells.

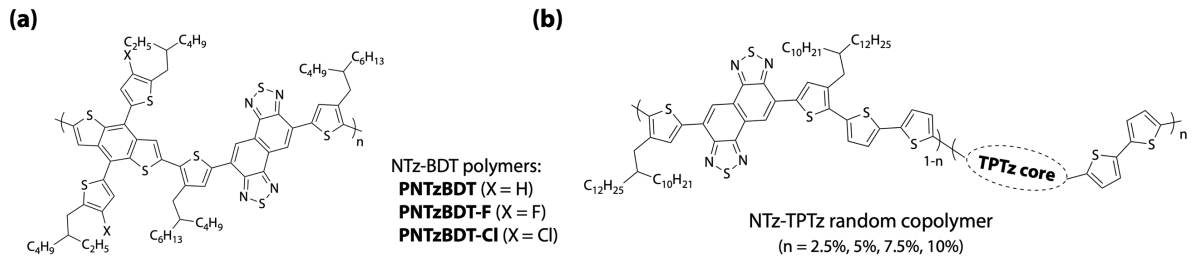

Figure 40 Chemical structure of (a) NTz-BDT polymers, and (b) NTz-TPTz random copolymers.

ACKNOWLEGEMENTS

First, I would like to express my sincere gratitude to my advisor, Prof. Itaru Osaka, for the support for my PhD, patience, enthusiasm, and immense knowledge. His guidance helped me to complete my PhD.

I would not have completed this study without the support of Dr. Masahiko Saito, Dr. Tsubasa Mikie, and my lab members, including Yoshikazu Teshima, Naoya Nakao, Kodai Yamanaka, Takumi Tanaka, and Yuka Iwasaki. In addition, I would like to thank Dr. Keisuke Tajima, Dr. Kyohei Nakano and Dr. Feng-Kung Chen of Riken for providing the TPTz unit, Dr. Tomoyuki Koganezawa of the Japan Synchrotron Radiation Research Institute (JASRI) for the GIWAXS measurement, Dr. Ryo Tanaka for the GPC measurement, and Dr. Makoto Meada for the TEM measurement.

Finally, I would like to sincerely appreciate my parents and brothers for their love, prayers, care, and financial support. They kept me going, and this study would not have been possible without them.

REFERENCE

1. The Iea Shc Solar Update 2009, 50.
2. A. K. Chilvery, A. K. Batra, B. Yang, et al., Perovskites: Transforming Photovoltaics, a Mini-Review. *J. Photonics Energy,* **2015,** *5*, 057402.
3. S. Günes, H. Neugebauer, N. S. Sariciftci. Conjugated Polymer-Based Organic Solar Cells. *Chem. Rev.,* **2007,** *107*, 1324-1338.
4. M. Kaltenbrunner, M. S. White, E. D. Głowacki, et al., Ultrathin and Lightweight Organic Dolar Cells with High Flexibility. *Nat. Commun.,* **2012,** *3*, 1-7.
5. G. Li, R. Zhu, Y. Yang. Polymer Solar Cells. *Nat. Photonics,* **2012,** *6*, 153-161.
6. T. R. Andersen, H. F. Dam, M. Hösel, et al., Scalable, Ambient Atmosphere Roll-to-Roll Manufacture of Encapsulated Large Area, Flexible Organic Tandem Solar Cell Modules. *Energy Environ. Sci.,* **2014,** *7*, 2925-2933.
7. L. Lu, T. Zheng, Q. Wu, et al., Recent Advances in Bulk Heterojunction Polymer Solar Cells. *Chem. Rev.,* **2015,** *115*, 12666-12731.
8. G. Yu, J. Gao, J. C. Hummelen, et al., Polymer Photovoltaic Cells: Enhanced Efficiencies Via a Network of Internal Donor-Acceptor Heterojunctions. *Science,* **1995,** *270*, 1789-1791.
9. B. C. Thompson, J. M. Fréchet. Polymer–Fullerene Composite Solar Cells. *Angew. Chem. Int. Ed.,* **2008,** *47*, 58-77.
10. Y. He, Y. Li. Fullerene Derivative Acceptors for High Performance Polymer Solar Cells. *Phys. Chem. Chem. Phys.,* **2011,** *13*, 1970-1983.
11. Y. Lin, J. Wang, Z. G. Zhang, et al., An Electron Acceptor Challenging Fullerenes for Efficient Polymer Solar Cells. *Adv. Mater.,* **2015,** *27*, 1170-1174.
12. J. Yuan, Y. Zhang, L. Zhou, et al., Single-Junction Organic Solar Cell with over 15% Efficiency Using Fused-Ring Acceptor with Electron-Deficient Core. *Joule,* **2019,** *3*, 1140-1151.
13. Y. Cui, H. Yao, J. Zhang, et al., Single-Junction Organic Photovoltaic Cells with Approaching 18% Efficiency. *Adv. Mater.,* **2020,** *32*, 1908205.
14. A. Armin, W. Li, O. J. Sandberg, et al., A History and Perspective of Non-Fullerene Electron Acceptors for Organic Solar Cells. *Adv. Energy Mater.,* **2021,** *11*, 2003570.
15. M. Zhang, X. Guo, W. Ma, et al., A Large-Bandgap Conjugated Polymer for Versatile Photovoltaic Applications with High Performance. *Adv. Mater.,* **2015,** *27*, 4655-4660.
16. Z. Cao, J. Chen, S. Liu, et al., Synergistic Effects of Polymer Donor Backbone Fluorination

and Nitrogenation Translate into Efficient Non-Fullerene Bulk-Heterojunction Polymer Solar Cells. *ACS Appl. Mater. Interfaces,* **2020,** *12*, 9545-9554.

17. M. Saito, T. Fukuhara, S. Kamimura, et al., Impact of Noncovalent Sulfur–Fluorine Interaction Position on Properties, Structures, and Photovoltaic Performance in Naphthobisthiadiazole-Based Semiconducting Polymers. *Adv. Energy Mater.,* **2020,** *10*, 1903278.
18. X. Zhan, Z. A. Tan, B. Domercq, et al., A High-Mobility Electron-Transport Polymer with Broad Absorption and Its Use in Field-Effect Transistors and All-Polymer Solar Cells. *J. Am. Chem. Soc.,* **2007,** *129*, 7246-7247.
19. H. Yan, Z. Chen, Y. Zheng, et al., A High-Mobility Electron-Transporting Polymer for Printed Transistors. *Nature,* **2009,** *457*, 679-686.
20. H. Sun, Y. Tang, C. W. Koh, et al., High-Performance All-Polymer Solar Cells Enabled by an N-Type Polymer Based on a Fluorinated Imide-Functionalized Arene. *Adv. Mater.,* **2019,** *31*, 1807220.
21. J. Yang, B. Xiao, A. Tang, et al., Aromatic-Diimide-Based N-Type Conjugated Polymers for All-Polymer Solar Cell Applications. *Adv. Mater.,* **2019,** *31*, 1804699.
22. A. Tang, J. Li, B. Zhang, et al., Low-Bandgap N-Type Polymer Based on a Fused-Dad-Type Heptacyclic Ring for All-Polymer Solar Cell Application with a Power Conversion Efficiency of 10.7%. *ACS Macro Lett,* **2020,** *9*, 706-712.
23. Y. Cui, Y. Xu, H. Yao, et al., Single-Junction Organic Photovoltaic Cell with 19% Efficiency. *Adv. Mater.,* **2021**, 2102420.
24. C. J. Brabec, A. Cravino, D. Meissner, et al., Origin of the Open Circuit Voltage of Plastic Solar Cells. *Adv. Funct. Mater.,* **2001,** *11*, 374-380.
25. R. A. Janssen, J. Nelson. Factors Limiting Device Efficiency in Organic Photovoltaics. *Adv. Mater.,* **2013,** *25*, 1847-1858.
26. D. Veldman, S. C. Meskers, R. A. Janssen. The Energy of Charge-Transfer States in Electron Donor–Acceptor Blends: Insight into the Energy Losses in Organic Solar Cells. *Adv. Funct. Mater.,* **2009,** *19*, 1939-1948.
27. H. Sirringhaus, P. Brown, R. Friend, et al., Two-Dimensional Charge Transport in Self-Organized, High-Mobility Conjugated Polymers. *Nature,* **1999,** *401*, 685-688.
28. M. Pandey, N. Kumari, S. Nagamatsu, et al., Recent Advances in the Orientation of Conjugated Polymers for Organic Field-Effect Transistors. *J. Mater. Chem. C,* **2019,** *7*, 13323-13351.
29. I. Osaka, K. Takimiya. Backbone Orientation in Semiconducting Polymers. *Polymer,* **2015,**

59, A1-A15.

30. D. Braun, A. Heeger, H. Kroemer. Improved Efficiency in Semiconducting Polymer Light-Emitting Diodes. *J. Electron. Mater.,* **1991,** *20*, 945-948.
31. C. J. Brabec, C. Winder, N. S. Sariciftci, et al., A Low-Bandgap Semiconducting Polymer for Photovoltaic Devices and Infrared Emitting Diodes. *Adv. Funct. Mater.,* **2002,** *12*, 709-712.
32. R. Steyrleuthner, M. Schubert, F. Jaiser, et al., Bulk Electron Transport and Charge Injection in a High Mobility N-Type Semiconducting Polymer. *Adv. Mater.,* **2010,** *22*, 2799-2803.
33. T. Umeda, S. Tokito, D. Kumaki. High-Mobility and Air-Stable Organic Thin-Film Transistors with Highly Ordered Semiconducting Polymer Films. *J. Appl. Phys.,* **2007,** *101*, 054517.
34. Https://Www.Idtechex.Com/En/Research-Article/a-Second-Chance-for-Organic-Photovoltaics/22896.
35. Https://Asia.Nikkei.Com/Business/Technology/Apple-Opts-for-Oled-Screens-for-Entire-5g-Iphone-Range.
36. Https://Veniversum.Me/Ofet/.
37. G. Li, V. Shrotriya, J. Huang, et al., High-Efficiency Solution Processable Polymer Photovoltaic Cells by Self-Organization of Polymer Blends. *Nat. Mater.,* **2005,** *4*, 864-868.
38. W. Ma, C. Yang, X. Gong, et al., Thermally Stable, Efficient Polymer Solar Cells with Nanoscale Control of the Interpenetrating Network Morphology. *Adv. Funct. Mater.,* **2005,** *15*, 1617-1622.
39. J. Xue, B. P. Rand, S. Uchida, et al., A Hybrid Planar–Mixed Molecular Heterojunction Photovoltaic Cell. *Adv. Mater.,* **2005,** *17*, 66-71.
40. Y. He, H.-Y. Chen, J. Hou, et al., Indene− C60 Bisadduct: A New Acceptor for High-Performance Polymer Solar Cells. *J. Am. Chem. Soc.,* **2010,** *132*, 1377-1382.
41. Y. He, G. Zhao, B. Peng, et al., High-Yield Synthesis and Electrochemical and Photovoltaic Properties of Indene-C70 Bisadduct. *Adv. Funct. Mater.,* **2010,** *20*, 3383-3389.
42. G. Zhao, Y. He, Y. Li. 6.5% Efficiency of Polymer Solar Cells Based on Poly (3-Hexylthiophene) and Indene-C60 Bisadduct by Device Optimization. *Adv. Mater.,* **2010,** *22*, 4355-4358.
43. J. Hou, H.-Y. Chen, S. Zhang, et al., Synthesis, Characterization, and Photovoltaic Properties of a Low Band Gap Polymer Based on Silole-Containing Polythiophenes and 2, 1, 3-Benzothiadiazole. *J. Am. Chem. Soc.,* **2008,** *130*, 16144-16145.
44. H.-Y. Chen, J. Hou, S. Zhang, et al., Polymer Solar Cells with Enhanced Open-Circuit

Voltage and Efficiency. *Nat. Photonics,* **2009,** *3*, 649-653.

45. Y. Liang, Z. Xu, J. Xia, et al., For the Bright Future—Bulk Heterojunction Polymer Solar Cells with Power Conversion Efficiency of 7.4%. *Adv. Mater.,* **2010,** *22*, E135-E138.
46. T.-Y. Chu, J. Lu, S. Beaupre, et al., Bulk Heterojunction Solar Cells Using Thieno [3, 4-C] Pyrrole-4, 6-Dione and Dithieno [3, 2-B: 2′, 3′-D] Silole Copolymer with a Power Conversion Efficiency of 7.3%. *J. Am. Chem. Soc.,* **2011,** *133*, 4250-4253.
47. S. C. Price, A. C. Stuart, L. Yang, et al., Fluorine Substituted Conjugated Polymer of Medium Band Gap Yields 7% Efficiency in Polymer− Fullerene Solar Cells. *J. Am. Chem. Soc.,* **2011,** *133*, 4625-4631.
48. I. Osaka, M. Shimawaki, H. Mori, et al., Synthesis, Characterization, and Transistor and Solar Cell Applications of a Naphthobisthiadiazole-Based Semiconducting Polymer. *J. Am. Chem. Soc.,* **2012,** *134*, 3498-3507.
49. X. Guo, A. Facchetti, T. J. Marks. Imide-and Amide-Functionalized Polymer Semiconductors. *Chem. Rev.,* **2014,** *114*, 8943-9021.
50. Y. Lin, Y. Li, X. Zhan. Small Molecule Semiconductors for High-Efficiency Organic Photovoltaics. *Chem. Soc. Rev.,* **2012,** *41*, 4245-4272.
51. Y. Lin, X. Zhan. Non-Fullerene Acceptors for Organic Photovoltaics: An Emerging Horizon. *Mater. Horiz.,* **2014,** *1*, 470-488.
52. Y. Cui, H. Yao, L. Hong, et al., Achieving over 15% Efficiency in Organic Photovoltaic Cells Via Copolymer Design. *Adv. Mater.,* **2019,** *31*, 1808356.
53. J. Yuan, T. Huang, P. Cheng, et al., Enabling Low Voltage Losses and High Photocurrent in Fullerene-Free Organic Photovoltaics. *Nat. Commun.,* **2019,** *10*, 1-8.
54. J. Yuan, Y. Zhang, L. Zhou, et al., Fused Benzothiadiazole: A Building Block for N-Type Organic Acceptor to Achieve High-Performance Organic Solar Cells. *Adv. Mater.,* **2019,** *31*, 1807577.
55. A. Karki, J. Vollbrecht, A. L. Dixon, et al., Understanding the High Performance of over 15% Efficiency in Single-Junction Bulk Heterojunction Organic Solar Cells. *Adv. Mater.,* **2019,** *31*, 1903868.
56. S. Mataka, K. Takahashi, Y. Ikezaki, et al., Sulfur Nitride in Organic Chemistry. Part 19. Selective Formation of Benzo-and Benzobis [1, 2, 5] Thiadiazole Skeleton in the Reaction of Tetrasulfur Tetranitride with Naphthalenols and Related Compounds. *Bull. Chem. Soc. Jpn.,* **1991,** *64*, 68-73.
57. M. Wang, X. Hu, P. Liu, et al., Donor–Acceptor Conjugated Polymer Based on Naphtho [1, 2-C: 5, 6-C] Bis [1, 2, 5] Thiadiazole for High-Performance Polymer Solar Cells. *J. Am.*

Chem. Soc., **2011,** *133*, 9638-9641.

58. V. Vohra, K. Kawashima, T. Kakara, et al., Efficient Inverted Polymer Solar Cells Employing Favourable Molecular Orientation. *Nat. Photonics,* **2015,** *9*, 403-408.
59. S. C. Price, A. C. Stuart, L. Yang, et al., Fluorine Substituted Conjugated Polymer of Medium Band Gap Yields 7% Efficiency in Polymer−Fullerene Solar Cells. *J. Am. Chem. Soc.,* **2011,** *133*, 4625-4631.
60. H. Huang, L. Yang, A. Facchetti, et al., Organic and Polymeric Semiconductors Enhanced by Noncovalent Conformational Locks. *Chem. Rev.,* **2017,** *117*, 10291-10318.
61. K. Kawashima, T. Fukuhara, Y. Suda, et al., Implication of Fluorine Atom on Electronic Properties, Ordering Structures, and Photovoltaic Performance in Naphthobisthiadiazole-Based Semiconducting Polymers. *J. Am. Chem. Soc.,* **2016,** *138*, 10265-10275.
62. S. Zhang, Y. Qin, J. Zhu, et al., Over 14% Efficiency in Polymer Solar Cells Enabled by a Chlorinated Polymer Donor. *Adv. Mater.,* **2018,** *30*, 1800868.
63. F. Chen, K. Nakano, Y. Kaji, et al., Triphenyleno [1, 2-C: 7, 8-C′] Bis ([1, 2, 5] Thiadiazole) as a V-Shaped Electron-Deficient Unit to Construct Wide-Bandgap Amorphous Polymers for Efficient Organic Solar Cells. *ACS Appl. Mater. Interfaces,* **2021,** *13*, 57743-57749.
64. S. Li, C.-Z. Li, M. Shi, et al., New Phase for Organic Solar Cell Research: Emergence of Y-Series Electron Acceptors and Their Perspectives. *ACS Energy Letters,* **2020,** *5*, 1554-1567.
65. J. Zhou, B. Zhang, W. Zou, et al., Chlorination of Dithienobenzodithiophene (Dtbdt) Based Polymers to Simultaneously Improve the V Oc, J Sc and Ff of Non-Fullerene Organic Solar Cells. *Sustainable Energy & Fuels,* **2020,** *4*, 5665-5673.
66. N. Nakao, S. Ogawa, H. D. Kim, et al., Pronounced Backbone Coplanarization by Π-Extension in a Sterically Hindered Conjugated Polymer System Leads to Higher Photovoltaic Performance in Non-Fullerene Solar Cells. *ACS Appl. Mater. Interfaces,* **2021**.
67. X. Yuan, Y. Zhao, T. Zhan, et al., A Donor Polymer Based on 3-Cyanothiophene with Duperior Batch-to-Batch Reproducibility for High-Efficiency Organic Solar Cells. *Energy Environ. Sci.,* **2021,** *14*, 5530-5540.
68. L. Zhang, X. Huang, C. Duan, et al., Morphology Evolution with Polymer Chain Propagation and Its Impacts on Device Performance and Stability of Non-Fullerene Solar Cells. *J. Mater. Chem. A,* **2021,** *9*, 556-565.
69. H. J. Son, F. He, B. Carsten, et al., Are We There Yet? Design of Better Conjugated Polymers for Polymer Solar Cells. *J. Mater. Chem.,* **2011,** *21*, 18934-18945.
70. L. Ye, S. Zhang, L. Huo, et al., Molecular Design toward Highly Efficient Photovoltaic Polymers Based on Two-Dimensional Conjugated Benzodithiophene. *Acc. Chem. Res.,* **2014,**

47, 1595-1603.

71. H. Yao, L. Ye, H. Zhang, et al., Molecular Design of Benzodithiophene-Based Organic Photovoltaic Materials. *Chem. Rev.,* **2016,** *116*, 7397-7457.
72. J. Hou, M.-H. Park, S. Zhang, et al., Bandgap and Molecular Energy Level Control of Conjugated Polymer Photovoltaic Materials Based on Benzo [1, 2-B: 4, 5-B′] Dithiophene. *Macromolecules,* **2008,** *41*, 6012-6018.
73. L. Huo, J. Hou. Benzo [1, 2-B: 4, 5-B′] Dithiophene-Based Conjugated Polymers: Band Gap and Energy Level Control and Their Application in Polymer Solar Cells. *Polym. Chem.,* **2011,** *2*, 2453-2461.
74. M. Zhang, X. Guo, S. Zhang, et al., Synergistic Effect of Fluorination on Molecular Energy Level Modulation in Highly Efficient Photovoltaic Polymers. *Adv. Mater.,* **2014,** *26*, 1118-1123.
75. Z. Zheng, O. M. Awartani, B. Gautam, et al., Efficient Charge Transfer and Fine-Tuned Energy Level Alignment in a Thf-Processed Fullerene-Free Organic Solar Cell with 11.3% Efficiency. *Adv. Mater.,* **2017,** *29*, 1604241.
76. B. Qiu, S. Chen, H. Li, et al., A Simple Approach to Prepare Chlorinated Polymer Donors with Low-Lying Homo Level for High Performance Polymer Solar Cells. *Chem. Mater.,* **2019,** *31*, 6558-6567.
77. P. Schilinsky, C. Waldauf, C. J. Brabec. Recombination and Loss Analysis in Polythiophene Based Bulk Heterojunction Photodetectors. *Appl. Phys. Lett.,* **2002,** *81*, 3885-3887.
78. S. R. Cowan, A. Roy, A. J. Heeger. Recombination in Polymer-Fullerene Bulk Heterojunction Solar Cells. *Phys. Rev. B: Condens. Matter Mater. Phys.,* **2010,** *82*, 245207.
79. L. J. A. Koster, V. D. Mihailetchi, R. Ramaker, et al., Light Intensity Dependence of Open-Circuit Voltage of Polymer: Fullerene Solar Cells. *Appl. Phys. Lett.,* **2005,** *86*, 123509.
80. J. Comyn. Contact Angles and Adhesive Bonding. *Int. J. Adhes. Adhes.,* **1992,** *12*, 145-149.
81. K.-H. Kim, H. Kang, H. J. Kim, et al., Effects of Solubilizing Group Modification in Fullerene Bis-Sdducts on Normal and Inverted Type Polymer Solar Cells. *Chem. Mater.,* **2012,** *24*, 2373-2381.
82. S. Nilsson, A. Bernasik, A. Budkowski, et al., Morphology and Phase Segregation of Spin-Casted Films of Polyfluorene/Pcbm Blends. *Macromolecules,* **2007,** *40*, 8291-8301.
83. Z. Liu, Y. Gao, J. Dong, et al., Chlorinated Wide-Bandgap Donor Polymer Enabling Annealing Free Non-fullerene Solar Cells with the Efficiency of 11.5%. *J. Phys. Chem. Lett.,* **2018,** *9*, 6955-6962.